

New Angles on Energy Correlation Functions

Ian Moult,^{1,2,3} Lina Necib,³ and Jesse Thaler³

¹*Berkeley Center for Theoretical Physics, University of California, Berkeley, CA 94720, USA*

²*Theoretical Physics Group, Lawrence Berkeley National Laboratory, Berkeley, CA 94720, USA*

³*Center for Theoretical Physics, Massachusetts Institute of Technology, Cambridge, MA 02139, USA*

E-mail: ianmoult@lbl.gov, lnecib@mit.edu, jthaler@mit.edu

ABSTRACT: Jet substructure observables, designed to identify specific features within jets, play an essential role at the Large Hadron Collider (LHC), both for searching for signals beyond the Standard Model and for testing QCD in extreme phase space regions. In this paper, we systematically study the structure of infrared and collinear safe substructure observables, defining a generalization of the energy correlation functions to probe n -particle correlations within a jet. These generalized correlators provide a flexible basis for constructing new substructure observables optimized for specific purposes. Focusing on three major targets of the jet substructure community—boosted top tagging, boosted $W/Z/H$ tagging, and quark/gluon discrimination—we use power-counting techniques to identify three new series of powerful discriminants: M_i , N_i , and U_i . The M_i series is designed for use on groomed jets, providing a novel example of observables with improved discrimination power after the removal of soft radiation. The N_i series behave parametrically like the N -subjettiness ratio observables, but are defined without respect to subjet axes, exhibiting improved behavior in the unresolved limit. Finally, the U_i series improves quark/gluon discrimination by using higher-point correlators to simultaneously probe multiple emissions within a jet. Taken together, these observables broaden the scope for jet substructure studies at the LHC.

Contents

1	Introduction	1
2	Review of Substructure Approaches	3
2.1	Energy Correlation Functions and N -subjettiness	4
2.2	Soft Drop Grooming	7
2.3	Power Counting the Soft/Collinear Behavior	8
3	Enlarging the Basis of Jet Substructure Observables	11
3.1	General Structure of Infrared/Collinear Safe Observables	12
3.2	New Angles on Energy Correlation Functions: $v e_n^{(\beta)}$	13
3.3	New Substructure Discriminants	15
3.3.1	The M_i Series	16
3.3.2	The N_i Series	16
3.3.3	The U_i Series	17
4	Simplifying Observables for Boosted Top Tagging	17
4.1	Constructing the N_3 Observable	17
4.2	Performance in Parton Showers	22
5	New Observables for 2-prong Substructure	25
5.1	Power-Counting Analysis and Observable Phase Space	26
5.1.1	M_2	27
5.1.2	N_2	28
5.1.3	$D_2^{(1,2)}$	30
5.2	Performance in Parton Showers	32
5.3	Stability in Parton Showers	36
6	Improving Quark/Gluon Discrimination	39
6.1	Probing Multiple Emissions with U_i	40
6.2	Performance in Parton Showers	42
7	Conclusions	46
A	Alternative Angular Weighting Functions	47
B	Aspects of 3-prong Tagging	49
B.1	Challenges for M_3	49
B.2	N_3 Without Grooming	50
B.3	Identifying N_3	52
B.4	Power Counting N_3	54
C	Relationship Between N_i and N-subjettiness	56

1 Introduction

With the Large Hadron Collider (LHC) rapidly acquiring data at a center-of-mass energy of 13 TeV, jet substructure observables are playing a central role in a large number of analyses, from Standard Model measurements [1–12] to searches for new physics [13–34].¹ As the field of jet substructure matures [35–38], observables are being designed for increasingly specific purposes, using a broader set of criteria to evaluate their performance beyond simply raw discrimination power. Continued progress relies on achieving a deeper understanding of the QCD dynamics of jets, allowing for more subtle features within a jet to be exploited. This understanding has progressed rapidly in recent years, due both to advances in explicit calculations of jet substructure observables [39–63] as well as to the development of techniques for understanding the dominant properties of substructure observables using analytic [64–66] and machine learning [67–73] approaches.

A particularly powerful method for constructing jet substructure observables is power counting, introduced in Ref. [65]. Given a basis of infrared and collinear (IRC) safe observables, power counting can identify which combinations are optimally sensitive to specific parametric features within a jet.² Furthermore, power counting elucidates the underlying physics probed by the observable. This approach was successfully applied to the energy correlation functions [74], leading to a powerful 2-prong discriminant called D_2 [65]. Vital to the power counting approach, though, is a sufficiently flexible basis of IRC safe observables to allow the construction of discriminants with specific properties.

In this paper, we exploit the known properties of IRC safe observables to systematically identify a useful basis for jet substructure, which we call the generalized energy correlation functions. These observables—denoted by ${}_v e_n^{(\beta)}$ and defined in Eq. (3.3)—are an extension of the original energy correlation functions with a more flexible angular weighting.³ Specially, these new observables correlate v pairwise angles among n particles, whereas the original correlators were restricted to v equaling n choose 2. Using these generalized correlators, we apply power counting to identify new jet substructure observables for each of the major jet substructure applications at the LHC: 3-prong boosted top tagging, 2-prong boosted $W/Z/H$ tagging, and 1-prong quark/gluon discrimination. In each case, our new observables exhibit improved performance over traditional observables when tested with parton shower generators.

¹This is by no means a complete list. Other studies from the LHC using jet substructure can be found at <https://twiki.cern.ch/twiki/bin/view/AtlasPublic> and <http://cms-results.web.cern.ch/cms-results/public-results/publications/>.

²In this paper, we use “basis” to refer to any set of observables, even if they do not span the full space of IRC safe observables.

³The ${}_v e_n$ notation is inspired by the hypergeometric functions, which are similarly flexible.

The flexibility of our basis, combined with insights from power counting, allows us to tailor our observables for specific purposes, beyond those that have been previously considered. As an interesting example, we are able to specifically design observables for use on groomed jets [41, 42, 75–78]. While grooming procedures are heavily used at the LHC to remove jet contamination from initial state radiation, underlying event, and pileup, most LHC analyses apply observables that were designed for use on ungroomed jets. Here, by understanding the impact of grooming on soft radiation, we introduce a 2-prong discriminant, M_2 , which exhibits almost no discrimination power on ungroomed jets, but outperforms traditional observables when measured on groomed jets. This observable therefore acts both as a probe of the grooming procedure and as a powerful discriminant. We also show how the use of groomed observables leads to remarkably stable distributions as a function of the jet mass and p_T , even for distributions that are unstable before grooming, such as D_2 . This has recently been emphasized as a desirable feature for substructure observables, particularly to facilitate sideband calibration and produce smooth mass distributions for backgrounds [79]; observables modified to achieve stability have been used by both ATLAS and CMS [80, 81].

The generalized energy correlation functions allow us to introduce a wide variety of new substructure observables, though we focus on three series with particularly nice properties. The first is the M_i series, defined via the ratio

$$M_i^{(\beta)} = \frac{{}_1e_{i+1}^{(\beta)}}{{}_1e_i^{(\beta)}}. \quad (1.1)$$

These observables identify jets with i hard prongs, but, as mentioned above, are only effective for discrimination on suitably groomed jets. The second is the N_i series, defined via the ratio

$$N_i^{(\beta)} = \frac{2e_{i+1}^{(\beta)}}{({}_1e_i^{(\beta)})^2}, \quad (1.2)$$

which are designed to mimic the behavior of the N -subjettiness ratio $\tau_{i,i-1}$ [82, 83]. The N_i observables are defined without respect to subjet axes, and therefore exhibit improved behavior compared to N -subjettiness, particularly in the transition to the unresolved region, where the definition of subjet axes becomes ambiguous. The third is the U_i series, defined as

$$U_i^{(\beta)} = {}_1e_{i+1}^{(\beta)}, \quad (1.3)$$

which probe multiple emissions within 1-prong jets and can be used to improve quark/gluon discrimination. In all cases, the parameter β controls the overall angular scaling of these observables, and the (β) superscript will often be dropped when clear from context.

To guide the reader, we summarize the particular applications studied in this paper, so that the (un)interested reader can skip to the relevant section. These observables will be made available in the `EnergyCorrelator` FASTJET CONTRIB [84, 85] starting in version 1.2.0.

- **Boosted Top Tagging** (Sec. 4):
 - N_3 : An axes-free observable which reduces to the N -subjettiness ratio $\tau_{3,2}$ in the resolved limit, but exhibits improved performance in the unresolved limit on groomed jets.
- **Boosted $W/Z/H$ tagging** (Sec. 5):
 - M_2 : A 2-prong discriminant specifically designed for use on groomed jets.
 - N_2 : An axes-free observable which reduces to the N -subjettiness ratio $\tau_{2,1}$ in the resolved limit, but exhibits improved performance on both groomed and ungroomed jets.
 - $D_2^{(\alpha,\beta)}$: A generalization of the standard D_2 observable [65] specifically designed for groomed jets, which exhibits improved performance when $\alpha = 1$, $\beta = 2$.
- **Quark/Gluon Discrimination** (Sec. 6):
 - U_i : A new series of observables for quark/gluon discrimination which probes the structure of multiple soft gluon emissions from the hard jet core, leading to improved performance over the standard C_1 observable [74].

The specific form of these observables, and the origin of their discrimination power, will be analyzed using power counting. We verify all power-counting predictions using parton shower generators and compare the performance of our newly introduced observables to traditional observables for each of the above applications.

The remainder of this paper is organized as follows. In Sec. 2, we review standard substructure and grooming techniques as well as the power counting approach for understanding soft and collinear scaling. In Sec. 3, we discuss the general structure of IRC safe observables and introduce the generalized energy correlation functions, $v e_n$, as well as the M_i , N_i , and U_i series. The three key case studies bulleted above appear in Secs. 4, 5, and 6. We conclude in Sec. 7 and discuss possible future directions for improving our understanding of jet substructure at the LHC.

2 Review of Substructure Approaches

In this section, we review a number of standard jet substructure techniques that will be used throughout this paper. We begin in Sec. 2.1 by defining the energy correlation functions [74] and N -subjettiness ratios [82, 83], both of which are widely used in jet substructure. In Sec. 2.2, we review the soft drop/modified mass drop [41, 42, 86] algorithm, which we use as our default grooming procedure. Finally in Sec. 2.3, using the 2-point energy correlation function as an example, we review the power-counting approach for analyzing jet substructure observables, which features heavily in later discussions. Readers familiar with these topics can safely skip to Sec. 3, though we recommend reviewing the logic of Sec. 2.3.

2.1 Energy Correlation Functions and N -subjettiness

The energy correlation functions [74] are a convenient basis of observables for probing multi-prong substructure within a jet. In this paper, we use the 2-, 3-, and 4-point energy correlation functions, defined as⁴

$$\begin{aligned} e_2^{(\beta)} &= \sum_{1 \leq i < j \leq n_J} z_i z_j \theta_{ij}^\beta, \\ e_3^{(\beta)} &= \sum_{1 \leq i < j < k \leq n_J} z_i z_j z_k \theta_{ij}^\beta \theta_{ik}^\beta \theta_{jk}^\beta, \\ e_4^{(\beta)} &= \sum_{1 \leq i < j < k < \ell \leq n_J} z_i z_j z_k z_\ell \theta_{ij}^\beta \theta_{ik}^\beta \theta_{jk}^\beta \theta_{i\ell}^\beta \theta_{j\ell}^\beta \theta_{k\ell}^\beta, \end{aligned} \quad (2.1)$$

where n_J is the number of particles in the jet. The generalization to higher-point correlators is straightforward, though we will not use them here. For simplicity, we often drop the explicit angular exponent β , writing the observable as e_n . This simplified notation will also be used for other observables introduced in the text.

It is convenient to work with dimensionless observables, written in terms of a generic energy fraction variable, z , and a generic angular variable, θ . The precise definitions of the energy fraction and angle can be chosen depending on context and do not affect our power-counting arguments. For the case of pp collisions at the LHC, which is the focus of our later studies, we work with longitudinally boost-invariant variables,

$$z_i \equiv \frac{p_{Ti}}{\sum_{j \in \text{jet}} p_{Tj}}, \quad \theta_{ij}^2 \equiv R_{ij}^2 = (\phi_i - \phi_j)^2 + (y_i - y_j)^2, \quad (2.2)$$

where p_{Ti} , ϕ_i , and y_i are the transverse momentum, azimuthal angle, and rapidity of particle i , respectively. Two other measures intended for e^+e^- collisions are available in the `EnergyCorrelator` `FASTJET` `CONTRIB` [84, 85]. The first is a definition based strictly on energies and opening angles,

$$z_i \equiv \frac{E_i}{E_J}, \quad \theta_{ij}^2 \equiv \Theta_{ij}^2, \quad (2.3)$$

where E_J is the total jet energy, and Θ_{ij} is the Euclidean angle between the 3-momenta \vec{p}_i and \vec{p}_j . There is an alternative definition in terms of energies and Mandelstam invariants,

$$z_i \equiv \frac{E_i}{E_J}, \quad \theta_{ij}^2 \equiv \frac{2p_i \cdot p_j}{E_i E_j}, \quad (2.4)$$

which reduces to Eq. (2.3) in the collinear limit but is easier for analytic calculations.

From Eq. (2.1), we see that the n -point energy correlation functions vanish in the soft and collinear limits, and therefore are natural resolution variables for $(n-1)$ -prong substructure. A number of powerful 2-prong discriminants have been formed from the energy correlation functions [65, 74], namely

$$C_2^{(\beta)} = \frac{e_3^{(\beta)}}{(e_2^{(\beta)})^2}, \quad D_2^{(\beta)} = \frac{e_3^{(\beta)}}{(e_2^{(\beta)})^3}, \quad D_2^{(\alpha,\beta)} = \frac{e_3^{(\alpha)}}{(e_2^{(\beta)})^{3\alpha/\beta}}. \quad (2.5)$$

⁴We use the normalized dimensionless definition denoted with a lower case e [65]. This is related to the original dimensionful definition in Ref. [74] by $e_n^{(\beta)} = \text{ECF}(n, \beta) / (\text{ECF}(1, \beta))^n$.

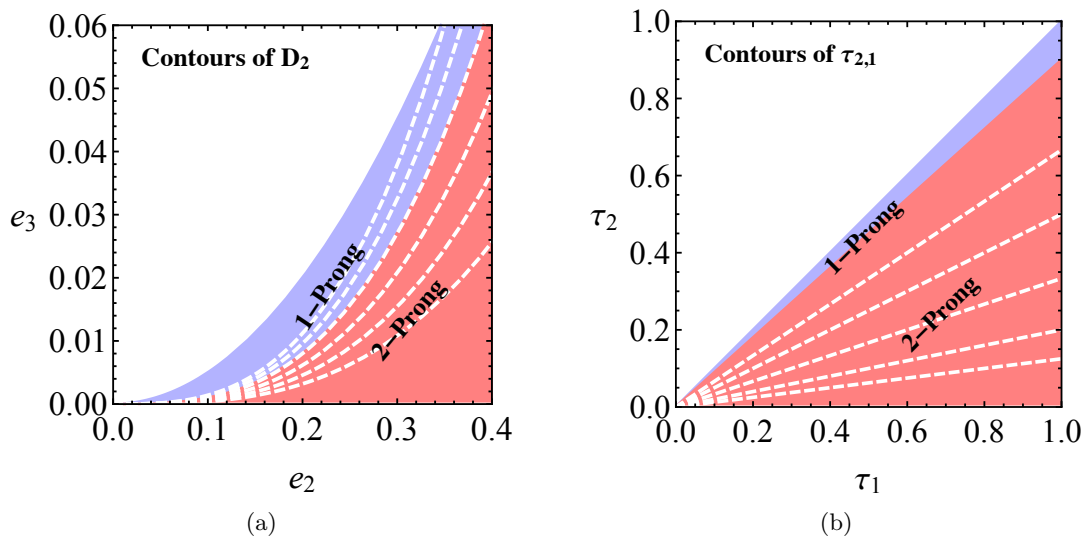


Figure 1: Schematic depiction of the phase space for (a) the energy correlation functions e_2, e_3 and (b) the N -subjettiness observables τ_1, τ_2 . In both cases, contours of the relevant ratio observable, D_2 or $\tau_{2,1}$, are shown as white dashed curves. These ratios are chosen such that the contours cleanly separate the 1- and 2-prong regions of phase space.

Beyond their discrimination power, these observables have nice analytic properties. First, since they can be written as a sum over particles in the jet without reference to external axes, they are automatically “recoil-free” [74, 87–90]. Second, since they have well-defined behavior in various soft and collinear limits, they are amenable to resummed calculations; in Ref. [58], D_2 was calculated to next-to-leading-logarithmic (NLL) accuracy in e^+e^- for both signal (boosted Z) and background (QCD) jets.

The basic structure of the e_2, e_3 phase space is shown in Fig. 1a and discussed in more detail in Refs. [58, 65]. Signal jets which have resolved 2-prong structure live in the region of phase space satisfying $e_3 \ll (e_2)^3$, whereas QCD background jets with 1-prong structure live in the phase space region defined by $(e_2)^3 \ll e_3 \ll (e_2)^2$. The observable D_2 is designed to define contours which cleanly separate the 1-prong and 2-prong regions of phase space, and therefore identifies the extent to which a jet is 1- or 2-prong-like.

Observables for boosted top tagging have also been proposed using the energy correlation functions, namely the C_3 observable [74],

$$C_3^{(\beta)} = \frac{e_4^{(\beta)} e_2^{(\beta)}}{(e_3^{(\beta)})^2}, \quad (2.6)$$

and the D_3 observable [66],

$$D_3^{(\alpha, \beta, \gamma)} = \frac{e_4^{(\gamma)} (e_2^{(\alpha)})^{\frac{3\gamma}{\alpha}}}{(e_3^{(\beta)})^{\frac{3\gamma}{\beta}}} + x \frac{e_4^{(\gamma)} (e_2^{(\alpha)})^{\frac{2\gamma}{\beta}-1}}{(e_3^{(\beta)})^{\frac{2\gamma}{\beta}}} + y \frac{e_4^{(\gamma)} (e_2^{(\alpha)})^{\frac{2\beta}{\alpha}-\frac{\gamma}{\alpha}}}{(e_3^{(\beta)})^2}. \quad (2.7)$$

Here, x and y are constants given in Ref. [66] that depend on the jet mass and p_T . The C_3 observable does not exhibit particularly good discrimination power, and while D_3 , which was constructed using the power counting approach, performs well, it has a complicated functional form. For the boosted top study in Sec. 4, we compare to a simplified version of the D_3 observable

$$D_3^{(\beta)} = \frac{e_4^{(\beta)} \left(e_2^{(\beta)} \right)^3}{\left(e_3^{(\beta)} \right)^3}, \quad (2.8)$$

obtained by setting $x = y = 0$, which behaves well on groomed jets. Unlike its more complicated cousin, this simplified D_3 has only a single angular exponent.

We also find it interesting to compare our new observables to N -subjettiness. The (normalized) N -subjettiness observable τ_N [82, 83] is defined as⁵

$$\tau_N^{(\beta)} = \sum_{1 \leq i \leq n_J} z_i \min \left\{ \theta_{i1}^\beta, \dots, \theta_{iN}^\beta \right\}. \quad (2.9)$$

Here, the angle θ_{iK} is measured between particle i and subject axis K in the jet. As for the case of the energy correlation functions, a number of different possible measures can be used to define θ_{iK} . For our LHC studies, we take $\theta_{iK} = R_{iK}$, analogously to Eq. (2.2).

Unlike the energy correlation functions of Eq. (2.1), which correlate groups of n particles within the jet, N -subjettiness divides a jet into N sectors and correlates the particles in each sector with their corresponding axis. Thus, implicit in the definition of N -subjettiness in Eq. (2.9) is the definition of appropriate N -subjettiness axes. Different definitions of the axes can lead to different behaviors of the observable, particularly away from the resolved limit [94]. A natural definition is to choose the axes that minimize the value of τ_N itself [83], as is done for the classic e^+e^- event shape thrust [95]. Exact minimization is computationally challenging, though, so a number of definitions which approximate the minimum are used instead, which are provided in the `Nsubjettiness` FASTJET CONTRIB [84, 85].

The relevant N -subjettiness ratio observables are

$$\tau_{2,1}^{(\beta)} = \frac{\tau_2^{(\beta)}}{\tau_1^{(\beta)}}, \quad \tau_{3,2}^{(\beta)} = \frac{\tau_3^{(\beta)}}{\tau_2^{(\beta)}}. \quad (2.10)$$

Here, $\tau_{2,1}$ is designed to be small when a jet has well-resolved 2-prong substructure, making it useful for boosted $W/Z/H$ tagging. Similarly, $\tau_{3,2}$ is designed to be small in the 3-prong limit, useful for boosted tops. The observable $\tau_{2,1}$ was calculated in e^+e^- collisions for signal (boosted Z) jets at N³LL accuracy [39].

The phase space for τ_1 , τ_2 is shown schematically in Fig. 1b, along with contours of constant $\tau_{2,1}$. Background QCD jets are defined by the linear scaling $\tau_2 \sim \tau_1$, whereas signal jets are defined by $\tau_2 \ll \tau_1$. This phase space structure is different from that of the e_2 and e_3 observables shown in Fig. 1a, where the phase space for background QCD

⁵This observable is based on the global event shape N -jettiness [91], which has recently been used to define the XCONE jet algorithm [92, 93].

jets is defined by two boundaries with distinct scalings. It is this fact which ultimately leads to many of the differences seen between D_2 and $\tau_{2,1}$, including the fact that the $\tau_{2,1}$ distribution is more stable as a function of jet mass and p_T . The phase space for $\tau_{3,2}$ is similar to $\tau_{2,1}$, to be contrasted with the complicated phase space for D_3 [66]. Using the generalized energy correlation functions, we can define new axes-free observables that mirror the phase space structures of $\tau_{2,1}$ and $\tau_{3,2}$, thereby exhibiting similar scaling and stability behaviors, particularly for groomed jets. This will be discussed for $\tau_{3,2}$ in Sec. 4 and for $\tau_{2,1}$ in Sec. 5.

2.2 Soft Drop Grooming

Two powerful tools which have emerged from the study of jet substructure are groomers [41, 42, 75–78] and pileup mitigation techniques [96–102], both of which remove soft radiation from a jet. Groomers have proven to be useful both for removing jet contamination as well as for identifying hard multi-prong substructure within a jet. In this paper, we use the soft drop [86] groomer with $\beta = 0$, which coincides with the modified mass drop procedure [41, 42] with $\mu = 1$. The soft drop groomer exhibits several theoretical advantages over other groomers; in particular, it removes non-global logarithms [103] to all orders, and it mitigates the process dependence of jet spectra. The soft-dropped groomed jet mass has recently been calculated to NNLL accuracy [60, 61].

Starting from a jet identified with an IRC safe jet algorithm (such as anti- k_t [104]), the soft drop algorithm is defined using Cambridge/Aachen (C/A) reclustering [105–107]. Specializing to the case of $\beta = 0$, the algorithm proceeds as follows:

1. Recluster the jet using the C/A clustering algorithm, producing an angular-ordered branching history for the jet.
2. Step through the branching history of the reclustered jet. At each step, check the soft drop condition

$$\frac{\min [p_{Ti}, p_{Tj}]}{p_{Ti} + p_{Tj}} > z_{\text{cut}}. \quad (2.11)$$

Here, z_{cut} is a parameter defining the scale below which soft radiation is removed. If the soft drop condition is not satisfied, then the softer of the two branches is removed from the jet. This process is then iterated on the harder branch.

3. The soft drop procedure terminates once the soft drop condition is satisfied.

Given a jet that has been groomed with the soft drop procedure, we can then measure any IRC safe observable on this jet and it will remain IRC safe. As we will see, because soft drop removes soft radiation from a jet, power-counting arguments for groomed jets can be dramatically different than those for ungroomed jets. This is previewed in Fig. 2, where the phase space for D_2 is substantially modified by the removal of soft radiation.

More general groomers are expected to give rise to similar power-counting modifications. For example, the soft drop condition in Eq. (2.11) can be generalized to include

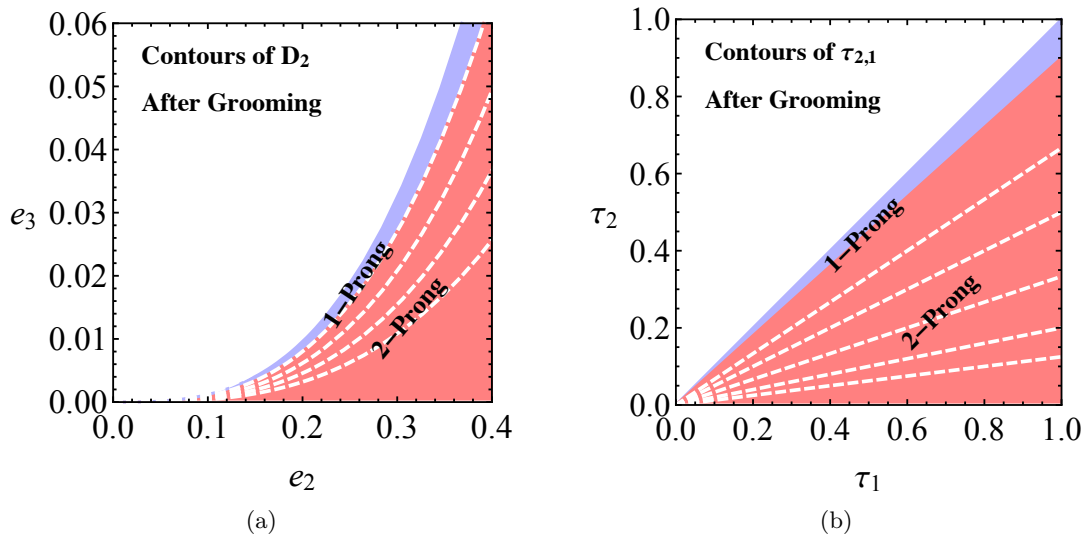


Figure 2: Same as Fig. 1, but after applying jet grooming. The upper-boundary of phase space for D_2 is modified by removing soft radiation, while the parametric behavior of $\tau_{2,1}$ is unchanged. This modified phase space for 2-prong discriminants will be discussed in more detail in Sec. 5.

an angular weighting exponent β , which controls the aggressiveness of the groomer, and we expect deviations away from our default of $\beta = 0$ to yield similar behavior, so long as the groomer continues to remove parametrically soft particles. We also expect that other groomers such as trimming [78], which is used heavily by the ATLAS experiment, will behave similarly for the same value of z_{cut} . We leave a detailed study of other groomers to future work.

2.3 Power Counting the Soft/Collinear Behavior

An efficient approach for studying jet substructure is power counting [65], which allows one to determine the parametric scaling of observables. This parametric behavior is determined by the soft and collinear limits of QCD and is robust to hadronization or modeling in parton shower generators. Here, we briefly review the salient features of power counting, using the 2-point energy correlator as an example. We refer readers interested in a more detailed discussion to the original paper.

High-energy QCD jets are dominated by soft and collinear radiation, a language which will be used frequently throughout this paper. Since QCD is approximately conformal, there is no intrinsic energy or angular scale associated with this radiation.⁶ By applying a measurement to a jet, though, one introduces a scale, which then determines the scaling of soft and collinear radiation. The simple observation that all scales are set by the measure-

⁶We ignore the scale Λ_{QCD} for this discussion, focusing on regions of phase space dominated by perturbative dynamics. While Λ_{QCD} plays an important role in certain phase space regions, for IRC safe observables it contributes only a power-suppressed contribution away from singular limits.

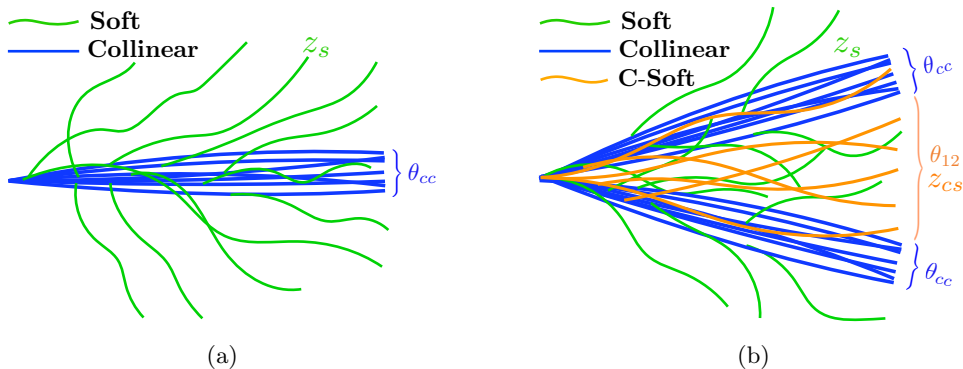


Figure 3: (a) Schematic of a 1-prong jet, showing the dominant soft (green) and collinear (blue) radiation, as well as the characteristic scales z_s and θ_{cc} . (b) Schematic of a 2-prong jet, showing the dominant soft (green), collinear (blue), and collinear-soft (orange) radiation, as well as the characteristic scales, z_s , θ_{cc} , z_{cs} , and θ_{12} .

ment itself allows for a powerful understanding of the jet’s energy and angular structure. Arguments along these lines are ubiquitous in the effective field theory (EFT) community. For example, in Soft Collinear Effective Theory (SCET) [108–111], they are used to identify the appropriate EFT modes required to describe a particular set of measurements.

In the context of power counting, soft and collinear emissions are defined by their parametric scalings. A soft emission, denoted by s , is defined by

$$z_s \ll 1, \quad \theta_{sx} \sim 1. \quad (2.12)$$

Here, z_s is the momentum fraction, as defined in Eq. (2.2), and θ_{sx} is the angle to any other particle x in the jet, including other soft particles. The scaling $\theta_{sx} \sim 1$ means that θ_{sx} is not assigned any parametric scaling associated with the measurement. A collinear emission, denoted by c , is defined by

$$z_c \sim 1, \quad \theta_{cc} \ll 1, \quad \theta_{cs} \sim 1. \quad (2.13)$$

Here, θ_{cc} is the angle between two collinear particles, while θ_{cs} is the angle between a collinear particle and a soft particle. In an EFT context, overlaps between soft and collinear regions are systematically removed using the zero-bin procedure [112], but this is not relevant for the arguments here. The soft and collinear modes are illustrated in Fig. 3a and their scalings are summarized in Table 1a.

We now use the simple example of e_2 to demonstrate how an applied measurement sets the scaling of soft and collinear radiation.⁷ The analysis of more general observables

⁷In this analysis, we do not consider the scale set by the jet radius, R . For $R \ll 1$, the jet radius must also be considered in the power counting and the scale R appears in perturbative calculations. For recent work on the resummation of logarithms associated with this scale, see Refs. [113–116].

Mode	Energy	Angle
soft	z_s	1
collinear	1	θ_{cc}

(a)

Mode	Energy	Angle
soft	z_s	1
collinear	1	θ_{cc}
c-soft	z_{cs}	θ_{12}

(b)

Table 1: Summary of the modes in Fig. 3: (a) 1-prong jets versus (b) 2-prong jets.

proceeds analogously. Repeating Eq. (2.1) for convenience, the 2-point energy correlation function is

$$e_2^{(\beta)} = \sum_{1 \leq i < j \leq n_J} z_i z_j \theta_{ij}^\beta. \quad (2.14)$$

If we only consider regions of phase space where $e_2 \ll 1$, such that we have a well-defined collimated jet, all particles in the jet either have small z_i or small θ_{ij} . In this phase space region, the observable is indeed dominated by soft and collinear emissions.

To determine the scaling of z_s and θ_{cc} in terms of the observable, we can consider the different possible contributions to e_2 : soft-soft correlations, soft-collinear correlations, and collinear-collinear correlations. Parametrically, e_2 can therefore be written as

$$e_2^{(\beta)} \sim \sum_s z_s z_s \theta_{ss}^\beta + \sum_{s,c} z_s z_c \theta_{cs}^\beta + \sum_c z_c z_c \theta_{cc}^\beta. \quad (2.15)$$

Expanding this result to leading order in z_s and θ_{cc} , we find

$$e_2^{(\beta)} \sim \sum_s z_s + \sum_c \theta_{cc}^\beta. \quad (2.16)$$

For simplicity, we drop the summation symbol, writing

$$e_2^{(\beta)} \sim z_s + \theta_{cc}^\beta. \quad (2.17)$$

Since we have only measured a single observable, e_2 , it sets the only scale in the jet, and there is no measurement to further distinguish the scalings of soft and collinear particles. We therefore find the scaling of z_s and θ_{cc} in terms of the observable,

$$z_s \sim e_2^{(\beta)}, \quad \theta_{cc} \sim \left(e_2^{(\beta)}\right)^{1/\beta}. \quad (2.18)$$

More generally, after identifying all parametrically different modes that can contribute to a set of measurements, the scaling of those modes is determined by the measured observables.

In this paper, we are interested not only in jets with soft and collinear radiation, but also in jets which have well-resolved substructure. In addition to the strictly soft and collinear modes which are found in Fig. 3a, a jet with well-resolved substructure also includes radiation emitted from the dipoles within the jet, shown in orange for the particular case of a 2-prong jet in Fig. 3b. This radiation is referred to as “collinear-soft” (or just

“c-soft”) as it has a characteristic angle θ_{12} defined by the opening angle of the subjects, as well as a momentum fraction $z_{cs} \ll 1$, both of which are set by the measurement. The appropriate EFT description for multi-prong substructure is referred to as SCET₊ [55, 117–119], and the scaling of the collinear-soft mode is summarized in Table 1b. Using the mode structure of multi-prong jets, it is straightforward to apply power-counting arguments to a wide variety of n -prong jet substructure observables, as demonstrated in Secs. 4 and 5.

We also apply power-counting arguments to groomed jets after soft drop has been applied. The effect of the grooming algorithm is not just to remove jet contamination, but also to modify the power counting in interesting, and potentially useful, ways. As discussed in Sec. 2.2, soft drop with $\beta = 0$ is defined with a single parameter z_{cut} , which determines the scale below which soft radiation is removed. To perform a proper power-counting analysis, one should also incorporate the scale z_{cut} and consider different cases depending on the relative scaling of z_{cut} and z_s . For simplicity, we ignore this complication through most of this paper and assume that the soft drop procedure simply removes the soft modes. That said, the residual soft scaling will matter for the quark/gluon study in Sec. 6. For a more detailed discussion, and a proper treatment of the scale z_{cut} involving collinear-soft modes, see Refs. [60, 61].

3 Enlarging the Basis of Jet Substructure Observables

An important goal of jet substructure is to design observables that efficiently identify particular features within a jet. A popular, and theoretically well-motivated, approach is to construct observables from combinations, often ratios, of IRC safe jet shapes.⁸ Such observables are widely employed at the LHC, and have proven to be both experimentally useful and theoretically tractable. Indeed, the observables reviewed in Sec. 2.1— $\tau_{2,1}$, $\tau_{3,2}$, C_2 , and D_2 —are all of this form.

Essential to this approach is a flexible basis of IRC safe observables from which to build discriminants. While the original energy correlators are indeed a useful basis, they are still somewhat restrictive. For example, the phase space structure of e_2 and e_3 in Fig. 1a is completely fixed, as are all of the parametric properties inherited from this structure, such that D_2 is the only combination that parametrically distinguishes 1- and 2-prong substructure.

In this section, we enlarge the basis of jet substructure observables by defining generalizations of the energy correlation functions, allowing for a more general angular dependence than considered in Eq. (2.1). These new observables are flexible building blocks, which we use in the rest of this paper to identify promising tagging observables using power-counting techniques.⁹

⁸These ratios are not themselves IRC safe, but are instead Sudakov safe [120, 121]. For a discussion of Sudakov safety for the case of D_2 , see Ref. [58]. For this reason, the ratio observables we construct in this paper cannot be written in the form of Eq. (3.1), even though their ${}_{\nu}e_n^{(\beta)}$ ingredients can.

⁹An alternative approach to identifying specific features within jets is machine learning, which has seen significant recent interest [67–73]. The contrast between these strategies has been dubbed “deep thinking” versus “deep learning”. In the deep thinking approach pursued here, the goal is to identify the physics principles that lead to discrimination power, focusing on observables with desirable properties for

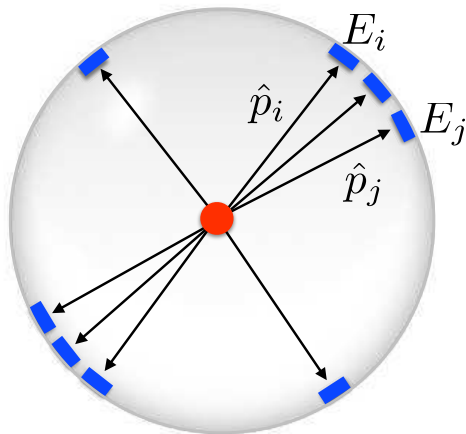


Figure 4: Schematic depiction of a hard scattering event. A general IRC safe observable can be constructed by summing over all energy deposits, E_i , in an event, with a symmetric angular weighting function depending on the dimensionless unit vectors \hat{p}_i .

3.1 General Structure of Infrared/Collinear Safe Observables

In order to engineer the phase space structure of observables to have specific properties, we first need to systematically understand the structure of IRC safe observables that probe n -particle correlations. The general structure of an IRC safe observable is shown schematically in Fig. 4, where any IRC safe observable can be constructed from the energy deposits and angular information on the sphere. In the pp case, of course, one typically uses the longitudinally boost-invariant quantities p_T and R_{ij} , but the following argument is insensitive to that coordinate change.

As shown in Ref. [122–125], any IRC safe observable can be constructed from the following (complete) basis of observables¹⁰

$$F_N(\{p_i\}) = \sum_{i_1} \sum_{i_2} \dots \sum_{i_N} E_{i_1} E_{i_2} \dots E_{i_N} f_N(\hat{p}_{i_1}, \hat{p}_{i_2}, \dots, \hat{p}_{i_N}), \quad (3.1)$$

where E_i is the energy of particle i , \hat{p}_i is a dimensionless unit vector describing its direction, and f_N is a symmetric function of its arguments. For IRC safety, we must further demand that the function f_N vanishes when any two particles become collinear. Note that Eq. (3.1) is a linear function of the momenta of the particles and a symmetric function of the angles. This basis of observables are referred to in the literature as C -correlators [122–125].

Since the above discussion is completely general, it is not immediately obvious that it is useful for jet substructure studies. Still, Eq. (3.1) has the interesting feature that, while

first-principles calculations. In the deep learning approach, the goal is to use reliable training samples to optimize the discrimination power and, in many cases, visualize the underlying physics. Ultimately, one would want to merge these two approaches, which could help avoid theoretical blindspots in the cataloging of observables and mitigate modeling uncertainties inherent in training samples. Detailed studies in data, ideally with high purity samples, will also be needed for a complete understanding.

¹⁰With a completely generic angular weighting function, f_N , this basis is of course overcomplete.

the dependence on the energies is fixed by IRC safety, the angular function f_N is much less restricted and can be chosen for specific purposes. The original energy correlators in Eq. (2.1) are a specific case of Eq. (3.1), where, up to an overall normalization, the angular weighting function is

$$e_N^{(\beta)} : \quad f_N(\hat{p}_{i_1}, \hat{p}_{i_2}, \dots, \hat{p}_{i_N}) = \prod_{s < t \in \{i_1, i_2, \dots, i_n\}} \theta_{st}^\beta. \quad (3.2)$$

The key observation is that by considering alternative angular weighting functions for n -point correlators beyond Eq. (3.2), we can define a more flexible basis of observables for jet substructure studies.

3.2 New Angles on Energy Correlation Functions: ${}_v e_n^{(\beta)}$

There are many known decompositions of the angular function f_N —including Fox-Wolfram moments [126, 127] and orthogonal polynomials on the sphere [128]—but these are not necessarily optimal for jet substructure. The reason is that jets with well-resolved subjets exhibit a hierarchy of distinct angular scales, so we need to design f_N to identify hierarchical—instead of averaged—features within a jet.

As seen in Eq. (3.2), the original energy correlation functions do capture multiple angular scales, but they do so all at once; it would be preferable if f_N could identify one angular scale at a time in order to isolate different physics effects. Furthermore, to make power-counting arguments more transparent, we want f_N to exhibit homogeneous angular scaling, such that each term in Eq. (3.1) has a well-defined scaling behavior without having to perform a non-trivial expansion in the soft and collinear limits.

With these criteria in mind, we can now translate the general language of IRC safe observables into a useful basis for jet substructure studies. The angular function f_N has to be symmetric in its arguments, and the simplest symmetric function that preserves homogeneous scaling is the min function.¹¹ This leads us to the generalized energy correlation functions, which depend on n factors of the particle energies and v factors of their pairwise angles,

$${}_v e_n^{(\beta)} = \sum_{1 \leq i_1 < i_2 < \dots < i_n \leq n_J} z_{i_1} z_{i_2} \dots z_{i_n} \prod_{m=1}^v \min_{s < t \in \{i_1, i_2, \dots, i_n\}}^{(m)} \left\{ \theta_{st}^\beta \right\}, \quad (3.3)$$

where $\min^{(m)}$ denotes the m -th smallest element in the list. For a jet consisting of fewer than n particles, ${}_v e_n$ is defined to be zero. More explicitly, the three arguments of the generalized energy correlation functions are as follows.

- The subscript n , appearing to the right of the observable, denotes the number of particles to be correlated. This plays the same role as the n subscript for the standard e_n energy correlators in Eq. (2.1).

¹¹The appearance of min can also be viewed as the lowest-order Taylor expansion of a more generic observable, which should be a good approximation in the case of small radius jets. This can be seen explicitly in App. A, where different functional forms are compared that give the same quantitative behavior as the min version here. Another motivation for the min definition is that it naively behaves more similarly to thrust [95] or N -jettiness [91], though we emphasize that ${}_v e_n$ does not rely on external axes.

- The subscript v , appearing to the left of the observable, denotes the number of pairwise angles entering the product. By definition, we take $v \leq \binom{n}{2}$, and the minimum then isolates the product of the v smallest pairwise angles.
- The angular exponent $\beta > 0$ can be used to adjust the weighting of the pairwise angles, as in Eq. (2.1).

For the special case of $v = \binom{n}{2}$, the generalized energy correlators reduce to the standard ones in Eq. (2.1), with ${}_1e_2 \equiv e_2$, ${}_3e_3 \equiv e_3$, ${}_6e_4 \equiv e_4$, and so on for the higher-point correlators.

Compared to the original energy correlators, the generalization in Eq. (3.3) allows more flexibility in the angular scaling; this simplifies the construction of useful ratios and extends the possible applications of energy correlators. In the case of boosted top tagging, for example, the standard $e_4 = {}_6e_4$ observable involves six different pairwise angles. A decaying boosted top quark, however, does not have six characteristic angular scales, so most of these angles are redundant and only serve to complicate the structure of the observable. This is reflected in the definition of D_3 in Eq. (2.7), which involves three distinct terms [66].

To make more explicit the definition in Eq. (3.3), we summarize the particular correlators used in our case studies below. For boosted 2-prong tagging in Sec. 5, we use the 2-point energy correlation function

$${}_1e_2^{(\beta)} \equiv e_2^{(\beta)} = \sum_{1 \leq i < j \leq n_J} z_i z_j \theta_{ij}^\beta, \quad (3.4)$$

whose definition is unique, since it only involves only a single pairwise angle. We also need the 3-point correlators, which have three variants probing different angular structures:¹²

$$\begin{aligned} {}_1e_3^{(\beta)} &= \sum_{1 \leq i < j < k \leq n_J} z_i z_j z_k \min \left\{ \theta_{ij}^\beta, \theta_{ik}^\beta, \theta_{jk}^\beta \right\}, \\ {}_2e_3^{(\beta)} &= \sum_{1 \leq i < j < k \leq n_J} z_i z_j z_k \min \left\{ \theta_{ij}^\beta \theta_{ik}^\beta, \theta_{ij}^\beta \theta_{jk}^\beta, \theta_{ik}^\beta \theta_{jk}^\beta \right\}, \\ e_3^{(\beta)} \equiv {}_3e_3^{(\beta)} &= \sum_{1 \leq i < j < k \leq n_J} z_i z_j z_k \theta_{ij}^\beta \theta_{ik}^\beta \theta_{jk}^\beta. \end{aligned} \quad (3.5)$$

Interestingly, we are able to construct powerful observables from each of these three 3-point correlators, resulting in different tagging properties.

For boosted top tagging in Sec. 4, we also need the 4-point correlators. There are six

¹²For ${}_2e_3$, note that $\min\{a, b, c\} \times \min^{(2)}\{a, b, c\} = \min\{ab, ac, bc\}$.

possible variants, but we only study three of them in the body of the text:

$$\begin{aligned}
{}_1e_4^{(\beta)} &= \sum_{1 \leq i < j < k < \ell \leq n_J} z_i z_j z_k z_\ell \min \left\{ \theta_{ij}^\beta, \theta_{ik}^\beta, \theta_{jk}^\beta, \theta_{i\ell}^\beta, \theta_{j\ell}^\beta, \theta_{k\ell}^\beta \right\}, \\
{}_2e_4^{(\beta)} &= \sum_{1 \leq i < j < k < \ell \leq n_J} z_i z_j z_k z_\ell \min \left\{ \theta_{ij}^\beta, \theta_{ik}^\beta, \theta_{jk}^\beta, \theta_{i\ell}^\beta, \theta_{j\ell}^\beta, \theta_{k\ell}^\beta \right\} \\
&\quad \times \min^{(2)} \left\{ \theta_{ij}^\beta, \theta_{ik}^\beta, \theta_{jk}^\beta, \theta_{i\ell}^\beta, \theta_{j\ell}^\beta, \theta_{k\ell}^\beta \right\}, \\
&\quad \vdots \\
e_4^{(\beta)} \equiv {}_6e_4^{(\beta)} &= \sum_{1 \leq i < j < k < \ell \leq n_J} z_i z_j z_k z_\ell \theta_{ij}^\beta \theta_{ik}^\beta \theta_{jk}^\beta \theta_{i\ell}^\beta \theta_{j\ell}^\beta \theta_{k\ell}^\beta,
\end{aligned} \tag{3.6}$$

where $\min^{(2)}$ is again the second smallest element in the list. Here, we see the simplicity in the angular structure of ${}_1e_4$ and ${}_2e_4$, as compared to ${}_6e_4$ which involves all six angles. The vertical dots denote other 4-point correlation functions; we have not found them to be particularly useful, but they might have applications in (and beyond) jet substructure.

When constructing jet substructure observables, it is often desirable to work with ratios that are approximately boost invariant. Since the different generalized correlators probe a different number of energy fractions and pairwise angles, each scales differently under Lorentz boosts. Under a boost γ along the jet axis and assuming a narrow jet, the energies and angles scale as

$$z_i \rightarrow z_i, \quad \theta_{ij} \rightarrow \gamma^{-1} \theta_{ij}. \tag{3.7}$$

This implies that the transformation of ${}_v e_n$ under boosts along the jet axis is determined solely by the v index,

$${}_v e_n^{(\beta)} \rightarrow \gamma^{-v\beta} {}_v e_n^{(\beta)}. \tag{3.8}$$

Therefore, another way of interpreting the different ${}_v e_n$ is as ways of probing n particle correlations with different properties under Lorentz boosts. The v index therefore broadens the set of boost-invariant combinations that can be formed.

Finally, we remark that the definition in Eq. (3.3) is certainly not unique, and we explore a few alternative definitions in App. A that reduce to the min function in collinear limits. To further generalize Eq. (3.3) while maintaining homogeneous scaling, one could use different angular exponents depending on the ordering of the angles. For the cases that we consider, though, we find that ${}_v e_n$ is sufficiently general to provide excellent performance while keeping the form of the observable (relatively) simple. That said, we expect alternative f_N functions to also be useful, and their performance could be studied using the same power-counting techniques pursued here.

3.3 New Substructure Discriminants

Our case studies are based primarily on three series of observables formed from the generalized correlators. We summarize their definitions here, and study their discrimination power in the forthcoming sections using both power-counting arguments and parton shower generators.

3.3.1 The M_i Series

The M_i series of observables is defined as

$$M_i^{(\beta)} = \frac{1e_{i+1}^{(\beta)}}{1e_i^{(\beta)}}. \quad (3.9)$$

This observable is dimensionless, being formed as a ratio of dimensionless observables. As can be seen from Eq. (3.8), it is also invariant to boosts along the jet axis, since one angular factor appears in both the numerator and denominator.

These observables are constructed to identify i hard prongs, but due to their limited angular structure, they are only effective when acting on suitably groomed jets. The main example of the M_i series that we will consider explicitly in this paper is

$$M_2^{(\beta)} = \frac{1e_3^{(\beta)}}{1e_2^{(\beta)}}, \quad (3.10)$$

which provides an example of a 2-prong substructure observable that only performs well after grooming. In App. B.1, we briefly discuss the behavior of M_3 for boosted top tagging, where we argue that a more aggressive grooming strategy would be needed to make M_3 perform well.

3.3.2 The N_i Series

We also define the N_i series of observables as

$$N_i^{(\beta)} = \frac{2e_{i+1}^{(\beta)}}{(1e_i^{(\beta)})^2}. \quad (3.11)$$

As with the M_i series, the N_i series is dimensionless, and from Eq. (3.8), it is boost invariant, as two angular factors appear in both the numerator and denominator. Indeed, the fact that the 2-point correlation function appears squared in the denominator is fixed by boost invariance.

Two particular examples we find useful for this paper are

$$N_2 = \frac{2e_3^{(\beta)}}{(1e_2^{(\beta)})^2}, \quad (3.12)$$

which is a powerful boosted $W/Z/H$ tagger, and

$$N_3 = \frac{2e_4^{(\beta)}}{(1e_3^{(\beta)})^2}, \quad (3.13)$$

which is a powerful boosted top tagger on groomed jets. More generally, N_i should be effective as an i -prong tagger, as discussed in App. C, at least for groomed jets.

The N_i observables take their name from the fact that in the limit of a resolved jet, they behave parametrically like the N -subjettiness ratio observables, as discussed in Secs. 4 and 5. Despite their similarity to N -subjettiness, the N_i observables achieve their discrimination power in a substantially different manner, which has both theoretical and experimental advantages.

3.3.3 The U_i Series

Finally, we consider the U_i series of observables defined as

$$U_i^{(\beta)} = {}_1e_{i+1}^{(\beta)}, \quad (3.14)$$

which are designed for quark/gluon discrimination. Note that unlike M_i and N_i , the U_i observables are not boost invariant. For the case $i = 1$, U_1 coincides with the usual quark/gluon discriminants formed from the energy correlation functions [74], namely

$$U_1^{(\beta)} = C_1^{(\beta)} = {}_1e_2^{(\beta)} = e_2^{(\beta)}, \quad (3.15)$$

which probe single soft particle correlations within the jet. For $i > 1$, the U_i observables probe multi-particle correlations within the jet in a specific way that is useful for quark/gluon discrimination.

4 Simplifying Observables for Boosted Top Tagging

Boosted top tagging has achieved significant attention at the LHC, with a large number of proposed observables to distinguish 3-prong hadronic top jets from the QCD background [74, 82, 83, 129–142]. In addition to b -tagging one of the subjets [8, 143–149] and requiring the (groomed) jet mass to be close to $m_t \simeq 172$ GeV, two of the most effective tagging observables are shower deconstruction [137, 150, 151] and the N -subjettiness ratio $\tau_{3,2}$ [82, 83]. Shower deconstruction works by testing the compatibility of a QCD shower model with the observed shower pattern; it is an extremely powerful discriminant, particularly at lower efficiencies. Jet shapes like N -subjettiness are also powerful discriminants, particularly at higher efficiencies. For a detailed discussion and experimental study, see, for example, Refs. [152, 153].

In this section, we use the generalized energy correlation functions to construct N_3 , a simple but powerful boosted top tagger designed for use on groomed jets. Unlike $\tau_{3,2}$, N_3 is defined without reference to external axes, allowing it to achieve better background rejection at high signal efficiencies. Interestingly, in the limit of well-resolved subjets and acting on groomed jets, N_3 has identical power counting to N -subjettiness. The behavior on ungroomed jets is discussed in App. B.2.

4.1 Constructing the N_3 Observable

To detect boosted top jets with hard 3-prong substructure, we can use combinations of 2-point, 3-point, and 4-point correlators. Due to the large number of possible combinations, the power counting approach becomes essential to systematically study the behavior of these observables.

In order to use power counting to probe the boundary between the 3-prong (signal) and 2-prong (background) regions of phase space, one must analyze signal configurations which approach this boundary. For this reason, we consider not only the case of three subjets with equal energies and opening angles, as shown in Fig. 5a, but also the strongly-ordered limit, shown in Fig. 5b, where two of the three prongs become collinear. When

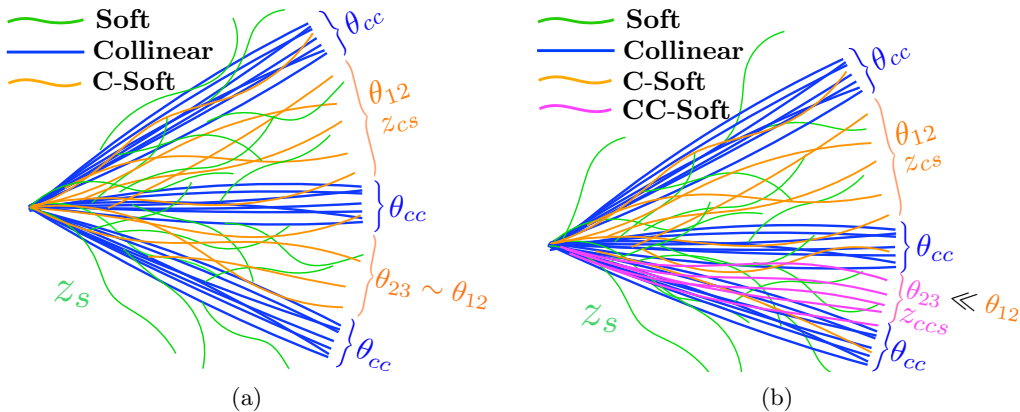


Figure 5: Configurations used in the power-counting analysis for N_3 , showing the modes and scales entering the description of the jets. In (a), the three subjects carry equal energies, and there is no hierarchy between the angles. In (b), each of the subjects carries equal energies, but there is a hierarchy in the opening angles of the jets, requiring an extra collinear-collinear-soft mode, shown in magenta, in the power-counting analysis.

Mode	Energy	Angle
soft	z_s	1
collinear	1	θ_{cc}
c-soft	z_{cs}	θ_{12}
cc-soft	z_{ccs}	θ_{23}

Table 2: A summary of the modes in Fig. 5b which enter the power-counting analysis for boosted top quarks.

the opening angles are hierarchical, the emission modes for each of the dipoles are distinct and must be treated separately, as discussed in Ref. [66]. For lack of a better name, we call these additional modes collinear-collinear-soft modes (shown in magenta in Fig. 5b) to distinguish them from collinear-soft modes (shown in orange). A summary of these different modes, and the scaling of their angles and energies, are given in Table 2. These modes satisfy the relations

$$z_{cs} \ll z_{ccs} \ll 1, \quad \theta_{cc} \ll \theta_{23} \ll \theta_{12} \ll 1. \quad (4.1)$$

Note the reversal of the energy and angle hierarchies: collinear-collinear-soft modes have smaller angles but higher energies than collinear-soft modes. With this slight modification, the power-counting analysis proceeds identically to the simpler case shown in Fig. 3b.

Many experimental analyses use jet shapes as measured on groomed jets, even if the original jet shapes were proposed without grooming. Grooming has the advantage of making jet properties resistant to pileup contamination and it also leads to observables that are more stable as the jet mass and p_T are varied. More generally, grooming techniques

minimize sensitivity to low momentum particles and the corresponding experimental uncertainties associated with their reconstruction. It is also possible to use a combination of groomed and ungroomed (or lightly groomed) substructure discriminants [154, 155]. Here, we design our observable specifically for use on groomed jets, since it will help us identify discriminants that are both stable and high-performing. From the perspective of power counting, grooming simplifies the scaling properties of observables, since we can ignore regions of phase space with soft wide-angle subjets. In the past, such regions caused complications in designing top tagging observables based on energy correlators [66], as seen in the definition of D_3 in Eq. (2.7). After jet grooming, we can drop soft radiation (shown in green in Fig. 5) for the purposes of power counting.

From Eq. (3.6), we have six 4-point correlators we could use to form ratio observables with the 2- and 3-point correlators. To reduce the number of possibilities, we restrict our attention to boost-invariant combinations, but this still leaves many ratios to test. In App. B.3, we outline a systematic strategy to isolate the most promising 3-prong discriminants using power counting. Here, we focus on the best performing observable,

$$N_3^{(\beta)} = \frac{2e_4^{(\beta)}}{(1e_3^{(\beta)})^2}, \quad (4.2)$$

which was presented in Sec. 3.3.2 as a member of the N_i series.

To understand why N_3 is a powerful discriminant on groomed jets, we need to contrast the phase space for 3-prong signal jets versus 2-prong background jets. For the 3-prong top signal, it is sufficient to study the strongly-ordered limit in Fig. 5b, since the balanced case of Fig. 5a can be obtained by setting $z_{ccs} = z_{cs}$ and $\theta_{23} = \theta_{12}$. Using the methods of Sec. 2.3 on the modes from Table 2, we find the following parametric scaling:

$$\begin{aligned} \text{3-prong signal (groomed):} \quad & 1e_3^{(\beta)} \sim \theta_{23}^\beta, \\ & 2e_4^{(\beta)} \sim z_{cs}\theta_{12}^\beta\theta_{23}^\beta + z_{ccs}\theta_{23}^{2\beta} + \theta_{23}^\beta\theta_{cc}^\beta. \end{aligned} \quad (4.3)$$

The dominant background to boosted top quarks are gluon and quark jets, particularly bottom quarks when subjet b -tagging is used [8, 143–149]. While we ordinarily think of these as being 1-prong backgrounds (see Fig. 3a), they are mainly relevant when they feature 2-prong substructure from a hard parton splitting. Therefore, the phase space configuration we have to consider for the background is that of Fig. 3b. Using the modes from Table 1b, we find

$$\begin{aligned} \text{2-prong background (groomed):} \quad & 1e_3^{(\beta)} \sim z_{cs}\theta_{12}^\beta + \theta_{cc}^\beta, \\ & 2e_4^{(\beta)} \sim z_{cs}^2\theta_{12}^{2\beta} + z_{cs}\theta_{12}^\beta\theta_{cc}^\beta + \theta_{cc}^{2\beta}. \end{aligned} \quad (4.4)$$

From these power-counting relations, we now want to derive the scaling of $2e_4$ versus $1e_3$.

For signal jets, $2e_4$ is always smaller than $1e_3$, since they share a factor of θ_{23}^β , but each term in $2e_4$ is also multiplied by parametrically small quantity. In particular, $\theta_{cc} \ll \theta_{23}$ by the assumption of Eq. (4.1), so we have the parametric relation

$$\text{3-prong signal (groomed):} \quad 2e_4^{(\beta)} \ll (1e_3^{(\beta)})^2. \quad (4.5)$$

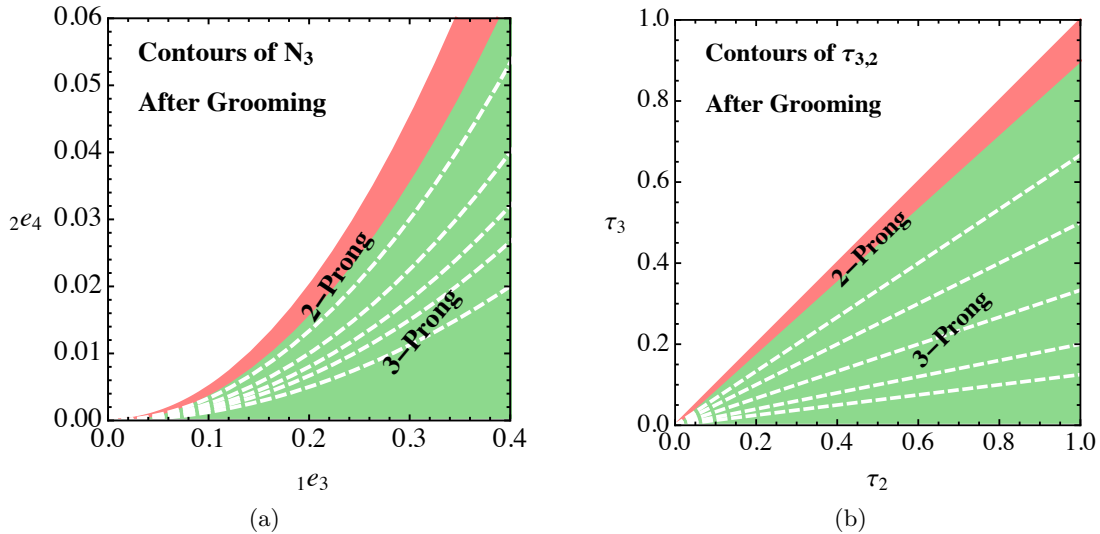


Figure 6: Comparison of the phase space for (a) N_3 and (b) $\tau_{3,2}$ after grooming has been applied. The phase space structure in the two cases is similar, with the background restricted to a single scaling at the upper boundary.

A much more detailed derivation of this scaling, and an illustration of how it can be identified systematically, is presented in App. B.4. For background jets, each term in $2e_4$ is the product of two terms in $1e_3$, so we have the relation

$$\text{2-prong background (groomed):} \quad 2e_4^{(\beta)} \sim (1e_3^{(\beta)})^2. \quad (4.6)$$

This shows that the particular combination chosen to define N_3 is indeed appropriate, since we can isolate the top signal region by making a cut of $N_3 \ll 1$. These phase space relations are shown in Fig. 6a.

To further improve our understanding, it is instructive to compare this with the N -subjettiness ratio $\tau_{3,2}$, whose phase space is shown in Fig. 6b. For strongly-ordered 3-prong substructure, we find

$$\begin{aligned} \text{3-prong signal (groomed):} \quad \tau_2^{(\beta)} &\sim \theta_{23}^\beta \sim 1e_3^{(\beta)}, \\ \tau_3^{(\beta)} &\sim z_{cs}\theta_{12}^\beta + z_{cs}\theta_{23}^\beta + \theta_{cc}^\beta \sim \frac{2e_4^{(\beta)}}{\theta_{23}^\beta}. \end{aligned} \quad (4.7)$$

For 2-prong background jets, we find

$$\text{2-prong background (groomed):} \quad \tau_2^{(\beta)} \sim \tau_3^{(\beta)} \sim z_{cs}\theta_{cs}^\beta + \theta_{cc}^\beta \sim 1e_3^{(\beta)}. \quad (4.8)$$

Remarkably, in both cases, this leads to the relations

$$\begin{aligned} 1e_3^{(\beta)} &\sim \tau_2^{(\beta)}, \\ 2e_4^{(\beta)} &\sim \tau_2^{(\beta)}\tau_3^{(\beta)}. \end{aligned} \quad (4.9)$$

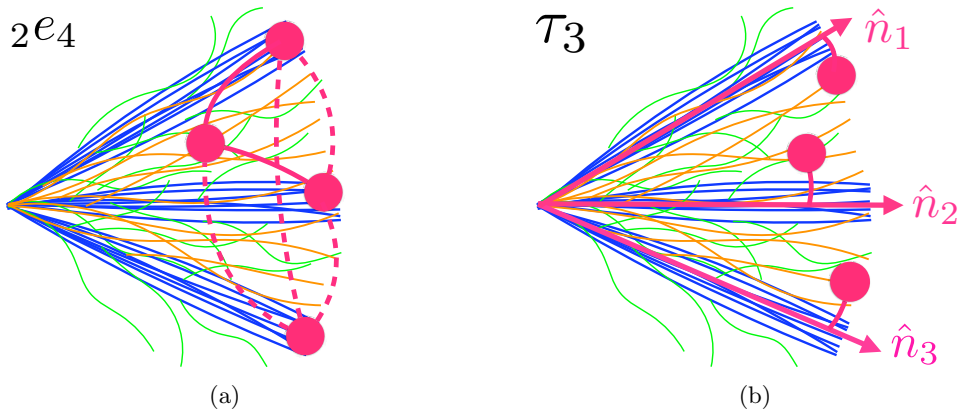


Figure 7: Comparison of the functional structure of (a) $2e_4$ and (b) τ_3 . The $2e_4$ observable correlates quadruplets of particles (and two of their six pairwise angles), while the τ_3 observable correlates particles with axes.

Therefore, on groomed jets, the N_3 and $\tau_{3,2}$ observables are parametrically identical:

$$N_3^{(\beta)} = \frac{2e_4^{(\beta)}}{(1e_3^{(\beta)})^2} \sim \frac{\tau_2^{(\beta)}\tau_3^{(\beta)}}{(\tau_2^{(\beta)})^2} = \frac{\tau_3^{(\beta)}}{\tau_2^{(\beta)}}. \quad (4.10)$$

This result is quite surprising. By summing over groups of four particles and taking double products of their pairwise angles, we have achieved an observable that behaves parametrically like an N -subjettiness ratio.

The observables N_3 and $\tau_{3,2}$ achieve their discrimination power in substantially different ways, as shown schematically in Fig. 7. Each term in $2e_4$ is sensitive to multiple energies and angles and contains cross terms like $\theta_{12}^\beta \theta_{cc}^\beta$. By contrast, N -subjettiness does not contain such cross terms; after determining the axes, each term in the N -subjettiness sum is independent of the presence of other subjets. Despite these differences, Eq. (4.9) shows that the 4-point correlation function factorizes into a product of lower-point N -subjettiness observables, yielding the same parametric behavior in the resolved limit.

While there are no parametric difference between N_3 and $\tau_{3,2}$, our parton shower study will show that N_3 exhibits improved discrimination power on groomed jets, particularly at high efficiencies. Part of the reason this occurs is because N_3 is defined without respect to subjet axes. This not only offers the practical advantage of not needing to specify an axes-finding algorithm, but it also has an effect on the behavior of N_3 away from the power-counting regime. Recall that N -jettiness was originally designed to isolate regions of phase space where there are N well-resolved jets [91]. In this limit, the axes are well defined and independent of the particular axes definition up to power corrections. When used in jet substructure, however, N -subjettiness is used both in the limit of well-resolved subjets as well as in the limit of unresolved subjets. Indeed, in many substructure analyses, relatively loose requirements are placed on N -subjettiness, such that the $\tau_{3,2}$ cut is placed precisely in the unresolved region. Here, N -subjettiness can exhibit pathological behavior related to the axes choice [94]. By contrast, the N_3 observable, being composed simply as sums over

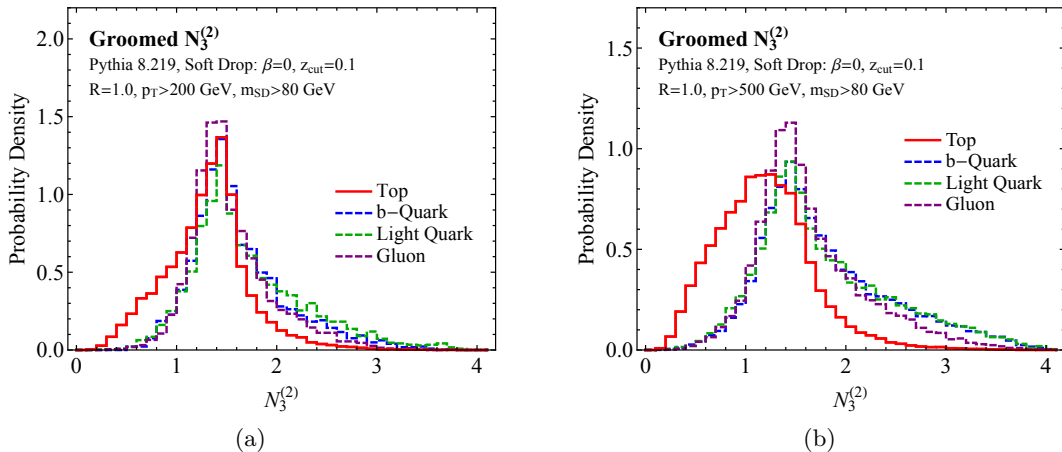


Figure 8: Distributions of N_3 on groomed jets for (a) $p_{TJ} = 200$ GeV and (b) $p_{TJ} = 500$ GeV, comparing signal top jets to background QCD jets initiated from b -quarks, light quarks, and gluons.

the jet constituents, is well behaved throughout the entire jet spectrum, and this will be reflected in its improved performance.

4.2 Performance in Parton Showers

Having understood the power counting of N_3 on groomed jets, we now study its behavior in parton shower generators, comparing N_3 with both $\tau_{3,2}$ and the simplified version of D_3 defined in Eq. (2.8). The comparison to $\tau_{3,2}$ is particularly interesting, since the parametrics in Eq. (4.10) suggest it should perform similarly to N_3 in the resolved limit.

For our parton shower study, we generate background QCD jets from $pp \rightarrow jj$ events, where we consider separately the cases of $j = g$ (gluon) and $j = u$ (representative of light quarks). We also consider the case of b -quark backgrounds, which are interesting to treat separately due to recent advances in b -tagged substructure [8, 143–149]; heavy quarks were generated from the process $pp \rightarrow b\bar{b}$. The boosted top signal is generated from $pp \rightarrow t\bar{t}$ events, with both tops decaying hadronically.

Events were generated with MADGRAPH5 2.3.3 [156] at the 13 TeV LHC and showered with PYTHIA 8.219 [157, 158] with underlying event and hadronization implemented with the default settings. Anti- k_T [104] jets with radius $R = 1.0$ were clustered in FASTJET 3.2.0 [84] using the Winner Take All (WTA) recombination scheme [90, 159].¹³ The energy correlation functions and N -subjettiness ratio observables were calculated using the EnergyCorrelator and Nsubjettiness FASTJET CONTRIBS [84, 85]. For N -subjettiness, we use one-pass WTA minimization with $\beta = 1$. As a concrete example of a groomer, we

¹³WTA axes align with a hard prong within the jet. They are nice theoretically, as they avoid recoil due to soft emissions [74, 87–90]. For low p_T tops, however, the use of WTA axes can potentially lead to lopsided axes. We explicitly checked that our results are unmodified if standard E -scheme recombination is used instead.

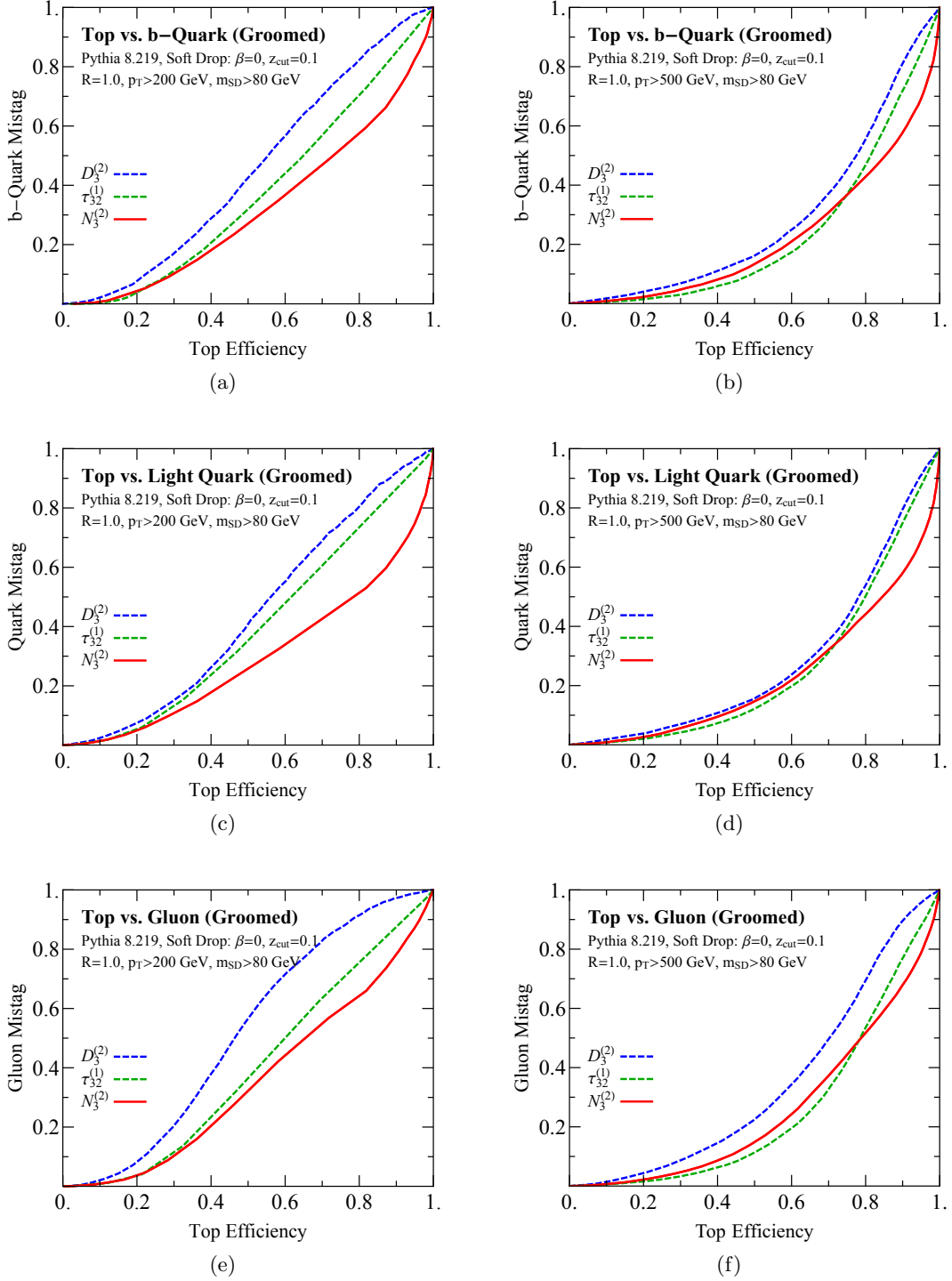


Figure 9: ROC curves comparing the groomed observables N_3 , $\tau_{3,2}$, and D_3 for (left column) $p_{T,J} = 200$ GeV and (right column) $p_{T,J} = 500$ GeV. The discrimination is shown for boosted top quarks against (top row) b -jets, (middle row) light quark jets, and (bottom row) gluon jets. In all cases, soft drop grooming has been applied, and the selection efficiency is after a groomed jet mass cut of $m_{\text{SD}} > 80$ GeV. The N_3 observable offers improved discrimination power, particularly at high signal efficiencies.

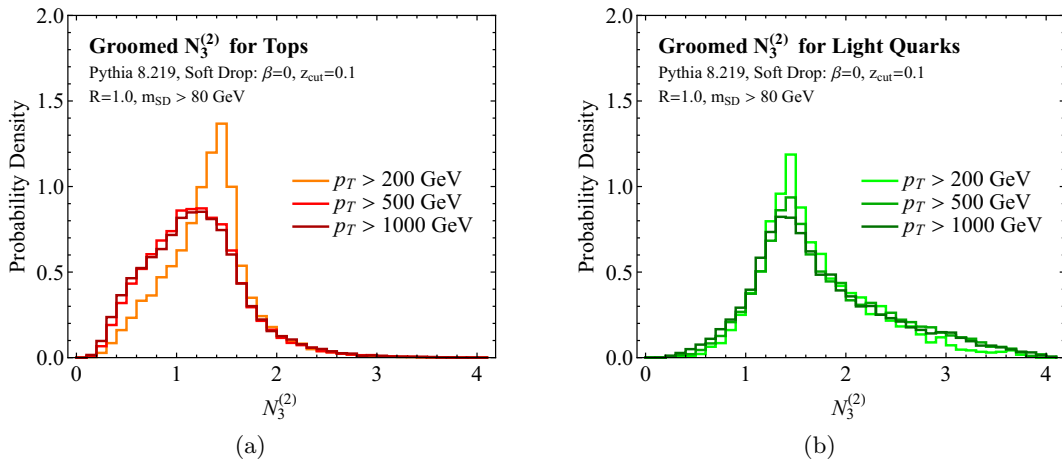


Figure 10: Stability of the groomed N_3 observable as a function of p_{TJ} for (a) signal and (b) background distributions. Here, light quark jets are used as representative of the background; gluons and b -jets behave similarly. The shift in the signal distribution in the lowest p_{TJ} bin is due to a high fraction of top quarks whose decay products are not fully captured by the $R = 1.0$ jet radius.

use $\beta = 0$ soft drop [86] (a.k.a. modified mass drop with $\mu = 1$ [41, 42]) with $z_{\text{cut}} = 0.1$, though our general observations should be independent of the particular choice of groomer.

As discussed in Sec. 4.1, we focus on the behavior of the observables on groomed jets, where N_3 was designed to perform well and where N_3 behaves parametrically like $\tau_{3,2}$. In App. B.2, we study boosted top tagging without grooming, where N_3 is still a reasonably powerful discriminant on ungroomed jets, but not as strong as $\tau_{3,2}$. We also discuss the behavior of M_3 in App. B.1, using power-counting arguments to show why it is a poor discriminant with standard groomers, but might perform better with a more aggressive grooming strategy.

In Fig. 8, we show distributions for groomed N_3 , comparing the top jet signal to the backgrounds of b -quark, light quark, and gluon jets. A groomed mass cut of $m_{\text{SD}} > 80$ GeV is applied, following a recent ATLAS study [160]. Here, we use $\beta = 2$ as the angular exponent for N_3 ; power counting does not, in this case, predict a preferred value of β , so it could be optimized for experimental performance. The behavior of these distributions is quite interesting, particularly for $p_{TJ} > 500$ GeV in Fig. 8b, where the top quarks are truly boosted. The signal distribution drops off sharply above $N_3 \simeq 1.5$, while the background distribution extends to larger values for all three samples. This behavior leads to excellent performance at high signal efficiencies, and is quite different than for $\tau_{3,2}$ (see Fig. 24 in App. B.2). Note that these distributions are calculated after the soft drop mass cut, so the region where N_3 exhibits improved performance is the one directly relevant for LHC searches.

In Fig. 9, we show signal efficiency versus background rejection (ROC) curves for

boosted top discrimination against b -quark, light quark, and gluon jets. In these and all subsequent ROC curves, the efficiency and mistag rates are given *after* applying a baseline mass requirement, in order to show just the gain in performance from adding a substructure cut. The baseline efficiencies for the $m_{\text{SD}} > 80$ GeV mass selection are

$$p_{TJ} = 200 \text{ GeV} : \quad \mathcal{E}_t = 61\%, \quad \mathcal{E}_b = 2.4\%, \quad \mathcal{E}_q = 2.8\%, \quad \mathcal{E}_g = 6.6\%, \quad (4.11)$$

$$p_{TJ} = 500 \text{ GeV} : \quad \mathcal{E}_t = 87\%, \quad \mathcal{E}_b = 10\%, \quad \mathcal{E}_q = 10\%, \quad \mathcal{E}_g = 19\%, \quad (4.12)$$

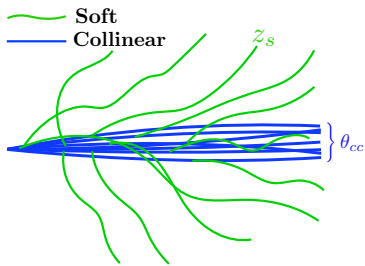
and the final efficiencies and mistag rates are obtained by multiplying these baseline values by those shown in Fig. 9. Comparing $p_{TJ} = 200$ GeV and $p_{TJ} = 500$ GeV, we conclude that the behavior of N_3 is reasonably robust as a function of p_{TJ} (see Fig. 10 for higher p_{TJ} values). The simplified version of D_3 with this choice of angular exponent gives rather poor discrimination power, especially for gluon jets; the apparent negative discrimination power for certain ROC curves in Fig. 9 is due to the use of a (non-optimal) one-sided cut. It is also satisfying to see the behavior predicted from the power-counting analysis. At lower top efficiencies, where there are well-resolved jets, N_3 and $\tau_{3,2}$ exhibit similar discrimination power, but at higher efficiencies, where there are not well-resolved jets, the structure of N_3 leads to considerably improved performance. It would be interesting to see whether these parton shower predictions remain true in LHC data.

Finally, another important feature of the soft-dropped N_3 observable is its stability as the mass and p_T of the jet are varied. This has recently been emphasized in Ref. [79] as a highly desirable feature of jet substructure observables, as it removes mass sculpting. In Fig. 10, we show the signal and background distributions for three different values of the jet p_{TJ} , namely $p_{TJ} = \{200, 500, 1000\}$ GeV following Ref. [160]. Remarkable stability of the N_3 distribution is seen, with the main distortion appearing for the top sample in the lowest p_{TJ} bin, where the $R = 1.0$ jet radius is not always large enough to capture all of the top decay products. Between $p_{TJ} = 500$ GeV and 1000 GeV, there are almost no changes to either the signal or background distributions. Though not shown here, $\tau_{3,2}$ exhibits comparable stability to N_3 , as expected since they share the same power counting. We conclude that soft-dropped N_3 is a powerful boosted top tagger that exhibits many experimentally desirable features.

5 New Observables for 2-prong Substructure

Jet substructure techniques have played an increasingly important role in recent LHC searches, especially for new resonances with decays involving boosted $W/Z/H$ bosons [21–28, 161–165]. In order to understand any possible hint of new physics in diboson analyses, it is essential to have exceptional control over the behavior of jet substructure discriminants, to allay concerns about possible analysis artifacts [166, 167]. In our view, echoing the perspective of Ref. [79], properties like stability with jet p_T and resilience to mass sculpting are just as important as (and perhaps more so than) absolute tagging performance.

In this section, we use the generalized correlators to construct 2-prong taggers that are robust and perform well. This is an application where the original energy correlators have



Modes	$e_2^{(\beta)}$	$1e_3^{(\beta)}$	$2e_3^{(\beta)}$	$3e_3^{(\beta)}$
<i>CCC</i>	θ_{cc}^β	θ_{cc}^β	$\theta_{cc}^{2\beta}$	$\theta_{cc}^{3\beta}$
<i>CCS</i>	$z_s + \theta_{cc}^\beta$	$z_s \theta_{cc}^\beta$	$z_s \theta_{cc}^\beta$	$z_s \theta_{cc}^\beta$
<i>CSS</i>	z_s	z_s^2	z_s^2	z_s^2
<i>SSS</i>	z_s^2	z_s^3	z_s^3	z_s^3

Table 3: Parametric contributions to e_2 and the 3-point correlators, ${}_v e_3$, in the case of a jet with 1-prong substructure. The different contributions arise from correlations among soft (*S*) and collinear (*C*) radiation.

already proven useful through the C_2 and D_2 ratios [65, 74]. Here, we propose three new ratios:

$$M_2^{(\beta)} = \frac{1e_3^{(\beta)}}{1e_2^{(\beta)}}, \quad N_2^{(\beta)} = \frac{2e_3^{(\beta)}}{(1e_2^{(\beta)})^2}, \quad D_2^{(\alpha,\beta)} = \frac{3e_3^{(\alpha)}}{(1e_2^{(\beta)})^{3\alpha/\beta}}, \quad (5.1)$$

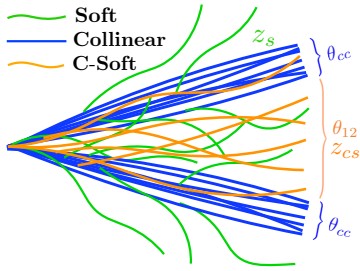
corresponding to the three variants of the 3-point correlator in Eq. (3.5). Each of these observables is sensitive to different angular structures within the jet and therefore achieves its discrimination power in a different manner. This fact is highlighted in their different behavior under grooming, where M_2 and $D_2^{(1,2)}$ were constructed to only perform well on groomed jets. Therefore, these observables are probes not only of 2-prong jet substructure but also of any grooming procedure applied to the jet.¹⁴

5.1 Power-Counting Analysis and Observable Phase Space

The power counting for 2-prong discriminants follows straightforwardly from Sec. 2.3, using the modes summarized in Fig. 3 and Table 1. Since the phase space is much simpler than in the 3-prong case, we can study the behavior of M_2 , N_2 , and $D_2^{(\alpha,\beta)}$ both before and after jet grooming.

To begin, we consider the 1-prong background in Table 3 and power count the contributions to e_2 and ${}_v e_3$ from every possible triplet of soft and collinear modes. We do the same for the 2-prong signal in Table 4, where we also have to consider collinear-soft modes, though we do not show the power-suppressed triplets for brevity. These tables show that while the 3-point correlators have similar behavior for soft particles, they have different behavior for correlations among collinear particles (cf. the first row of Table 3 and the second and third row of Table 4). This is expected given the different number of pairwise angles in the definition of each ${}_v e_3$. We discuss the consequences of this power counting for each of the proposed ratios in the following subsections.

¹⁴See also Ref. [168] for an example of an observable designed specifically to probe the grooming procedure by measuring non-global correlations, and Ref. [44] for an example of improving discrimination power by understanding the behavior of the grooming procedure.



Modes	$e_2^{(\beta)}$	$1e_3^{(\beta)}$	$2e_3^{(\beta)}$	$3e_3^{(\beta)}$
$C_1 C_2 S$	θ_{12}^β	$z_s \theta_{12}^\beta$	$z_s \theta_{12}^\beta$	$z_s \theta_{12}^\beta$
$C_1 C_2 C$	θ_{12}^β	θ_{cc}^β	$\theta_{12}^\beta \theta_{cc}^\beta$	$\theta_{12}^{2\beta} \theta_{cc}^\beta$
$C_1 C_2 C_s$	θ_{12}^β	$z_{cs} \theta_{12}^\beta$	$z_{cs} \theta_{12}^{2\beta}$	$z_{cs} \theta_{12}^{3\beta}$

Table 4: Same as Fig. 3, but for a jet with a resolved 2-prong substructure. The different contributions arise from correlations among soft (S), collinear (C_i), and collinear-soft (C_s) radiation. Power-suppressed contributions are not shown.

5.1.1 M_2

The observable M_2 is based on $1e_3$:

$$M_2^{(\beta)} = \frac{1e_3^{(\beta)}}{1e_2^{(\beta)}}. \quad (5.2)$$

We first consider its behavior on 1- and 2-prong jets without grooming. For 1-prong background jets from Table 3, we have

$$\begin{aligned} \text{1-prong background (ungroomed): } e_2^{(\beta)} &\sim z_s + \theta_{cc}^\beta, \\ 1e_3^{(\beta)} &\sim z_s^2 + \theta_{cc}^\beta. \end{aligned} \quad (5.3)$$

This exhibits a non-trivial phase space with boundaries $1e_3 \sim (e_2)^2$ when the jet is dominated by soft radiation, and $1e_3 \sim e_2$ when the jet is dominated by collinear radiation. For 2-prong signal jets from Table 4, we have

$$\begin{aligned} \text{2-prong signal (ungroomed): } e_2^{(\beta)} &\sim \theta_{12}^\beta, \\ 1e_3^{(\beta)} &\sim z_{cs} \theta_{12}^\beta + \theta_{cc}^\beta. \end{aligned} \quad (5.4)$$

From the fact that $z_{cs} \ll 1$, and $\theta_{cc} \ll \theta_{12}$, one therefore finds the inequality $1e_3 \ll e_2$.

The phase space for M_2 is shown in Fig. 11a. This power-counting analysis demonstrates that before any grooming has been applied, there is considerable overlap between the parametric phase space regions occupied by 1- and 2-prong jets. Therefore, M_2 has limited discrimination power on ungroomed jets. The power-counting analysis also makes clear why M_2 performs so poorly: 1-prong jets are dominated by soft radiation with scaling $1e_3 \sim (e_2)^2$, which overlaps with the 2-prong signal region with $1e_3 \ll e_2$. The fact that this overlap is caused only by soft radiation also suggests that it can be eliminated by applying a jet grooming procedure to remove soft radiation.

In Fig. 11b, we show the phase space for M_2 after grooming. Soft drop removes the z_s contributions from Eq. (5.3), which pushes 1-prong background jets to the upper boundary of the phase space with $1e_3 \sim e_2$. By contrast, the parametric scaling of the signal jets is

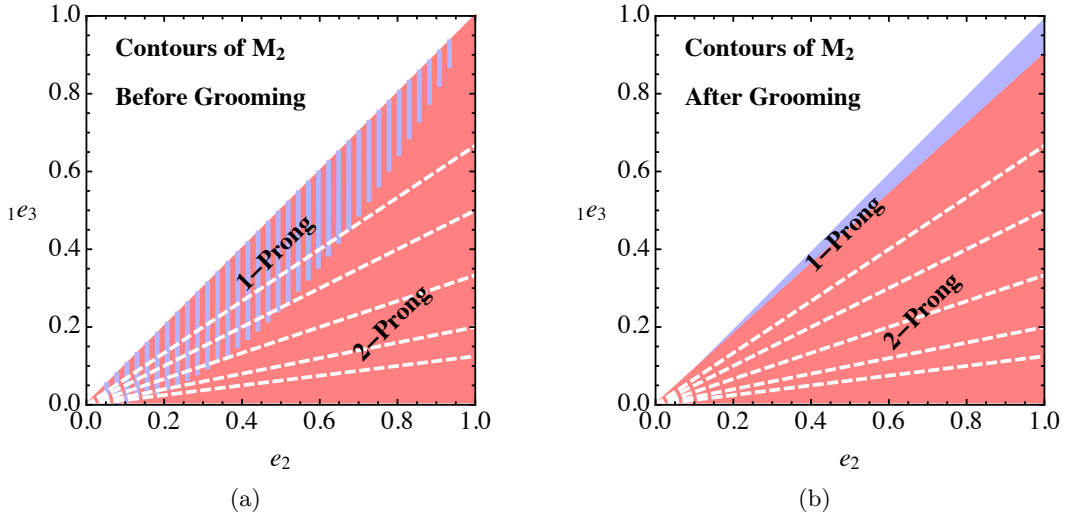


Figure 11: Parametric phase space for the M_2 observable (a) before grooming and (b) after grooming. The grooming procedure removes wide-angle soft radiation, pushing 1-prong jets to the upper boundary of the phase space.

unaffected by the soft drop procedure.¹⁵ This yields a triangular phase space that resembles the case of $\tau_{2,1}$ in Fig. 1b, where 1-prong background jets live on the upper boundary and 2-prong signal jets live in the bulk. Perhaps counterintuitively, the soft drop procedure pushes the background to larger values of M_2 , achieving better discrimination power.

The M_2 observable therefore provides an interesting example of a discriminant that only performs well after grooming. It emphasizes the parametric effect that grooming procedures can have on radiation within a jet, beyond simply removing jet contamination. For this reason, we expect precision calculations of the M_2 distribution to provide useful insights into the behavior of such grooming procedures.

5.1.2 N_2

The observable N_2 is based on ${}_2e_3$,

$$N_2^{(\beta)} = \frac{2e_3^{(\beta)}}{({}_1e_2^{(\beta)})^2}. \quad (5.5)$$

The power-counting argument for N_2 closely parallels M_2 . We will see that the phase space for N_2 is parametrically unmodified by the grooming procedure, making it perform well on both groomed and ungroomed jets.

¹⁵As stated at the end of Sec. 2.3, for simplicity we do not power count the grooming parameter z_{cut} . It is well understood how to properly incorporate z_{cut} into the power-counting analysis (see e.g. [60, 61]), but this has a negligible impact for understanding the qualitative behavior of 2-prong discriminants.

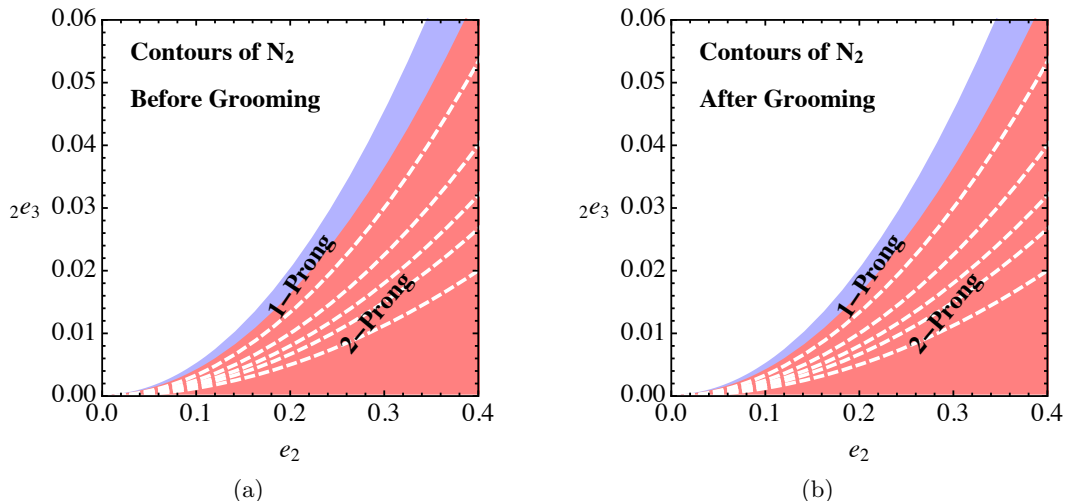


Figure 12: Same as Fig. 11 but for N_2 . The grooming procedure does not modify the scaling of the phase space, so (a) and (b) are identical as far as power counting is concerned. Therefore, the N_2 observable exhibits good discrimination power both before and after grooming is applied.

We again begin by analyzing the parametric behavior of the observable on ungroomed jets. Using Table 3 for 1-prong background jets, we find

$$\begin{aligned}
 \text{1-prong background (ungroomed): } \quad e_2^{(\beta)} &\sim z_s + \theta_{cc}^\beta, \\
 2e_3^{(\beta)} &\sim z_s^2 + z_s\theta_{cc}^\beta + \theta_{cc}^{2\beta}.
 \end{aligned} \tag{5.6}$$

In contrast to M_2 , the 1-prong background jets exhibit only a single scaling, $2e_3 \sim (e_2)^2$, for jets dominated by either soft or collinear radiation. Using Table 4 for 2-prong signal jets, we find

$$\begin{aligned}
 \text{2-prong signal (ungroomed): } \quad e_2^{(\beta)} &\sim \theta_{12}^\beta, \\
 2e_3^{(\beta)} &\sim z_s\theta_{12}^\beta + z_{cs}\theta_{12}^{2\beta} + \theta_{cc}^\beta\theta_{12}^\beta.
 \end{aligned} \tag{5.7}$$

Signal jets satisfy the inequality $2e_3 \ll (e_2)^2$, explaining the definition of the N_2 observable. The phase space before grooming is summarized in Fig. 12a, where there is clear separation between 1-prong background jets, which live on the upper boundary of the phase space, and 2-prong signal jets, which live in the bulk of the phase space, again resembling the case of $\tau_{2,1}$ in Fig. 1b.

Because the 1-prong background jets have a single scaling, removing z_s from Eq. (5.6) has no effect on the parametric phase space. Similarly, removing z_s from Eq. (5.7) does not change the parametrics of the 2-prong signal. Therefore, N_2 behaves more similarly to other 2-prong discriminants in the literature, since its discrimination power does not come entirely from the grooming procedure. The power-counting analysis also suggests that N_2

should be a powerful 2-prong discriminant both before and after grooming is applied; this will be verified in the parton shower studies below.

It is also interesting to contrast the N_2 phase space in Fig. 12a with that of D_2 in Fig. 1a. For D_2 , the background jets are bounded by two different scaling behaviors:

$$(e_2^{(\beta)})^3 < e_3^{(\beta)} < (e_2^{(\beta)})^2. \quad (5.8)$$

For N_2 , by contrast, the background jets exhibit a single scaling and therefore live entirely on the boundary of phase space:

$${}_2e_3^{(\beta)} \sim (e_2^{(\beta)})^2. \quad (5.9)$$

Since this boundary is purely geometric, the N_2 distributions are remarkably insensitive to the mass or p_T of the jet, even before grooming is applied.

Just as N_3 is related to $\tau_{3,2}$ (see Sec. 4.1), N_2 behaves parametrically like $\tau_{2,1}$ in the resolved limit. The power-counting analysis proceeds identically as for N_3 and will not be repeated here; see App. C for the general argument relating N_i to $\tau_{i,i-1}$. We want to emphasize again that, in analogy to Fig. 7, N_2 exhibits $\tau_{2,1}$ -like behavior without reference to any axes within the jet. It therefore does not exhibit the axes pathologies that arise for N -subjettiness in the limit of unresolved substructure, and N_2 can therefore be expected to have improved performance compared to $\tau_{2,1}$, particularly at high efficiencies.

5.1.3 $D_2^{(1,2)}$

Our final example of a 2-prong discriminant is based on ${}_3e_3 = e_3$, where we reconsider the D_2 observable with two distinct angular exponents,

$$D_2^{(\alpha,\beta)} \equiv \frac{e_3^{(\alpha)}}{(e_2^{(\beta)})^{3\alpha/\beta}}. \quad (5.10)$$

The case of $\alpha = \beta$ was first defined in Ref. [65] and analytically calculated in Ref. [58]. While the phase space for $D_2^{(\alpha,\beta)}$ was discussed in detail in Ref. [58], we focus on the impact that $\alpha \neq \beta$ has on groomed jet discrimination.

With distinct angular exponents α and β , 1-prong background jets exhibit the scaling

$$\begin{aligned} \text{1-prong background (ungroomed): } \quad e_2^{(\beta)} &\sim z_s + \theta_{cc}^\beta, \\ e_3^{(\alpha)} &\sim z_s^2 + z_s \theta_{cc}^\alpha + \theta_{cc}^{3\alpha}. \end{aligned} \quad (5.11)$$

The background therefore occupies a non-trivial phase space with boundaries $e_3^{(\alpha)} \sim (e_2^{(\beta)})^2$, when the jet is dominated by soft radiation, and $e_3^{(\alpha)} \sim (e_2^{(\beta)})^{3\alpha/\beta}$, when the jet is dominated by collinear radiation. The 2-prong signal has the parametric scaling

$$\begin{aligned} \text{2-prong signal (ungroomed): } \quad e_2^{(\beta)} &\sim \theta_{12}^\beta, \\ e_3^{(\alpha)} &\sim z_s \theta_{12}^\alpha + z_{cs} \theta_{12}^{3\alpha} + \theta_{12}^{2\alpha} \theta_{cc}^\alpha, \end{aligned} \quad (5.12)$$

from which one can derive the relation $e_3^{(\alpha)} \ll (e_2^{(\beta)})^{3\alpha/\beta}$. This demonstrates that the definition of $D_2^{(\alpha,\beta)}$ in Eq. (5.10) is indeed appropriate for 2-prong substructure, confirming the expectation from boost invariance (see Eq. (3.8)).

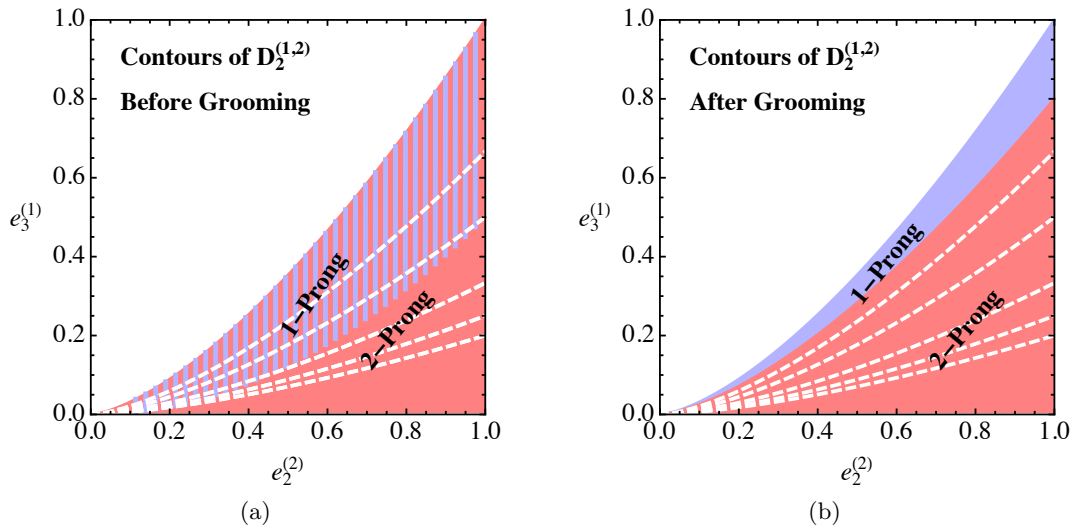


Figure 13: Same as Fig. 11 but for $D_2^{(1,2)}$. Only after grooming is applied can the 1- and 2-prong regions of phase space be separated.

As discussed in Ref. [58] for ungroomed jets, the observable $D_2^{(\alpha,\beta)}$ only provides good discrimination between 1-prong and 2-prong jets for

$$3\alpha > 2\beta. \quad (5.13)$$

When this relation is violated, the phase space regions for signal and background jets overlap. This is shown in Fig. 13a, where contours of $D_2^{(\alpha,\beta)}$ cannot separate the 1- and 2-prong regions when Eq. (5.13) is violated. After a grooming procedure is applied, though, the overlapping phase space region is removed, as shown schematically in Fig. 13b. Now the constraint in Eq. (5.13) no longer applies, and the angular exponents can be chosen with a particular focus on discrimination power on groomed jets.

The choice of (α, β) exponents could be tuned to optimize performance, but we advocate that $\alpha = 1, \beta = 2$ is a natural choice for groomed 2-prong discrimination. This choice explicitly violates Eq. (5.13), so $D_2^{(1,2)}$ can only have good performance after grooming. The choice of $\beta = 2$ is motivated by the relation

$$e_2^{(2)} \simeq \frac{p_{TJ}^2}{m_J^2}, \quad (5.14)$$

such that a cut on the jet mass, or p_T , is effectively a cut on $e_2^{(2)}$. Without grooming, one would typically take $\alpha = 2$, but with grooming, one can lower the angular exponent α to 1 to more directly probe collinear emissions. Importantly, by considering the observable with separate α and β exponents, we are able to satisfy both the requirement that it behaves sensibly under a mass cut, as well as improve its sensitivity to collinear emissions. This is not possible with the $\alpha = \beta$ version of the D_2 observable, and indeed, $D_2^{(1,2)}$ leads to improved discrimination power on groomed jets. From an analytic perspective, the choice

of $\alpha = 1$, $\beta = 2$ simplifies calculations, hopefully facilitating precision calculations of $D_2^{(1,2)}$ on groomed jets at the LHC.

5.2 Performance in Parton Showers

We now perform a parton shower study to verify the predictions of the above power-counting analysis. It is useful to briefly summarize our robust predictions regarding the behavior of M_2 , N_2 , and $D_2^{(1,2)}$ as boosted 2-prong taggers:

- The M_2 observable should provide little discrimination power before grooming, but will act as a powerful discriminant after the removal of wide-angle soft radiation.
- The N_2 observable will act as a powerful discriminant both before and after grooming, matching the behavior of $\tau_{2,1}$ in the resolved limit.
- The $D_2^{(1,2)}$ observable will behave similarly to M_2 , providing good discrimination power only after grooming has been applied.

These predictions rely only on parametric scalings and are therefore independent of the implementation details of the perturbative parton shower or the hadronization model. For conciseness, we only show results generated with PYTHIA 8.219, though we used VINCIA 2.0.01 [169–175] to check that the same results could be obtained with an alternative perturbative shower. We have not yet studied hadronization uncertainties, but we expect them to be small, particularly for groomed jets.

To verify these power-counting predictions, we use the same analysis and generation strategy as Sec. 4.2, again using a jet radius of $R = 1.0$. We generate background QCD jets from $pp \rightarrow Zj$ events, where we consider separately the cases of $j = g$ (gluon) and $j = u, d, s$ (light quark), letting the Z decay leptonically to avoid additional hadronic activity. The 2-prong signal of boosted Z bosons are generated from $pp \rightarrow ZZ$ events, with one Z decaying leptonically, and the other to light quarks, $q = u, d, s$. We do not address in this paper the issue of sample dependence and the impact of color connections to the rest of the event. While it would be interesting to compare the discrimination power of N_2 against the more-prevalent $pp \rightarrow jj$ background, we expect the conclusions from $pp \rightarrow Zj$ to be robust, especially after grooming has been applied.

For concreteness, we always set the angular exponent in the energy correlator to $\beta = 2$, such that a mass cut directly corresponds to a cut on the denominator of the observable, see Eq. (5.14). While this is a nice theoretical feature, it is by no means necessary, and the value of β could be optimized for experimental performance. To focus on the phase space where tagging performance actually matters, we place a cut of $m \in [80, 100]$ GeV for all of the ungroomed distributions and a cut of $m_{\text{SD}} \in [80, 100]$ GeV for all of the groomed distributions. We only present distributions with a cut of $p_T > 500$ GeV, though other p_T ranges exhibit similar behaviors.

In Fig. 14, we show normalized distributions of M_2 , N_2 , and $D_2^{(1,2)}$ before and after soft drop grooming. Despite all being derived from 3-point correlators, they exhibit rather different behaviors. As expected, M_2 is a poor discriminant before grooming is applied;

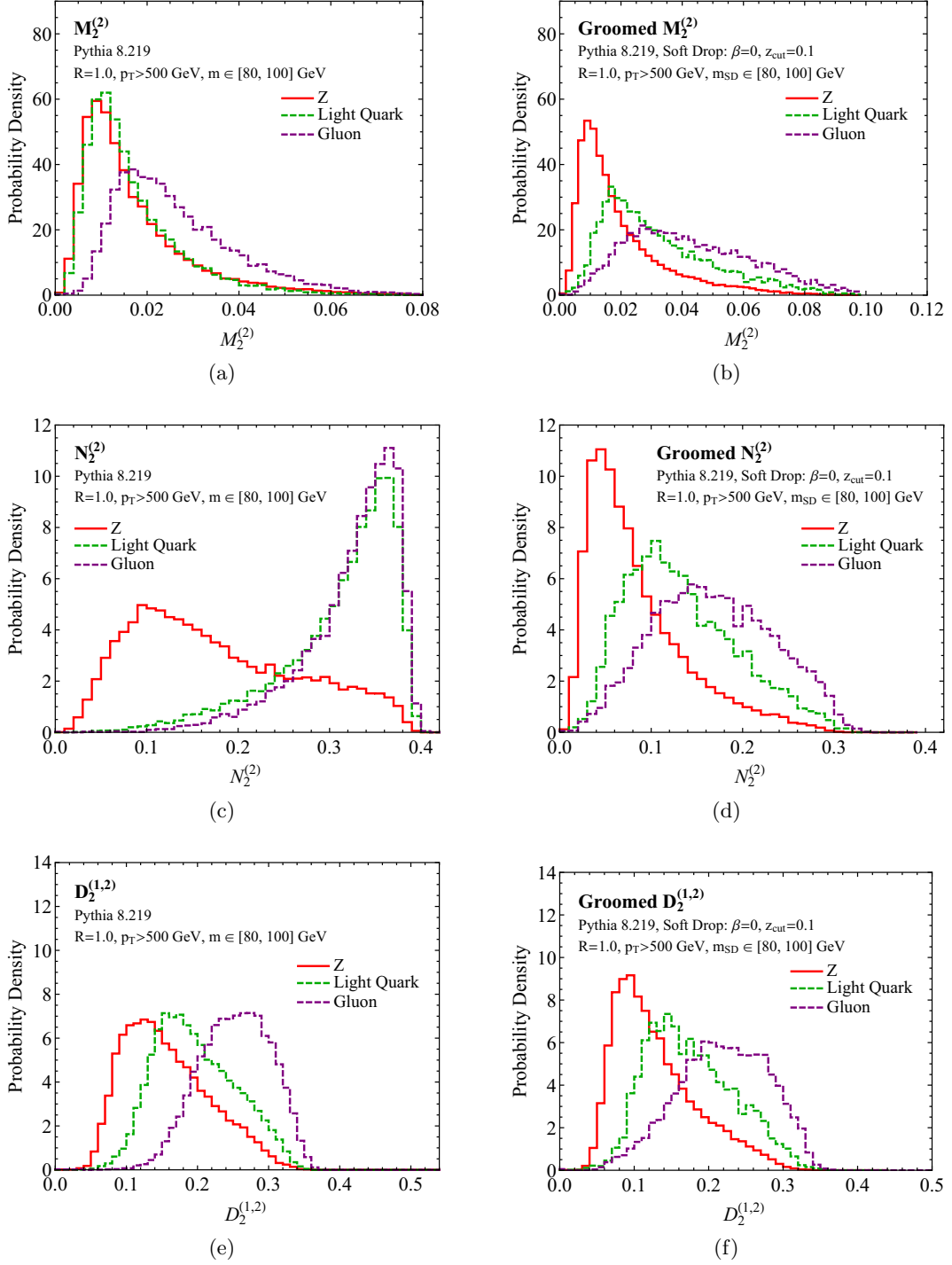


Figure 14: Distributions for (top row) M_2 , (middle row) N_2 , and (bottom row) $D_2^{(1,2)}$ measured on boosted Z and quark/gluon jets. The results are shown (left column) before grooming and (right column) after grooming.

amusingly, the distributions of the Z boson signal and quark jet background are essentially identical. As predicted by the power-counting analysis, the soft drop grooming procedure pushes the background M_2 distributions to larger values while leaving the signal distribution largely unmodified. We are not aware of another substructure discriminant with such a dramatic shift in behavior after jet grooming.

Turning to N_2 , it exhibits good discrimination power both before and after grooming is applied, even though the shapes of the distributions are substantially modified by grooming. Before grooming, the N_2 distribution exhibits a sharp edge at its upper boundary. This arises because 1-prong background jets have a single parametric scaling and are therefore compressed along the upper boundary of the phase space (see Fig. 12). After grooming, N_2 remains a powerful discriminant, as the phase space is parametrically unchanged by the grooming procedure. As expected, the peak values of the distributions decrease as soft radiation is groomed away, but the range spanned by the distribution remains approximately constant. This highlights the fact that parametric arguments give robust predictions about the boundaries of phase space but not the specific shapes of the distributions. In App. C, we also verify that N_2 and $\tau_{2,1}$ exhibit the same parametric behaviors in the resolved limit.

Finally, the $D_2^{(1,2)}$ observable, while only a fair discriminant before grooming, exhibits good discrimination power after soft drop is applied. Therefore, we have seen that all of the power-counting predictions are observed in the parton shower generators, suggesting that parametric scalings dominate the behavior of these observables, at least for the purposes of 2-prong substructure tagging. From Fig. 14, we see that some of the observables behave quite differently for the quark and gluon samples. We revisit the possibilities of using ${}_{\nu}e_3$ for quark/gluon discrimination in Sec. 6, where we introduce the U_2 observable, which is based on ${}_{1}e_3$, similar to M_2 .

To study the discrimination power more quantitatively, we show ROC curves before and after grooming in Fig. 15, considering the quark and gluon backgrounds separately. The baseline efficiencies for the ungroomed and groomed mass selections are

$$\begin{aligned} m \in [80, 100] \text{ GeV} : \quad & \mathcal{E}_Z = 27\%, \quad \mathcal{E}_q = 17\%, \quad \mathcal{E}_g = 15\%, \\ m_{\text{SD}} \in [80, 100] \text{ GeV} : \quad & \mathcal{E}_Z = 37\%, \quad \mathcal{E}_q = 2.6\%, \quad \mathcal{E}_g = 4.3\%, \end{aligned} \quad (5.15)$$

where we again normalize the ROC curves to show only the gains from the new 2-prong discriminants.¹⁶ We use D_2 (with $\beta = 2$) as a standard reference, since it is currently used by the ATLAS experiment for its excellent tagging performance [5, 6, 9, 24, 26–28, 161, 162, 176, 177].¹⁷

Of the three new observables, only N_2 is designed to act as a discriminant on ungroomed jets. In both Figs. 15a and 15c, we see that N_2 outperforms the standard D_2 observable in discriminating against both quark and gluon jets. From power-counting arguments, we cannot predict the relative performance between the quark and gluon samples,

¹⁶Note the improved signal significance in the groomed case, which offsets the apparent decrease in discrimination performance when comparing the ungroomed and groomed ROC curves.

¹⁷Note that ATLAS uses D_2 after jet trimming [78], which has a similar parametric behavior to D_2 after soft drop in the region we are considering.

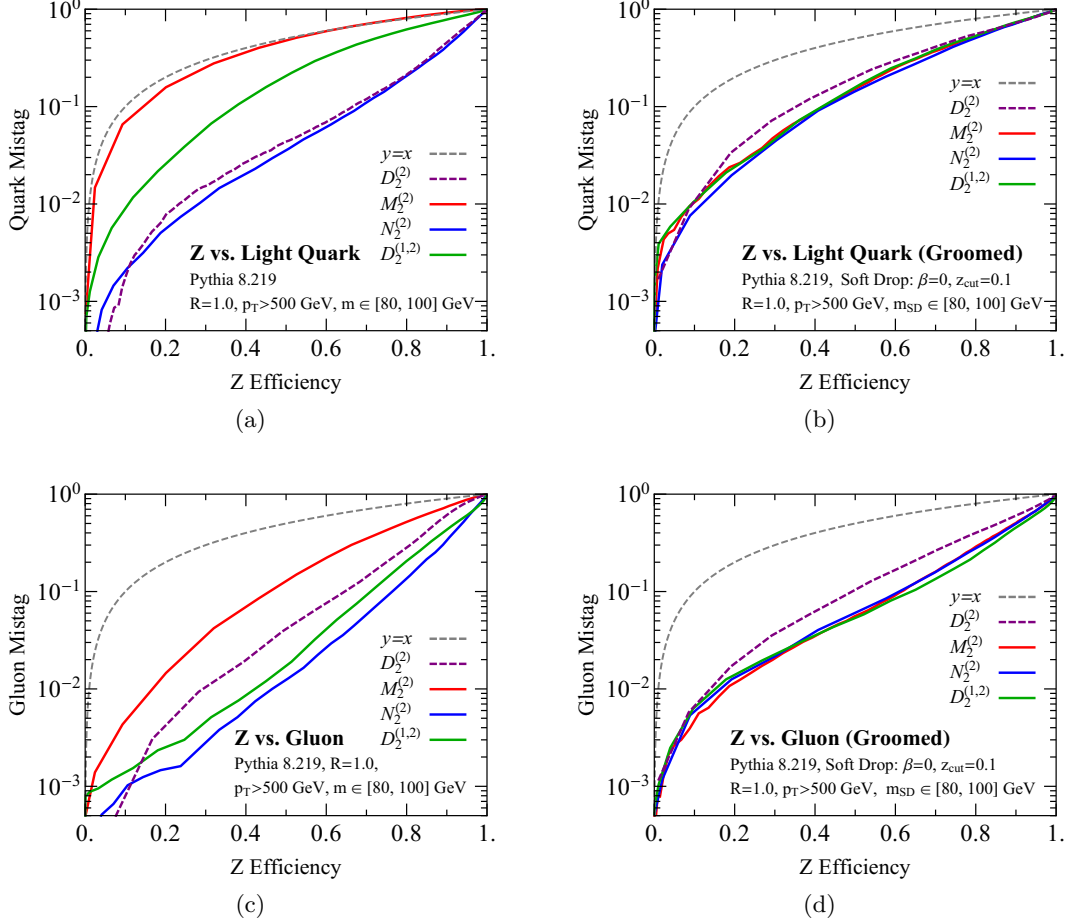


Figure 15: ROC curves for boosted Z boson (left column) before grooming and (right column) after grooming. The discrimination power is shown against (top row) quark jets and (bottom row) gluon jets. As a point of reference, we show the ROC curve for $D_2^{(2)}$, which is currently used by the ATLAS experiment, in dashed purple. As predicted by power counting, the application of grooming greatly modifies the relative performance of the different observables. Note that an ungroomed mass cut is applied in the left column, while a groomed mass cut is applied in the right column. Efficiencies from these mass cuts are given in Eq. (5.15). See Fig. 27 in App. C for a comparison to $\tau_{2,1}$, and see Fig. 28 in App. D for a hybrid strategy using a groomed mass cut but ungroomed discriminants.

but the fact that N_2 sees significant performance gains on the gluon sample is very encouraging. As discussed in Sec. 5.1, the discrimination power of N_2 is closely related to $\tau_{2,1}$ in the resolved limit, but with an improved behavior in the transition to the unresolved region. We discuss this relation in more detail in App. C, showing that N_2 has slightly improved performance compared to $\tau_{2,1}$ on ungroomed jets, but considerably improved performance after grooming.

After jet grooming, shown in Figs. 15b and 15d, all three new observables offer improved discrimination power over D_2 . Comparing the results before and after grooming, we see dramatic gains in performance for M_2 and $D_2^{(1,2)}$, as expected from power counting. It is rather curious that after grooming, all three observables offer comparable discrimination power, even though they are based on $v e_3$ correlators with different characteristic behaviors. It would be interesting to study the correlations between these observables to see if they are probing complementary physics effects. Such correlations go beyond the power-counting analysis of this paper, so we leave a study to future work.

Thus far, we have only considered observables measured entirely on either groomed or ungroomed jets. Experimentally, though, it may be desirable to measure ungroomed observables after the application of a groomed mass cut (see e.g. [178]); we refer to this as a “hybrid” strategy. In App. D, we present ROC curves for M_2 , N_2 , D_2 , and $\tau_{2,1}$ using this hybrid strategy and analyze their behavior using power counting. We leave a more detailed study of the optimal use of mixed groomed/ungroomed observables to future work.

5.3 Stability in Parton Showers

In addition to their absolute performance, our new 2-prong discriminants exhibit stable behavior, especially after grooming. As recently emphasized in Ref. [79], stability of background distributions as a function of mass and p_T cuts is an important consideration when designing jet substructure observables. Excessive dependence on jet mass and p_T can lead to mass sculpting, which can increase systematic uncertainties in sideband fits, counteracting gains from improved tagging performance.

To illustrate how the phase space structure controls the stability of the observable, it is interesting to study the stability of D_2 , M_2 , and N_2 before and after grooming. These three observables represent the three scaling behaviors we have encountered in this paper. Prior to grooming, we have:

- D_2 in Fig. 1a: The background occupies a non-trivial phase space region that does not overlap with the signal.
- M_2 in Fig. 11: The background occupies a non-trivial phase space region overlapping with the signal.
- N_2 in Fig. 12: The background is confined to a single scaling on the boundary of phase space.

The $D_2^{(1,2)}$ observable has a similar phase space structure to M_2 , and will therefore behave similarly, so we do not show it explicitly in this section. Note that $\tau_{2,1}$ has the same phase space structure as N_2 , so it exhibits related stability properties.

In Fig. 16, we use parton showers to test the stability of D_2 , M_2 , and N_2 on the light quark background as the jet mass cut is varied.¹⁸ Prior to grooming, only the N_2 observable exhibits any degree of stability on the background. After grooming, all three observables have a nicely stable peak position and shape, and the residual variation could be compensated using the decorrelation technique of Ref. [79]. We can now use a power-counting analysis to demonstrate how these behaviors are dictated by the form of the phase space. Although we focus on light quark jets in Fig. 16, similar stability properties are observed for gluon jets. This is also emphasized by the power-counting argument, which is insensitive to the quark or gluon nature of the jet.

We begin by considering the observables before grooming. For D_2 in Fig. 1a, the background region is defined by two different scalings, one of which defines the upper boundary of the phase space and one of which defines the scaling of the boundary between the signal and background, and therefore the scaling of the desired cut value for discrimination. The upper boundary of the phase space is defined by the scaling $e_3 \sim (e_2)^2$, leading to the maximum value

$$D_2^{\max} \sim \frac{e_3}{(e_2)^3} \sim \frac{(e_2)^2}{(e_2)^3} \sim \frac{1}{e_2}. \quad (5.16)$$

Simplifying to the case of $\beta = 2$, and using Eq. (5.14), we have

$$D_2^{(2),\max} \sim \frac{p_{TJ}^2}{m_J^2}, \quad (5.17)$$

which depends sensitively on m_J and p_{TJ} . This behavior can be clearly seen in Fig. 16a, where the D_2 distribution shifts dramatically with the jet mass cut, an undesirable feature for the purposes of sideband calibration.

For M_2 with a phase space given in Fig. 11, we see quite different behavior. In this case, the upper boundary of the phase space is defined by ${}_1e_3 \sim e_2$, and therefore M_2 has a maximum value

$$M_2^{\max} \sim \frac{{}_1e_3}{e_2} \sim \frac{e_2}{e_2} \sim \text{const}, \quad (5.18)$$

which is largely independent of the jet mass, p_T , and the angular exponent β . Stability of the maximal value (endpoint), though, is not sufficient to guarantee stability of the distribution. Indeed, the scaling of the lower boundary of the phase space for the background is ${}_1e_3 \sim (e_2)^2$, so we expect a sharp drop in the background, and therefore a peak in the distribution, around

$$M_2^{\text{peak}} \sim \frac{{}_1e_3}{e_2} \sim \frac{(e_2)^2}{e_2} \sim e_2. \quad (5.19)$$

Simplifying again to the case of $\beta = 2$, and using Eq. (5.14), we have

$$M_2^{(2),\text{peak}} \sim \frac{m_J^2}{p_{TJ}^2}, \quad (5.20)$$

¹⁸We could alternatively vary the cut on the jet p_T . From the power-counting analysis, all stability properties are determined by functions of the ratio m_J/p_{TJ} , and therefore it is straightforward to understand the p_{TJ} dependence from the m_J dependence.

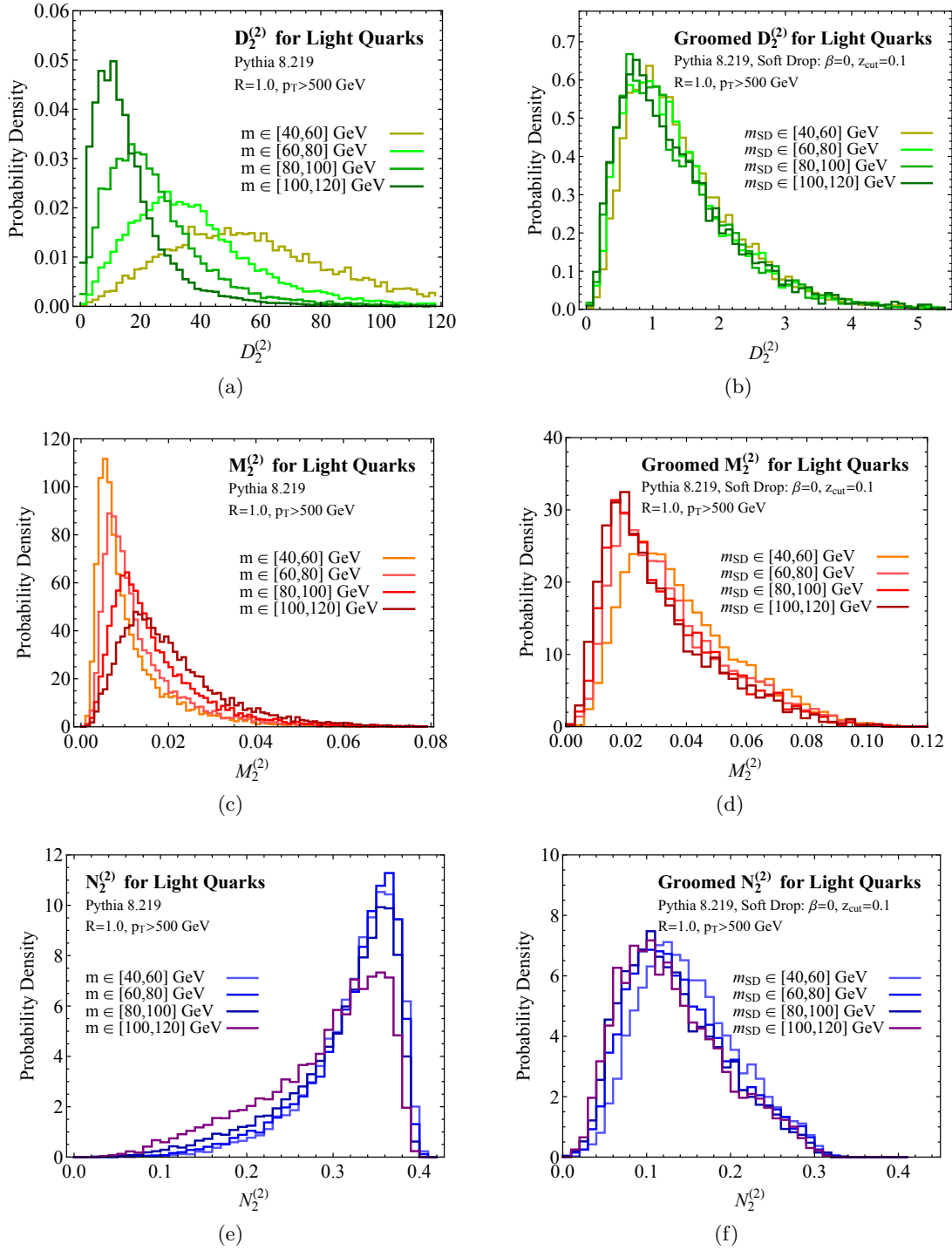


Figure 16: Stability of the light-quark background distributions for (top row) D_2 , (middle row) M_2 , and (bottom row) N_2 as a function of the jet mass cut, comparing (left column) un-groomed jets to (right column) groomed jets. The different structure of the phase space for N_2 leads to improved stability before grooming is applied. After grooming, all observables exhibit excellent stability. Similar results are found for gluon jets as well.

which depends sensitively on m_J and p_{TJ} , but in exactly the opposite way as D_2 . This behavior is observed in Fig. 16c.

Finally, for N_2 shown in Fig. 12, the background region is defined by a single scaling, namely $2e_3 \sim (e_2)^2$, which defines the upper boundary. Since there is a single scaling, we expect the peak for the background distribution to be defined by the same scaling. This means that N_2 has a maximum value and a peak location that both scale like

$$N_2^{\text{max,peak}} \sim \frac{2e_3}{(e_2)^2} \sim \frac{(e_2)^2}{(e_2)^2} \sim \text{const}, \quad (5.21)$$

which is largely independent of the jet mass, p_T , and the angular exponent β . This is well verified in the parton shower analysis, as shown in Fig. 16e. Thus, we see that by carefully engineering the phase space of an observable, one can achieve properties, such as stability, that are important experimentally. In this specific case, the stability of the full N_2 distribution gives further evidence that N_2 is a promising 2-prong tagger, even without grooming.

After grooming away soft radiation, we see from Figs. 16b, 16d, and 16f that all the distributions are stable, and from our power counting analysis, it is easy to understand why this is true. For D_2 , grooming has a dramatic impact (note the change in the x -axis range), since it removes the region of phase space that leads to the undesired scaling behavior in Eq. (5.17) (see also Fig. 2a). In this way, the endpoint for groomed D_2 (as well as the whole distribution) becomes remarkably robust to the jet mass cut. For the M_2 observable, the grooming removes the background in the bulk of phase space and pushes it to the upper boundary, as shown in Fig. 11, stabilizing the peak of the M_2 distribution but leaving the endpoint largely unchanged. After jet grooming, the parametric phase space for N_2 is unmodified, so the endpoint and peak scaling in Eq. (5.21) should not change. Comparing Figs. 16e and 16f, we see that the specific value of the N_2 endpoint and peak is modified, but the stability with varying mass cut is robust.

Therefore, in all cases after grooming, we have

$$\text{groomed : } D_2^{\text{max,peak}} \sim \text{const}, \quad M_2^{\text{max, peak}} \sim \text{const}, \quad N_2^{\text{max,peak}} \sim \text{const}. \quad (5.22)$$

This demonstrates three distinct ways of generating a stable distribution: engineering the background phase space to directly have the desired boundary (e.g. N_2), or grooming soft radiation to stabilize the boundary (e.g. D_2) or the peak (e.g. M_2) of the background distribution. It is important to emphasize that the power-counting analysis can only identify the power-law scaling of the distribution in m_J or p_{TJ} . Removing this power-law scaling does not, however, guarantee complete numerical stability of the distribution. For this, techniques such as designing decorrelated taggers (DDT) [79] can be used. We expect that methods like DDT will be most powerful when applied to variables that are already naturally stable, but we leave a study to future work.

6 Improving Quark/Gluon Discrimination

A major challenge in the field of jet substructure is reliable quark/gluon discrimination. Despite its many potential applications, there has been significant difficulty both in under-

standing the behavior of quark/gluon discriminants in parton showers, as well as in developing analytically-tractable observables which surpass the Casimir scaling limit (see Eq. (6.1) below). For detailed discussions of these issues, we refer the reader to Refs. [43, 74, 179–182], as well as to studies in data [10, 183–185].

Quark/gluon discrimination has mostly been studied using IRC safe observables, such as the angularities [131, 186] or 2-point energy correlation functions $C_1 = e_2$ [74], which are set by a single emission at LL accuracy.¹⁹ At LL order, and ignoring nonperturbative effects, one can show that the discrimination power of such observables is set by the Casimir scaling relation

$$\text{disc}(x) = x^{C_A/C_F} = x^{9/4}, \quad (6.1)$$

where x is the fraction of quarks retained by the cut and $\text{disc}(x)$ is the fraction of gluons retained. In this way, discrimination power is capped by the ratio of the gluon and quark color charges, $C_A/C_F = 9/4$. Casimir scaling arises because after a single emission, the discrimination power is set only by the color factor associated with the hard jet core, independent of the particular details of the observable.

Beyond LL accuracy, where one is sensitive to physics beyond the leading emission, improved discrimination power is observed. In Ref. [74], an analytic calculation of C_1 was performed at NLL accuracy, and a noticeable increase in discrimination power beyond the Casimir limit was found for $\beta < 1$ (though not confirmed in an ATLAS study [185]). For small values of β , however, one is highly sensitive to nonperturbative effects, which must be modeled or extracted from data. Particularly for gluon jets, which are not well constrained by LEP event shape data [201–204], this leads to significant discrepancies between distributions obtained from different parton shower generators.²⁰ This in turn leads to rather large uncertainties in the predicted quark/gluon efficiencies; see Refs. [43, 182] for detailed studies.

Given the Casimir scaling limit of single-emission observables, a promising approach for improving quark/gluon discrimination is to design observables that are directly sensitive to multiple emissions within the jet, even at lowest order. In this section, we define a series of observables U_i specifically intended for this purpose. Since these observables exhibit different behavior from standard single-emission observables, they may also prove useful in improving the parton shower description of quark and gluon jets. We will particularly emphasize the stability of their discrimination power as a function of the angular exponent β , which could be helpful for disentangling perturbative and nonperturbative effects.

6.1 Probing Multiple Emissions with U_i

A standard observable for quark/gluon discrimination is the 2-point energy correlation function e_2 , whose scaling was derived already in Eq. (2.17) for 1-prong jets:

$$e_2^{(\beta)} \sim z_s + \theta_{cc}^\beta. \quad (6.2)$$

¹⁹Important exceptions are (IRC unsafe) multiplicity-based observables, which have a long history in QCD [187–198] (see [199] for a recent experimental study), and more recently, shower deconstruction [200].

²⁰This has been coined the “PYTHIA-HERWIG sandwich”, with LHC data as the filling.

As discussed, e_2 is set at LL accuracy by a single emission from the hard core. Note that the scaling is the same for quarks and gluons, since $C_F = 4/3$ versus $C_A = 3$ is not a parametric difference between the samples.

To go beyond this single-emission behavior, we consider the 3-point correlators, ${}_v e_3$, which explicitly probe two emissions from the hard jet core. Using the modes in Table 1a, we derive the following scalings (which were already given in Sec. 5.1):

$$\begin{aligned} {}_1 e_3^{(\beta)} &\sim z_s^2 + \theta_{cc}^\beta, \\ {}_2 e_3^{(\beta)} &\sim z_s^2 + z_s \theta_{cc}^\beta + \theta_{cc}^{2\beta}, \\ {}_3 e_3^{(\beta)} &\sim z_s^2 + z_s \theta_{cc}^\beta + \theta_{cc}^{3\beta}. \end{aligned} \tag{6.3}$$

We can draw a number of interesting conclusions from Eq. (6.3). First, in the majority of phase space there is a direct relationship between the last two 3-point correlators and the 2-point correlator: ${}_2 e_3 \sim (e_2)^2$ and ${}_3 e_3 \sim (e_2)^2$.²¹ We therefore do not expect ${}_2 e_3$ or ${}_3 e_3$ to yield improved quark/gluon discrimination power compared to e_2 ; this illustrates the importance of understanding parametric correlations between different observables. By contrast, ${}_1 e_3$ does not obey such a relation to e_2 , since only for ${}_1 e_3$ is the cross term $\theta_{cc}^\beta z_s$ power suppressed. Since ${}_1 e_3$ directly probes the double-soft limit of a jet, without soft/collinear cross talk at leading power, we can expect it to carry more information about the flavor of the jet's initiating parton. This intuition will be verified in our parton shower study.

Another interesting feature of ${}_1 e_3$ is the relative scaling between the collinear and soft modes, as can be seen from comparing Eq. (6.3) to Eq. (6.2). To improve quark/gluon efficiency with e_2 , one typically needs to use small values of the angular exponent β . Since ${}_1 e_3$ already has a suppressed soft scaling, it can achieve good quark/gluon discrimination at comparatively higher values of the angular exponent. In the parton shower study below, we will find that the performance of ${}_1 e_3$ with $\beta = 2$ is comparable to e_2 with $\beta = 0.2$. This relative scaling also modifies the structure of nonperturbative corrections, although we will not discuss this aspect further in this paper.²² Note that the discrimination power as a function of β is not a prediction of power counting and can only be obtained by explicit calculations (or measurements) of the distributions.

Seeing the potential of ${}_1 e_3$, it is natural to consider higher-point correlators. For an $n + 1$ point correlator, we have

$${}_1 e_{n+1}^{(\beta)} \sim z_s^n + \theta_{cc}^\beta, \tag{6.4}$$

which probes the n -soft limit, again without soft/collinear cross talk at leading power. We are therefore led to define the U_i series of observables,

$$U_i^{(\beta)} = {}_1 e_{i+1}^{(\beta)}, \tag{6.5}$$

²¹Because of the $\theta_{cc}^{3\beta}$ term, this parametric relation is strictly speaking not true for ${}_3 e_3$, but the difference is power suppressed in much of the phase space.

²²Our reluctance to weigh in on nonperturbative corrections is because a standard shape function analysis [205–209], which is applicable for e_2 , does not hold for ${}_1 e_3$. In future work, we might hope to extend the shape function logic to non-additive observables like ${}_1 e_3$.

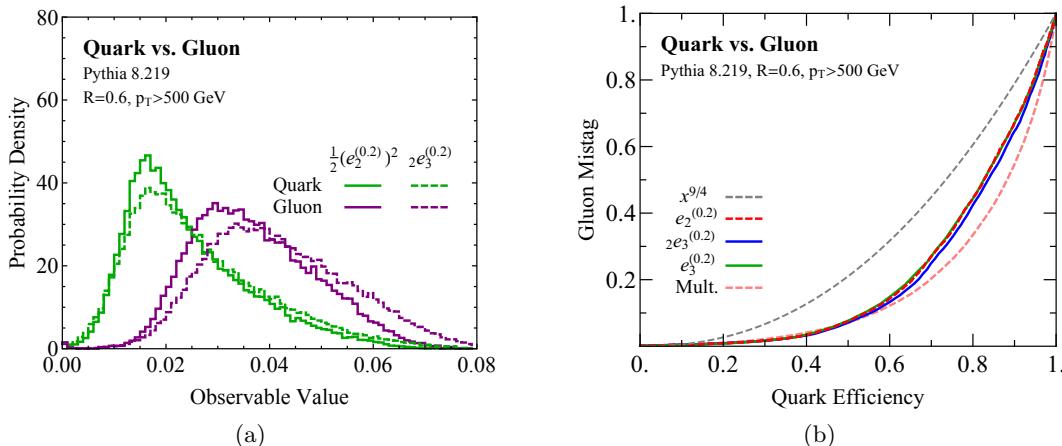


Figure 17: Comparison of the 3-point correlators, $2e_3$ and $3e_3$, with the 2-point correlator, $e_2 = U_1$. The fact that these observables are related by power counting is shown by verifying (a) the scaling relation $2e_3 \sim \frac{1}{2}(e_2)^2$ at the level of distributions and (b) the nearly identical quark/gluon discrimination power using a ROC curve. The prediction from Casimir scaling and the result for hadron multiplicity are shown for reference.

for quark/gluon discrimination. The reason one might expect U_i to perform better with increasing i is that higher-point correlators can effectively “count” more emissions than lower-point correlators. Since gluon jets generate more emissions than quark jets, on average by a factor of C_A/C_F , one expects improved quark/gluon contrast with each additional emission probed; this intuition will be borne out in the parton shower study below. More generally, we hope that these observables will prove useful for probing the structure of the QCD shower.

From the power counting in Eq. (6.4), we see that the scaling of the soft modes for U_i depends on the index i as z_s^i . One might therefore naively think that after grooming is applied, all the U_i observables would be identical. This is not the case for a fixed value of z_{cut} , however, since the soft scale increases as a function of i . To emphasize this point, the average values of U_i are typically $\langle U_2 \rangle = 0.05$ and $\langle U_3 \rangle = 0.01$ (see Fig. 14 from our parton shower study below). By Eq. (6.4), these correspond to z_s values of $z_s \simeq 0.25$ and $z_s \simeq 0.4$, respectively, both of which are well above the $z_{\text{cut}} = 0.1$ scale that we use as our grooming benchmark. Therefore, the emissions that dominate the U_2 and U_3 distributions are not actually removed by our grooming procedure. Thus, the behavior of U_i is expected to be more resilient to grooming for larger values of i .

6.2 Performance in Parton Showers

We now use a parton shower study to verify the above power-counting predictions and to assess quantitatively the potential improvements in quark/gluon discrimination power achievable using higher-point correlators. For reasons of computational time we restrict

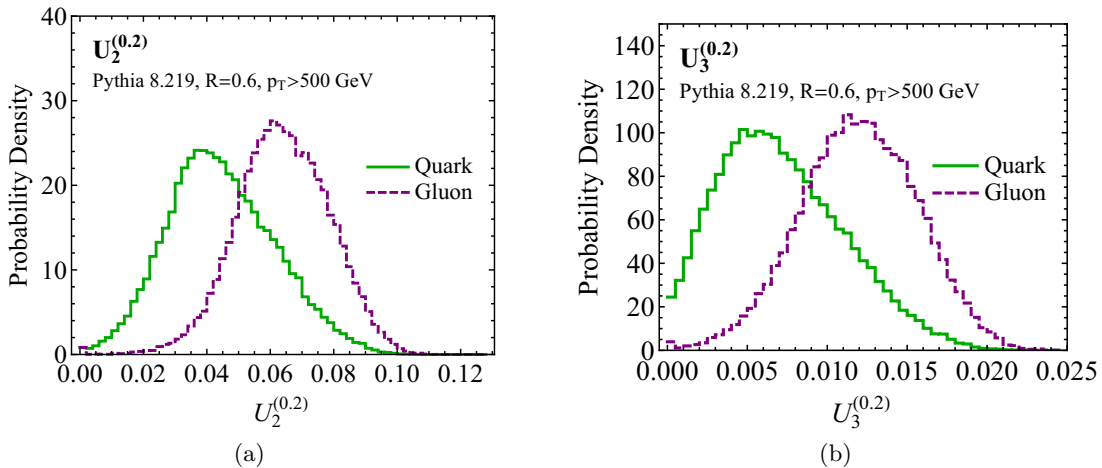


Figure 18: Distributions of (a) U_2 and (b) U_3 for $\beta = 0.2$, as measured on quark and gluon jets.

our study of the U_i series to $i = 1, 2, 3$.²³ The quark and gluon jets are generated from the same PYTHIA $pp \rightarrow Z + j$ samples described in Sec. 5.2, and the same overall analysis strategy applies, though no cut is placed on jet masses. Furthermore, we use a smaller jet radius of $R = 0.6$. Given known parton shower uncertainties, it would be interesting to study different shower and hadronization algorithms to understand the degree to which LHC measurements of U_i could provide insight into quark/gluon tagging; we leave such studies to future work.

We begin by verifying the power-counting argument of Eq. (6.3), which suggested that ${}_{2e_3}$ and e_3 should be highly correlated with $U_1 = C_1 = e_2$. Even though ${}_{2e_3}$ and e_3 probe three particle correlations, they have a fixed scaling relation with respect to e_2 , and are therefore not expected to provide new information for quark/gluon tagging. Taking ${}_{2e_3}$ as a representative example in Fig. 17a, we compare the distributions of ${}_{2e_3}$ and $\frac{1}{2}(e_2)^2$; they are remarkably similar so we conclude that power counting is indeed capturing the dominant scaling relation. From the ROC curves in Fig. 17b, we see that the discrimination power of e_2 , ${}_{2e_3}$, and ${}_{3e_3}$ are very similar for the same value of β , with limited improvement observed by including 3-particle correlations. This emphasizes that probing multi-particle correlations does not, in and of itself, improve quark/gluon discrimination, since higher-point correlation functions can be correlated with lower-point correlation functions.

We now consider the behavior of U_2 and U_3 , which were designed to exploit multi-particle correlations to improve quark/gluon discrimination. In Fig. 18, we show distributions of U_2 and U_3 with $\beta = 0.2$, indicating good separation of the quark and gluon samples. This is quantified in Fig. 19a, which shows ROC curves for U_i comparing $i = 1, 2, 3$. Recall that $U_1 = C_1 = e_2$ is a standard quark/gluon discriminant and a useful baseline to assess performance gains (even if PYTHIA itself skews optimistic about quark/gluon separation

²³For a jet with n_J particles, the computational cost of U_i scales like n_J^{i+1} . On a typical laptop, the analysis of a single jet takes around {0.14 ms, 0.86 ms, 11 ms} for $\{U_1, U_2, U_3\}$.

power [43, 74]). Going from U_1 to U_2 to U_3 , the discrimination power at high efficiencies does increase with more emissions being probed, though the change is relatively small going from $i = 2$ to $i = 3$.

Beyond absolute performance gains, it is also interesting to study the relative performance of U_i as a function of the angular exponent β . In Fig. 19b, we show the gluon rejection at 70% quark efficiency as a function of β .²⁴ Unlike for $U_1 = e_2$, where the discrimination power falls off rapidly with increasing β , for U_2 , and even more so for U_3 , the discrimination power remains well above the Casimir scaling limit, even into the large β regime where U_i should be amenable to fixed-order or resummed perturbative calculations. We find this much flatter behavior of the discrimination power with respect to β to be one of the most interesting features of these observables, suggestive that multiple soft emissions are just as important as hard collinear emissions for discriminating quarks from gluons. Full ROC curves for different values of the angular exponents are provided in App. E.

It would be interesting to see if there is asymptotic behavior as $i \rightarrow \infty$, though this is likely only meaningful in the context of a comparative study of parton shower generators, since it depends sensitively on the assumptions made for correlated soft emissions. As a first step in this direction, in Fig. 18 we compare U_i to hadron multiplicity, which is known to be a powerful quark/gluon discriminant. Remarkably, the performance of the U_i observables appears to asymptote to multiplicity as i is increased, both in the shape of the ROC curves as well as in the behavior as a function of β . It would be interesting to understand whether this connection can be made formal, and whether the U_i observables can be used to give an IRC safe definition of a multiplicity-like observable.

Finally, we want to test whether this improvement in quark/gluon discrimination power is robust to grooming. In Fig. 20, we compare the U_2 and U_3 distributions before and after grooming has been applied. At large values of the observables, relatively little difference is observed for our baseline grooming parameters, as expected from the power-counting analysis of Sec. 6.1. At smaller values of the observables, there is a distortion in the distributions due to the fact that grooming substantially decreases the overall particle multiplicity. In particular, there are expected features at $U_2 = 0$ ($U_3 = 0$), from when the grooming gives less than three (four) particles in the jet. In this regime, power-counting arguments are no longer applicable since the distribution is dominated by nonperturbative effects. That said, as shown in App. E, the ROC curves after grooming exhibit the same features as in the ungroomed case, with U_2 and U_3 outperforming U_1 , indicating that this parametric prediction is still robust.

It would be of great interest to perform explicit calculations of U_2 to understand its exact dependence on the color Casimirs, as well as on the angular exponent β . A resummed calculation, in particular, would shed light onto the all-orders structure of multiple-emission observables, which have not been widely explored in the literature.²⁵ It would also be useful

²⁴We chose 70% quark efficiency as a benchmark, since it was used in the recent study of Ref. [10], though the features emphasized in the text are largely independent of this particular choice. At very low quark efficiencies, deep in the nonperturbative regime, the different U_i behaviors merge.

²⁵See Refs. [56, 58] for discussions of factorization and resummation of such observables, and Refs. [40, 94] for fixed-order studies.

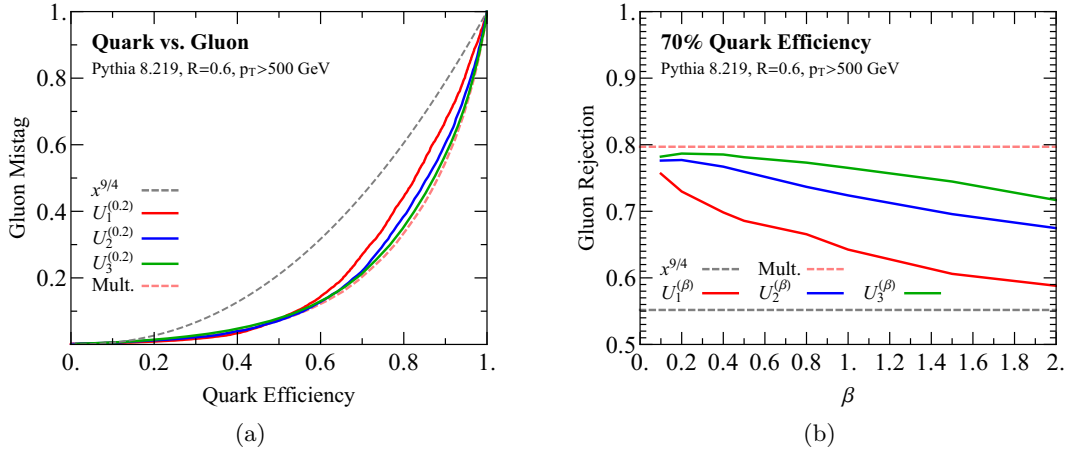


Figure 19: Comparison of the quark/gluon discrimination power for U_1 , U_2 , and U_3 to the prediction from Casimir scaling and the result for hadron multiplicity. (a) ROC curves demonstrating the improvement in performance as more emissions are probed. (b) Gluon rejection at 70% quark efficiency as a function of the angular exponent β . The performance of the U_i observables appears to asymptote to hadron multiplicity as i is increased.

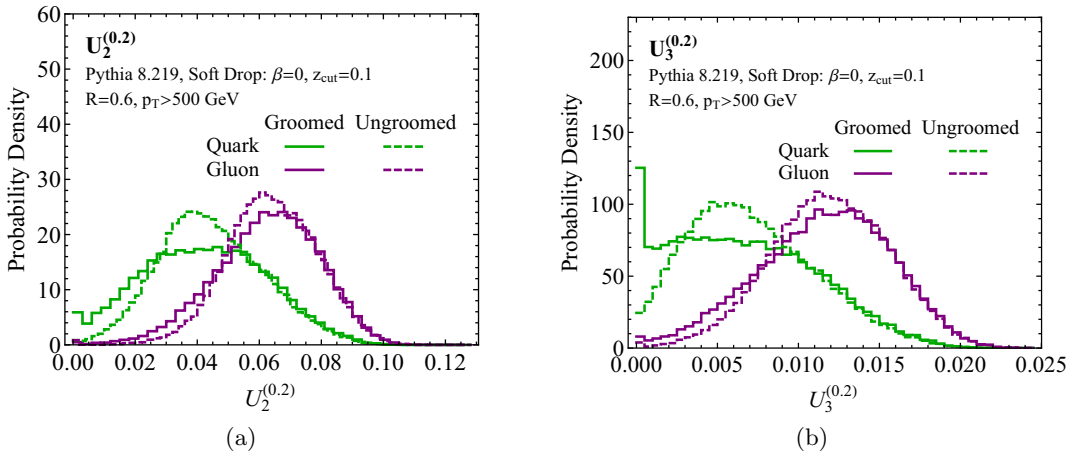


Figure 20: Distributions of (a) U_2 and (b) U_3 for $\beta = 0.2$, before and after grooming. At large values of the observable, grooming has no impact on either the quark or gluon distribution, as expected. The corresponding groomed ROC curves are given in Fig. 30. In (b), the bin at zero is due to jets that have three or fewer particles after grooming.

to understand whether the measurement of multiple U_i observables with different β values could be used to improve quark/gluon discrimination. The multi-differential cross section for $U_1 = e_2$ with two different angular exponents was calculated in Refs. [54, 55] and the gains in performance for quark/gluon discrimination were studied in Ref. [43] from the perspective of mutual information. In preliminary investigations, we find that correlations among the U_i are indeed helpful, but we leave a detailed study to future work.

7 Conclusions

Continued progress in jet substructure relies on the ability to devise observables that can probe increasingly detailed aspects of jets. In this paper, we used the known structures imposed by IRC safety to motivate the generalized energy correlation functions, $v e_n$, a flexible basis for constructing new substructure discriminants. These generalized correlators incorporate an angular weighting function, allowing them to probe different angular structures within a jet. We presented a number of case studies of relevance to the jet substructure community—boosted top tagging, boosted $W/Z/H$ tagging, and quark/gluon discrimination—demonstrating the power of power-counting techniques to design discriminants for specific purposes. In each case, our newly-developed observables outperform standard jet shapes in parton shower studies.

The three series of observables introduced in this paper— M_i , N_i , and U_i —exhibit new ways to probe the soft and collinear limits of QCD. The M_i series is designed for tagging groomed jets, showing that the removal of soft radiation can dramatically change the phase space of i -prong discriminants. The N_i series is designed to mimic N -subjettiness in the limit of resolved substructure, showing how to probe radiation patterns around collinear prongs without requiring external axes. Finally, the U_i series is designed to evade the usual quark/gluon limitations imposed by Casimir scaling, showing the importance of multiple soft emissions for quark/gluon radiation patterns. Taken together, these observables widen the scope for jet substructure investigations, allowing more handles to optimally use jets at the LHC.

Given their tagging performance, it would be interesting to calculate these observables from first principles. This would provide insights into the impact of jet grooming on multi-prong observables, the difference between axes-based and axes-free observables, and the structure of multiple emissions within quark/gluon jets. We are particularly interested in the differences between groomed and ungroomed distributions, since jet grooming not only changes the power counting of observables, but it also changes the logarithmic structure and power corrections in analytic calculations [41, 42, 44, 60, 61, 86]. Beyond jet substructure, we suspect that the generalized correlators could eventually be useful as a tool for performing NNLO calculations; powerful slicing schemes have been devised using N -jettiness [210, 211] and $v e_n$ -based slicing could potentially be valuable in regimes where axes are inappropriate or cumbersome.

One aspect of jet substructure that has not been studied here is the correlations between discriminants. We did apply power-counting techniques to identify correlations among basis elements to define optimal discriminants, but we did not consider whether

power-counting could reveal parametric relationships between different proposed discriminants. Along similar lines, we did not consider in detail the hybrid strategy of using both groomed and ungroomed observables. In preliminary investigations, we find that, not surprisingly, discriminants with the same power counting are highly correlated. When discriminants have different power counting, though, there appears to be additional information gained through multi-variate combinations. At the moment, our application of power counting does not tell us what these multi-variate correlations are or whether we can robustly predict high-performing combinations. We look forward to developing more sophisticated power-counting strategies to exploit these correlations in the future.

Finally, we want to emphasize the importance of first-principles calculations and unfolded experimental measurements of U_1 , U_2 , and U_3 . While the expected tagging performance of 2- and 3-prong discriminants—like M_2 , N_2 , $D_2^{(1,2)}$, and N_3 —can be seen directly from power-counting arguments, this is not the case for quark/gluon discriminants, since C_F and C_A are not parametrically different quantities. For 1-prong jets, power counting can tell us which soft/collinear features are probed by the U_i series, but it cannot reliably predict their expected parametric behavior or relative performance. In parton shower studies, we do find that U_2 and U_3 exhibit improved performance over naive Casimir scaling, even in the larger β regime where they are under better perturbative control, suggesting that the U_i series is a sensitive probe of the QCD shower. Therefore, measurements of the U_i series, along with comparisons to parton shower (and eventually analytic) predictions, are likely to lead to deeper understanding of jets in QCD.

Acknowledgments

We thank Philip Harris, Andrew Larkoski, Simone Marzani, Ben Nachmann, Sid Narayanan, Duff Neill, Sal Rappoccio, and Nhan Tran for helpful discussions, and we thank Matteo Cacciari, Gavin Salam, and Gregory Soyez for help developing the `EnergyCorrelator` `FASTJET` `CONTRIB`. IM is supported by the U.S. Department of Energy (DOE) under cooperative research agreement DE-SC0011090. The work of LN and JT is supported by the DOE under grant contract numbers DE-SC-00012567 and DE-SC0015476. JT is also supported by a Sloan Research Fellowship from the Alfred P. Sloan Foundation. This work was performed in part at the Aspen Center for Physics, which is supported by National Science Foundation grant PHY-1066293.

A Alternative Angular Weighting Functions

As discussed in Sec. 3.1, any symmetric function of the angles, $f_N(\hat{p}_{i_1}, \hat{p}_{i_2}, \dots, \hat{p}_{i_N})$, that vanishes in the collinear limits can in principle be used in Eq. (3.1). While we argued in Sec. 3.2 that the min function is particularly effective due to its ability to isolate hierarchical angular structures, other functional forms can certainly be used. In this appendix, we study two alternate definitions of the angular weighting function, which, from a power counting perspective, are identical to those considered in the text.

For concreteness, we study variants of the N_2 observable from Sec. 5, which was based on a 3-point correlator:

$${}_2e_3^{(\beta)} = \sum_{1 \leq i < j < k \leq n_J} z_i z_j z_k \min \left\{ \theta_{ij}^\beta \theta_{ik}^\beta, \theta_{ij}^\beta \theta_{jk}^\beta, \theta_{ik}^\beta \theta_{jk}^\beta \right\} \Rightarrow N_2^{(\beta)} = \frac{{}_2e_3^{(\beta)}}{({}_1e_2^{(\beta)})^2}. \quad (\text{A.1})$$

One variant is to consider an angular weighting function that smoothly approximates the min function.²⁶

$${}_2r_3^{(\beta)} = \sum_{1 \leq i < j < k \leq n_J} z_i z_j z_k \left(\frac{1}{\theta_{ij} \theta_{ik}} + \frac{1}{\theta_{ij} \theta_{jk}} + \frac{1}{\theta_{ik} \theta_{jk}} \right)^{-\beta} \Rightarrow R_2^{(\beta)} = \frac{{}_2r_3^{(\beta)}}{({}_1e_2^{(\beta)})^2}. \quad (\text{A.2})$$

Another variant is to use the geometric fact that in the collinear limit, the minimum product of pairwise distances is parametrically the same as the area of the triangle spanned by the three points²⁷

$${}_2a_3^{(\beta)} = \sum_{1 \leq i < j < k \leq n_J} z_i z_j z_k \left(\sqrt{s(s - \theta_{ij})(s - \theta_{ik})(s - \theta_{jk})} \right)^\beta \Rightarrow A_2^{(\beta)} = \frac{{}_2a_3^{(\beta)}}{({}_1e_2^{(\beta)})^2}, \quad (\text{A.3})$$

where $s = (\theta_{ij} + \theta_{jk} + \theta_{ik})/2$ comes from Heron's formula. While A_2 is parametrically identical to N_2 , it has the interesting property that it vanishes when the vectors defining the three particles are coplanar, similar to dipolarity introduced in Ref. [212].

Even though the N_2 , R_2 , and A_2 observables have identical power counting, their distributions could in principle differ by $\mathcal{O}(1)$ numbers, possibly allowing for improved discrimination power. In Fig. 21a we compare the distributions of these three observables in PYTHIA, showing that they are rather similar. To aid the eye, we have rescaled the R_2 and A_2 distributions to match the N_2 distribution. Turning to the Z versus quark ROC curve in Fig. 21b, the performance is nearly identical. This further emphasizes that the behavior of the observables is dominated by parametric scalings. Since we did not find any gains from using these more complicated variants, we restricted the study in the text to the definition given in Eq. (3.3).

It is still an interesting question whether other choices of angular weighting functions might lead to improved performance in more complicated jet substructure applications. It seems unlikely, however, since for small radius jets, one can Taylor expand the angular function in the small θ limit, and observables with the same power counting must have the same lowest-order expansion. In practice, the use of smoother definitions which approximate the min function might be useful for performing perturbative calculations.

²⁶The r notation is motivated by the resistance formula for a set of parallel resistors.

²⁷To mimic the behavior of ${}_1e_3$, one could consider the triangle area divided by its perimeter, which is parametrically related to the smallest distance in the collinear limit.

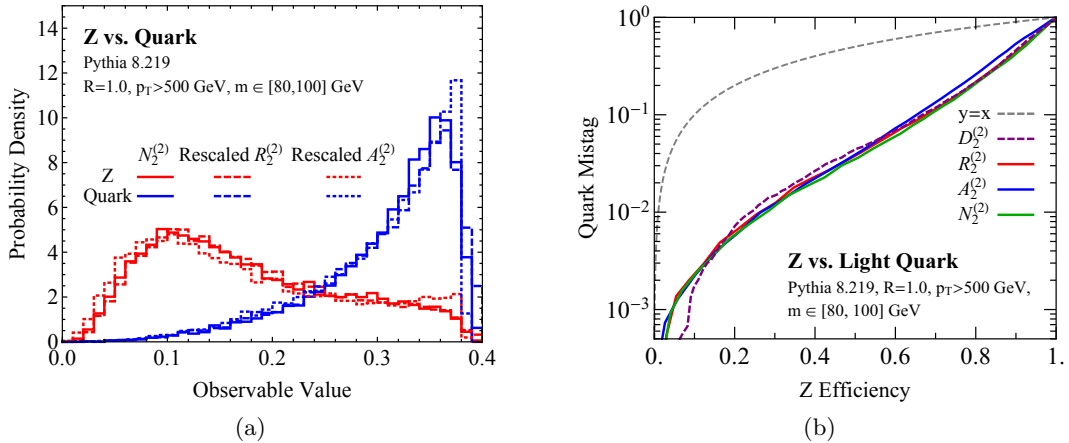


Figure 21: Two alternative definitions of the N_2 -style observable— R_2 and A_2 . (a) Distributions on Z and quark samples. (b) ROC curves for discrimination performance. Since the alternative definitions have identical power counting to N_2 , they exhibit parametrically similar behavior.

B Aspects of 3-prong Tagging

B.1 Challenges for M_3

In Sec. 3.3.1, we defined the general series of M_i observables. We saw in Sec. 5 that the M_2 observable was an effective boosted $W/Z/H$ tagger on groomed jets. One might therefore consider the M_3 observable,

$$M_3^{(\beta)} = \frac{{}_1e_4^{(\beta)}}{{}_1e_3^{(\beta)}}, \quad (\text{B.1})$$

as a possible boosted top tagger.

We can see from a power-counting analysis, however, that even with grooming, M_3 will not perform well. Following the notation of Sec. 4.1, a strongly-ordered 3-prong jet has

$$\begin{aligned} \text{3-prong signal (groomed):} \quad & {}_1e_3^{(\beta)} \sim \theta_{23}^\beta, \\ & {}_1e_4^{(\beta)} \sim z_{ccs}\theta_{23}^\beta + \theta_{cc}^\beta, \end{aligned} \quad (\text{B.2})$$

while a 2-prong background jet has

$$\begin{aligned} \text{2-prong background (groomed):} \quad & {}_1e_3^{(\beta)} \sim z_{cs}\theta_{cs}^\beta + \theta_{cc}^\beta, \\ & {}_1e_4^{(\beta)} \sim z_{cs}^2\theta_{cs}^\beta + \theta_{cc}^\beta. \end{aligned} \quad (\text{B.3})$$

For signal jets, we have the relation ${}_1e_4 \ll {}_1e_3$, so we would like the background to satisfy ${}_1e_4 \sim {}_1e_3$. That desired relation is violated, though, by contributions of the collinear-soft

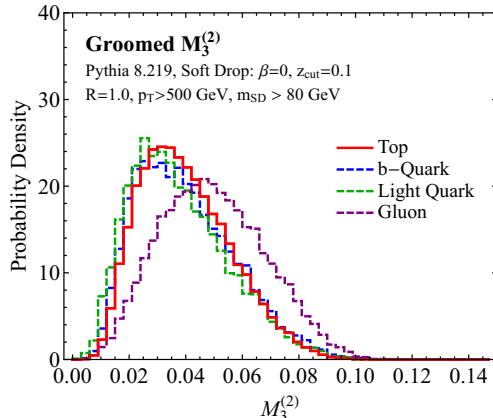


Figure 22: Distributions of M_3 , comparing the signal of boosted top jets to the background of b -quarks, light quarks, and gluons. As expected from power counting, limited discrimination is observed.

modes to $1e_4$, due to the different z_{CS} scalings in Eq. (B.3). We therefore predict from power counting that M_3 should be a poor discriminant.

In Fig. 22, we show the distribution of M_3 for boosted top jets compared to those from QCD jet backgrounds, where little discrimination power is observed. Similar to how ordinary grooming was required for M_2 to become an effective discriminant in the 2-prong case, it is likely that another layer of grooming is needed to remove the undesired collinear-soft contributions to M_3 and make it an effective 3-prong tagger. While we do not pursue M_3 further in this paper, it would be interesting to consider alternative grooming methods designed to isolate 3-prong structure and mitigate both soft and collinear-soft radiation. As a starting point, one could consider doubly-soft-dropped boosted top jets, where after an initial application of soft drop, one reapplies soft drop to the two remaining prongs.

B.2 N_3 Without Grooming

In Sec. 4.1, we argued that on groomed jets with well-resolved substructure, N_3 behaves parametrically like $\tau_{3,2}$, but exhibits improved discrimination power in the transition to the unresolved region. On ungroomed jets, however, N_3 behaves differently from $\tau_{3,2}$, and in particular, it does not provide good discrimination in regions of phase space where there is a soft wide-angle subjet. This same issue was discussed in detail for the case of D_3 in Ref. [66]; the treatment of the soft subjet region of phase space required the addition of two extra terms to D_3 , leading to the complicated form shown in Eq. (2.7). To avoid the soft subjet issue, and to advocate for the stability of groomed observables, we explicitly focused on the case of groomed top jets in Sec. 4.1.

Here, we compare N_3 and $\tau_{3,2}$ on ungroomed jets. Though N_3 was not designed for use on ungroomed jets, it still provides reasonably good discrimination power, though not as good as $\tau_{3,2}$. Distributions of ungroomed N_3 are shown in Fig. 23a, where we use an

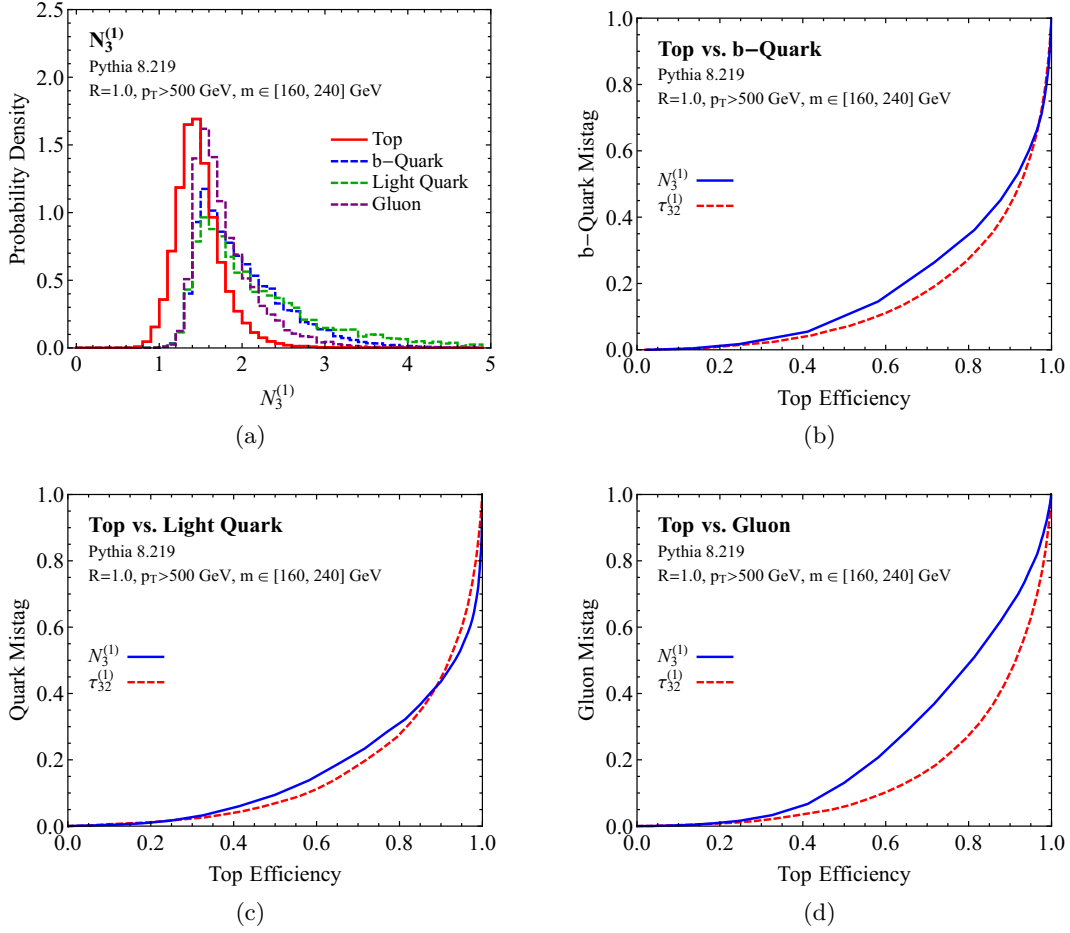


Figure 23: Behavior of N_3 without grooming. (a) Distributions of N_3 for boosted top signals compared to b -quark, light quark, gluon backgrounds. (b,c,d) ROC curves comparing the discrimination power of N_3 versus $\tau_{3,2}$ against the different QCD backgrounds.

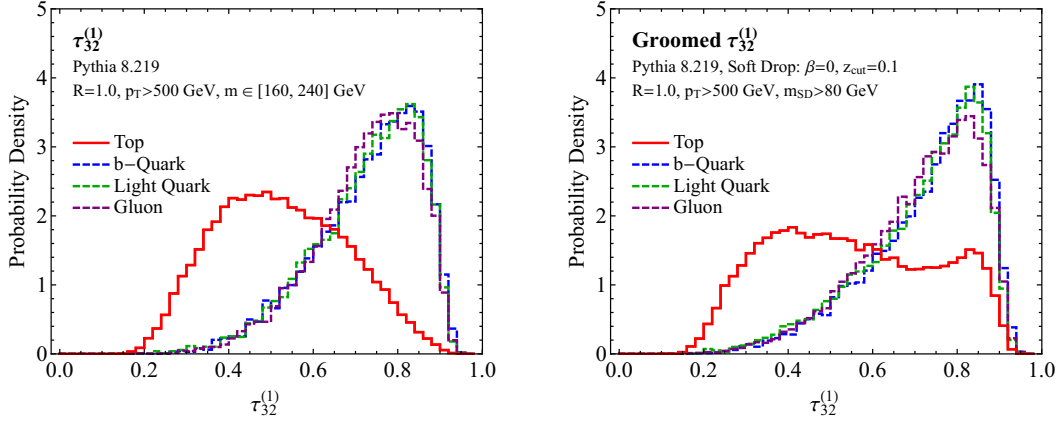


Figure 24: Distributions of the N -subjettiness ratio $\tau_{3,2}$ (a) before grooming and (b) after grooming for both the boosted top signal and the different QCD backgrounds.

alternative mass window cut of $m \in [160, 240]$ GeV. The discrimination performance for the top signal against the b -quark, light quark, and gluon jet backgrounds are shown in Figs. 23b, 23c, and 23d, respectively. The best performance is seen in rejecting quark jets, although ungroomed N_3 has worse performance on gluon jets. Interestingly, similar quark/gluon differences were seen for D_3 in Ref. [140], although the nature of this behavior is not understood and is not necessarily connected in any way to the use of energy correlators.

Though N_3 was designed for use on groomed jets, we believe that N_3 is a sufficiently good discriminant on ungroomed jets to merit further investigations. At minimum, ungroomed N_3 distributions could be measured as a baseline to test the impact of jet grooming. We offer a bounty to the first group that identifies an axes-free observable with the same power counting as ungroomed $\tau_{3,2}$.

For completeness, in Fig. 24, we show the N -subjettiness observable $\tau_{3,2}$ as measured on the same samples, both before and after grooming. As expected, excellent discrimination power is observed before grooming. After grooming, the discrimination power is worsened primarily due to the behavior in the unresolved region, namely as $\tau_{3,2} \rightarrow 1$. It is in this region that N_3 exhibits improved performance, as seen already in the behavior of the distributions in Fig. 8 and the performance in the ROC curve in Fig. 9.

B.3 Identifying N_3

In Sec. 4.1, we considered the observable N_3 defined as

$$N_3^{(\beta)} = \frac{2e_4^{(\beta)}}{(1e_3^{(\beta)})^2}. \quad (\text{B.4})$$

There are, however, a large number of other possible observables that could be formed from combinations of the different 2-, 3-, and 4-point correlators. In this appendix, we describe in more detail the justification for our focus on N_3 . It is interesting that this

process happens to identify an observable with the same parametric behavior as the N -subjettiness ratio $\tau_{3,2}$. As discussed in the text, we focus on the case of groomed jets. This means that we can ignore soft radiation for our power counting analysis.

For groomed boosted top jets, it is sufficient to consider a 3-prong configuration with hierarchical angles, as illustrated in Fig. 5b. In particular, we do not have to consider the soft subjet phase space region from Ref. [66], which has hierarchical energies, since those configurations are removed by the grooming procedure. For the 3-prong signal, the scaling of the 2-point correlator is

$$e_2^{(\beta)} \sim \theta_{12}^\beta, \quad (\text{B.5})$$

the scalings of different 3-point correlators are

$$\begin{aligned} 3e_3^{(\beta)} &\sim \theta_{23}^\beta \theta_{12}^{2\beta}, \\ 2e_3^{(\beta)} &\sim \theta_{23}^\beta \theta_{12}^\beta, \\ 1e_3^{(\beta)} &\sim \theta_{23}^\beta. \end{aligned} \quad (\text{B.6})$$

and the scalings of the different 4-point correlators are

$$\begin{aligned} 6e_4^{(\beta)} &\sim z_{cs} \theta_{12}^{5\beta} \theta_{23}^\beta + z_{ccs} \theta_{12}^{3\beta} \theta_{23}^{3\beta} + \theta_{23}^\beta \theta_{cc}^\beta \theta_{12}^{4\beta}, \\ 5e_4^{(\beta)} &\sim z_{cs} \theta_{12}^{4\beta} \theta_{23}^\beta + z_{ccs} \theta_{12}^{2\beta} \theta_{23}^{3\beta} + \theta_{23}^\beta \theta_{cc}^\beta \theta_{12}^{3\beta}, \\ 4e_4^{(\beta)} &\sim z_{cs} \theta_{12}^{3\beta} \theta_{23}^\beta + z_{ccs} \theta_{12}^{1\beta} \theta_{23}^{3\beta} + \theta_{23}^\beta \theta_{cc}^\beta \theta_{12}^{2\beta}, \\ 3e_4^{(\beta)} &\sim z_{cs} \theta_{12}^{2\beta} \theta_{23}^\beta + z_{ccs} \theta_{23}^{3\beta} + \theta_{23}^\beta \theta_{cc}^\beta \theta_{12}^\beta, \\ 2e_4^{(\beta)} &\sim z_{cs} \theta_{12}^\beta \theta_{23}^\beta + z_{ccs} \theta_{23}^{2\beta} + \theta_{23}^\beta \theta_{cc}^\beta, \\ 1e_4^{(\beta)} &\sim 0 + z_{ccs} \theta_{23}^\beta + \theta_{cc}^\beta, \end{aligned} \quad (\text{B.7})$$

where the alignment and zero in the last line are there just to help guide the eye.

For 2-prong background jets, all we need is the scaling of the 2-point correlator,

$$e_2^{(\beta)} \sim \theta_{cs}^\beta, \quad (\text{B.8})$$

and the scalings of the different 3-point correlators,

$$\begin{aligned} 3e_3^{(\beta)} &\sim z_{cs} \theta_{cs}^{3\beta} + \theta_{cs}^{2\beta} \theta_{cc}^\alpha, \\ 2e_3^{(\beta)} &\sim z_{cs} \theta_{cs}^{2\beta} + \theta_{cs}^\beta \theta_{cc}^\alpha, \\ 1e_3^{(\beta)} &\sim z_{cs} \theta_{cs}^\beta + \theta_{cc}^\alpha. \end{aligned} \quad (\text{B.9})$$

While the background scalings of the 4-point correlators would be needed to verify signal/background separation, as was done in Sec. 4.1, they are not needed to restrict the combinations under consideration. Since their form is not particularly illuminating, we do not show them here.

While there are a large number of observables listed above, the analysis can be simplified by noting that for both the signal and background, the information contained in

the 3-point correlators ${}_2e_3$ and ${}_3e_3$ is redundant, since it can be expressed in terms of e_2 and ${}_1e_3$. Furthermore, any observable derived from power counting will be linear in the 4-point correlator and will have the 3-point correlator appearing in the denominator raised to some power. Finally, from Eq. (B.7), we see that θ_{23} appears at most raised to the third power; it therefore suffices to consider ${}_1e_3$ raised at most to the third power. The power of e_2 is then fixed by Lorentz invariance.

The above logic allows us to write down a parametrically complete set of potential 3-prong observables,

$$\mathcal{O}_{v,y} = \frac{{}_v e_4^{(\beta)} \left(e_2^{(\beta)} \right)^{y-v}}{\left({}_1 e_3^{(\beta)} \right)^y}, \quad v \in \{1, 2, 3, 4, 5, 6\}, \quad y \in \{1, 2, 3\}, \quad y \leq v. \quad (\text{B.10})$$

At this point, one can then either power count each of these options explicitly to test for background isolation, or simply evaluate their performance in a parton shower generator. To limit the number of options to consider, one can apply the further constraint that e_2 should not appear explicitly in the observable, to mitigate correlations with the jet mass. This is equivalent to setting $y = v$, and gives

$$T_v = \frac{{}_v e_4^{(\beta)}}{\left({}_1 e_3^{(\beta)} \right)^v}. \quad (\text{B.11})$$

Note that $v = 1$ gives M_3 and $v = 2$ gives N_3 . Among all of the $\mathcal{O}_{v,y}$ observables, we found that the best performing one in PYTHIA was N_3 , which then became the focus of our boosted top study.

B.4 Power Counting N_3

While the identification of the parametrically optimal discriminant is usually fairly straightforward given the parametric expressions for the observables, confusions can arise when the scalings have multiple terms. Here, we present more details for the signal analysis of the N_3 observable from Sec. 4.1, to illustrate how power counting can be performed systematically. This allows one to avoid potential confusions when there are competing parametric relations. This same approach can be used in the other examples studied in the paper, though for the 1- and 2-prong case studies, we find that the more heuristic treatment in the text is just as illuminating as the systematic strategy.

We begin by recalling the power counting for ${}_1e_3$ and ${}_2e_4$, considering the signal with (hierarchical) 3-prong substructure:

$$\begin{aligned} {}_1 e_3^{(\beta)} &\sim \theta_{23}^\beta, \\ {}_2 e_4^{(\beta)} &\sim z_{cs} \theta_{12}^\beta \theta_{23}^\beta + z_{ccs} \theta_{23}^{2\beta} + \theta_{23}^\beta \theta_{cc}^\beta. \end{aligned} \quad (\text{B.12})$$

We next need to identify which of the parameters— θ_{12} , θ_{23} , θ_{cc} , z_{cs} , and z_{ccs} —are set by which measurements. Since most boosted top analyses apply a mass cut, we assume that θ_{12} is set by a mass measurement. This is not crucial, however, and the argument below

can be generalized without the fixed-mass assumption. This leaves us with the task of determining the parametric relationship between $\{\theta_{23}, \theta_{cc}, z_{cs}, z_{ccs}\}$ and $\{1e_3, 2e_4\}$. Clearly, the measurement of $1e_3$ sets θ_{23} . By assumption, there is no hierarchy between the three terms in $2e_4$, yielding the following scaling of the kinematic variables:

$$\theta_{23}^\beta \sim 1e_3^{(\beta)}, \quad \theta_{cc}^\beta \sim \frac{2e_4^{(\beta)}}{1e_3^{(\beta)}}, \quad z_{cs} \sim \frac{2e_4^{(\beta)}}{\theta_{121e_3}^\beta}, \quad z_{ccs} \sim \frac{2e_4^{(\beta)}}{(1e_3^{(\beta)})^2}. \quad (\text{B.13})$$

Now, we want to derive an observable which distinguishes 3-prong jets from jets with fewer than 3 prongs. This can be accomplished by identifying the regions in phase space where the 3-prong EFT description breaks down, and translating that into constraints on the relationship between $1e_3$ and $2e_4$. As given in Eq. (4.1) and illustrated in Fig. 5b, 3-prong phase space is defined by the following four conditions:

$$\begin{aligned} (a) \quad & \theta_{23} \ll \theta_{12} \ll 1, & (b) \quad & \theta_{cc} \ll \theta_{23}, \\ (c) \quad & z_{ccs} \ll 1, & (d) \quad & z_{cs} \ll z_{ccs}, \end{aligned} \quad (\text{B.14})$$

Plugging Eq. (B.13) into condition (a), we find

$$(a) \implies 1e_3^{(\beta)} \ll e_2^{(\beta)} \ll 1. \quad (\text{B.15})$$

This just defines the region of validity of our analysis, but is not helpful in determining a relationship between $1e_3$ and $2e_4$. Turning to condition (b), we find

$$(b) \implies \frac{2e_4^{(\beta)}}{1e_3^{(\beta)}} \ll 1e_3^{(\beta)} \implies \frac{2e_4^{(\beta)}}{(1e_3^{(\beta)})^2} \ll 1. \quad (\text{B.16})$$

Note that the constraint $\theta_{cc} \ll 1$ does not give as strong a bound. Condition (c) gives the same constraint,

$$(c) \implies \frac{2e_4^{(\beta)}}{(1e_3^{(\beta)})^2} \ll 1. \quad (\text{B.17})$$

Finally, we see that condition (d) is already satisfied by condition (a),

$$(d) \implies \frac{2e_4^{(\beta)}}{\theta_{121e_3}^\beta} \ll \frac{2e_4^{(\beta)}}{(1e_3^{(\beta)})^2} \implies 1e_3^{(\beta)} \ll \theta_{12}^\beta. \quad (\text{B.18})$$

and provides no extra information.

From this analysis, one finds that the strongest constraint on the breakdown of the 3-prong EFT is

$$\frac{2e_4^{(\beta)}}{(1e_3^{(\beta)})^2} \ll 1, \quad (\text{B.19})$$

leading to the definition of the N_3 observable,

$$N_3^{(\beta)} = \frac{2e_4^{(\beta)}}{(1e_3^{(\beta)})^2}. \quad (\text{B.20})$$

With practice, one can immediately infer this result from the scaling of the observables in Eq. (B.12), without having to explicitly consider each EFT constraint, but this example illustrates how the procedure can be performed systematically when confusions arises.

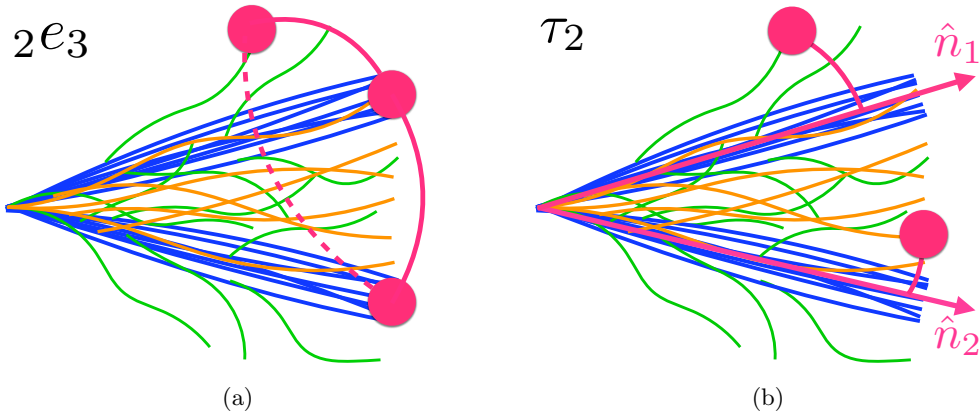


Figure 25: Comparison of the functional structure of (a) $2e_3$ and (b) τ_2 . The $2e_3$ observable correlates triplets of particles (and two of their three pairwise angles), while the τ_2 observable correlates particles with axes.

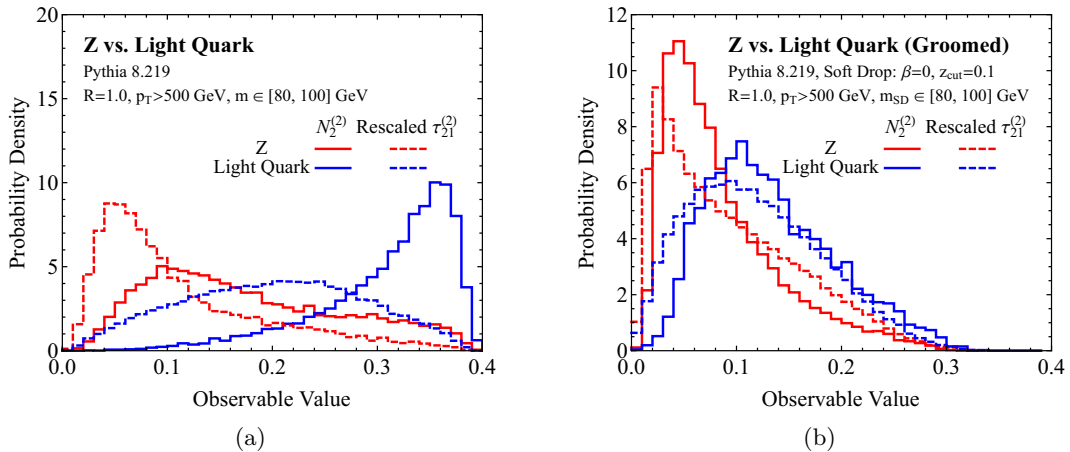


Figure 26: Distributions of N_2 and $\tau_{2,1}$ on the Z signal and quark background (a) before grooming and (b) after grooming. To aid visual comparison, $\tau_{2,1}$ has been rescaled to match the endpoint of N_2 .

C Relationship Between N_i and N -subjettiness

In Sec. 3.3.2, we claimed that the N_i observables and the N -subjettiness ratio observables are related for groomed jets. This was shown explicitly for the case of $i = 3$ in Sec. 4.1. In this appendix, we show that this is generically true, suggesting that N_i is indeed an appropriate observable for identifying i -prong substructure on groomed jets.

Since we work with groomed jets, we do not have to consider soft subjet configurations (i.e. i -prong jets with hierarchical energies). Instead, the power counting is determined by the generalization of Fig. 5b with hierarchical angles, where a jet has i subjets, two of which become collinear and approach an $(i - 1)$ -subjet configuration. We label the two

subjets that approach each other by 1 and 2, such that θ_{12} denotes the angle between them. By assumption, θ_{12} is smaller than the angles between any other subjets (which we power count as $\theta_{st} \sim 1$), but larger than the typical collinear scale θ_{cc} .

By considering the contributions from collinear modes aligned along subjets 1 and 2, we find the parametric relation

$${}_1e_i^{(\beta)} \sim \theta_{12}^\beta \sim \tau_{i-1}^{(\beta)}, \quad (\text{C.1})$$

where all other pairwise combinations of modes are power suppressed. Here, we are assuming that the N -subjettiness axes are defined such that one axis is aligned with subjet 1 or 2, with the remaining $i - 2$ axes aligned along the other subjets; this is indeed the configuration that minimizes τ_{i-1} in the small θ_{12} limit, assuming balanced energies. Adding an extra axis yields

$$\tau_i^{(\beta)} \sim \theta_{cc}^\beta, \quad (\text{C.2})$$

where now the i axes align with the i subjets.

For the correlator involving two angles, the power-counting analysis yields

$${}_2e_{i+1}^{(\beta)} \sim \theta_{12}^\beta \left(\theta_{cc}^\beta + \dots \right) \sim \tau_{i-1}^{(\beta)} \cdot \tau_i^{(\beta)}, \quad (\text{C.3})$$

where the ellipses denote contributions from collinear-soft modes, which depend on the other angles between the subjets. To understand the appearance of $\theta_{12}^\beta \theta_{cc}^\beta$, note that the largest contribution to ${}_2e_{i+1}$ comes from selecting two collinear modes from one subjet and one collinear mode from each of the remaining $i - 1$ subjets; for that configuration, the two smallest pairwise angles are indeed θ_{cc} and θ_{12} .

Generalizing the argument in App. B.4, Eqs. (C.1) and (C.3) imply ${}_2e_{i+1} \ll ({}_1e_i)^2$ on i -prong signal jets, such that the appropriate i -prong discriminant is

$$N_i^{(\beta)} = \frac{{}_2e_{i+1}^{(\beta)}}{({}_1e_i^{(\beta)})^2} \sim \frac{\tau_i^{(\beta)}}{\tau_{i-1}^{(\beta)}}, \quad (\text{C.4})$$

where the last relation should be understood in the power-counting sense. Therefore, as advertised, the N_i observable is indeed related to the N -subjettiness ratio $\tau_{i,i-1}$, and both are expected to be good i -prong discriminants.

As an example to demonstrate this parametric relation, we consider the case $i = 2$, which was alluded to in Sec. 5. The relevant observables are shown schematically in Fig. 25. In Fig. 26, we show distributions of $\tau_{2,1}$ and N_2 before and after grooming for $\beta = 2$, taking quarks as representative of the background. To aid in a visual comparison, we have rescaled the $\tau_{2,1}$ distributions by a common factor to match the N_2 endpoint. Before grooming, the shapes of the two distributions are quite different, with N_2 being much more peaked towards the endpoint for the background. After soft drop has been applied, the distributions for the two observables are quite similar, as predicted by the power-counting discussion above.

Still, there is a non-parametric difference between the $\tau_{2,1}$ and N_2 distributions, which leads to improved tagging performance for N_2 . This can be seen by eye in the groomed plot in Fig. 26b, where the background distribution for N_2 is pushed to higher values while

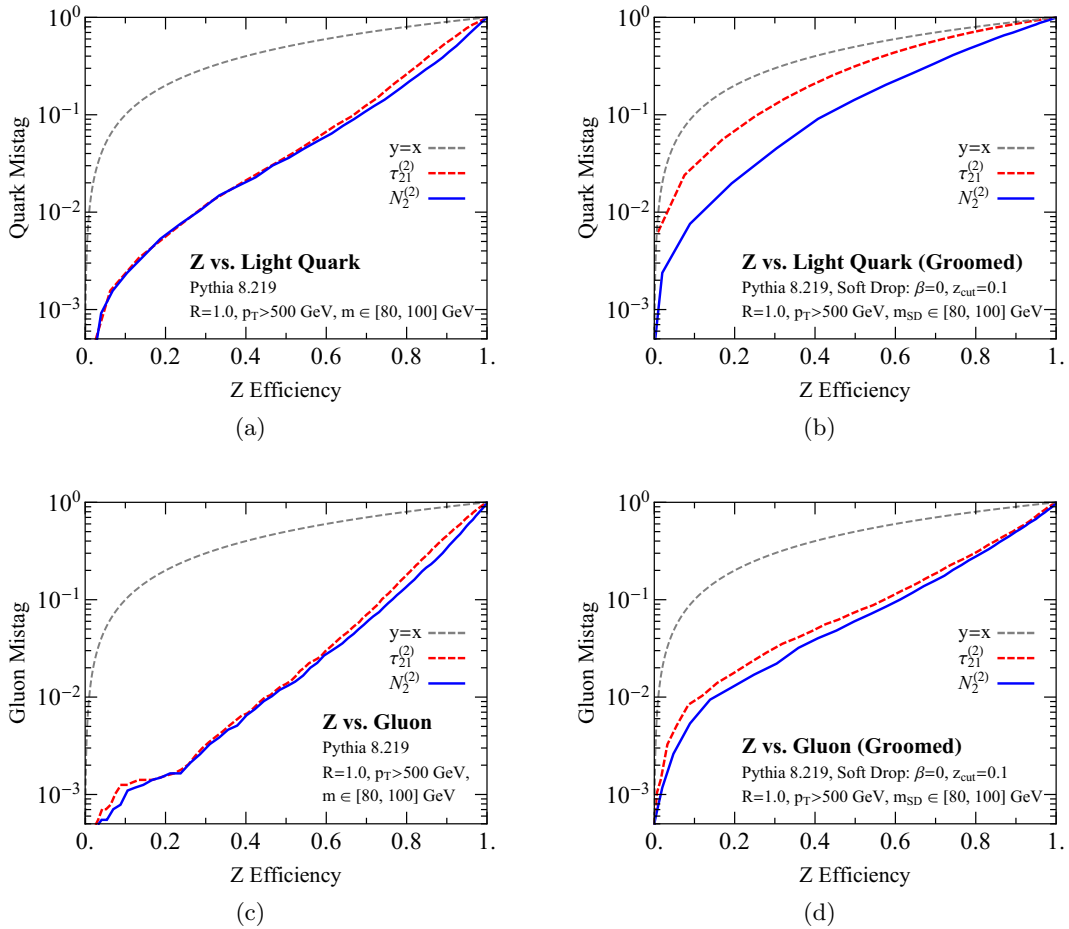


Figure 27: Same as Fig. 15 but comparing N_2 and $\tau_{2,1}$.

the signal distribution is more rapidly falling toward the endpoint. More quantitatively, we can consider the ROC curves in Fig. 27. For the ungroomed case, the discrimination power is similar, with N_2 showing slightly improved behavior at higher efficiencies. For the groomed case, there are significant gains to be had in using N_2 instead of $\tau_{2,1}$.²⁸

D Hybrid Strategies for 2-prong Observables

Throughout the text, we focused on discriminants formed from combinations (often ratios) of either groomed or ungroomed observables. It is also interesting to consider discriminants formed from mixtures of groomed and ungroomed observables [154, 155], which we will refer to as a hybrid strategy. While we will not explore this topic in detail, we take as a simple example ungroomed 2-prong observables after the application of a groomed mass cut.

²⁸While it is possible that different axes choices for N -subjettiness could provide improved performance, it seems to us that any axes definition will be ambiguous in the unresolved region. This also highlights the nice property that N_2 is defined without respect to subjet axes.

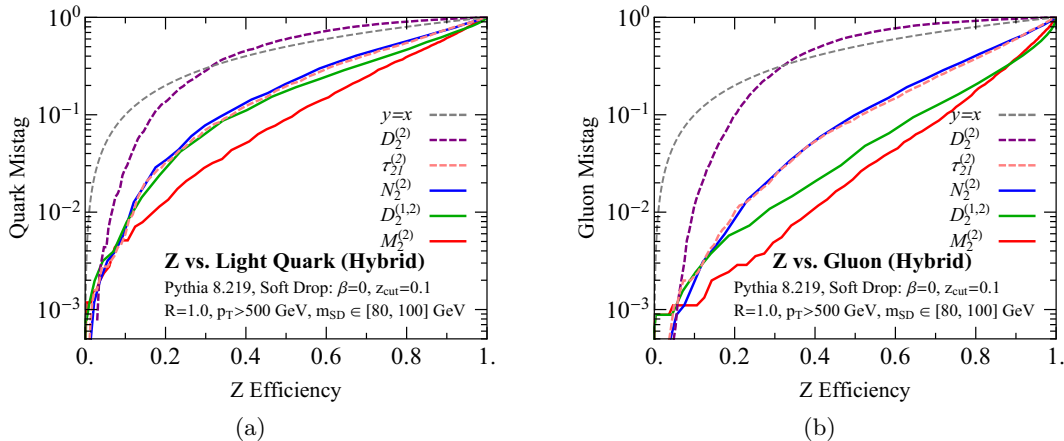


Figure 28: Same as Figs. 15b and 15d but using a hybrid strategy where a cut is placed on the groomed jet mass, but the discriminants are ungroomed.

In Fig. 28, we show the ROC curves for boosted Z discrimination, showing light quark and gluon backgrounds separately; this should be contrasted with Fig. 15. The behavior of these hybrid observables can be understood using the power-counting analysis of Sec. 5.3, where we analyzed the stability of the observables as a function of m_J and p_{TJ} . For signal jets, a cut on the groomed mass has little effect due to the color singlet nature of the Z boson, and therefore the hybrid observables should have a similar behavior to the ungroomed observables. For background QCD jets, however, applying a groomed mass cut in the same mass window enforces a higher effective cut on the ungroomed mass. This, in turn, enters the scaling relations for the background distributions given in Sec. 5.3:

$$M_2^{(2),\text{peak}} \sim \frac{m_J^2}{p_{TJ}^2}, \quad N_2^{(2),\text{max,peak}} \sim \text{const}, \quad D_2^{(2),\text{max}} \sim \frac{p_{TJ}^2}{m_J^2}. \quad (\text{D.1})$$

For M_2 , and similarly for $D_2^{(1,2)}$, using a groomed mass cut has the interesting effect of pushing the ungroomed background distribution to higher values, thereby improving discrimination power. For N_2 , the distribution is parametrically unmodified, and therefore similar discrimination power is expected for the ungroomed and hybrid observables. For $D_2^{(2)}$, larger effective mass values push the distribution to lower values, thereby worsening discrimination power. These power-counting predictions are seen clearly in Fig. 28.

The above behavior is perhaps counterintuitive, especially the poor performance of $D_2^{(2)}$ and the good performance of M_2 , but it follows straightforwardly from the power-counting analysis. That said, the quantitative discrimination power depends crucially on the choice of mass window, and one must keep in mind that this study is based on a relatively narrow soft-dropped mass cut around m_Z . Further studies are therefore warranted to test whether discrimination performance can indeed be improved by simultaneously using information before and after grooming.

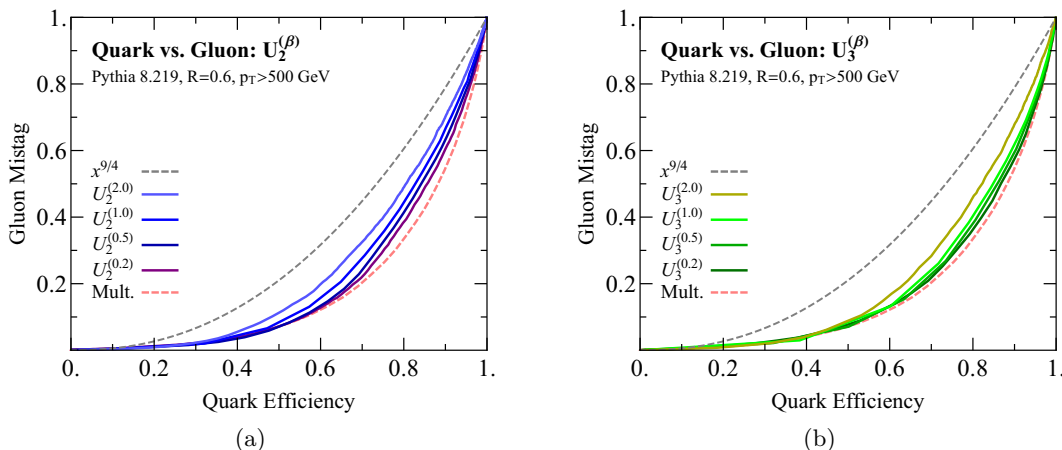


Figure 29: ROC curves as the angular exponent β is varied for (a) U_2 and (b) U_3 . For U_3 , a more stable ROC curve is observed throughout the entire distribution.

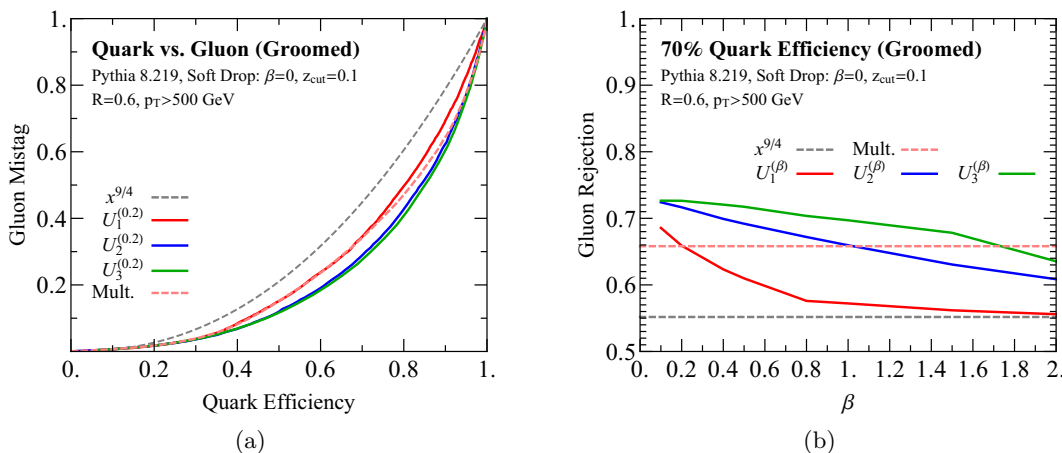


Figure 30: Same as Fig. 19, but after grooming. The improved performance of U_2 and U_3 relative to U_1 is robust to removing soft radiation.

E Supplemental Quark/Gluon Plots

In Fig. 19b, we emphasized the stability of U_i for $i = 2, 3$ as a function of the angular exponent β . In Fig. 29, we show the full ROC curves for both U_2 and U_3 as a function of the angular exponent β . Neither observable asymptotes to the Casimir scaling prediction, even at high efficiencies or high β values. Furthermore, the U_3 distributions exhibit stability as a function of β throughout the whole ROC curve. This would be interesting to verify in an analytic calculation.

In Fig. 30a, we show the ROC curves for U_2 and U_3 after grooming for $\beta = 0.2$, showing

that the U_i series continues to perform better for larger values of i . In Fig. 30b, we show the performance as a function of β , demonstrating the stability of U_3 , even after grooming.

References

- [1] **CMS** Collaboration, S. Chatrchyan et al., *Search for a Higgs boson in the decay channel H to $ZZ(*)$ to $q \bar{q} \ell^- \ell^+$ in pp collisions at $\sqrt{s} = 7$ TeV*, *JHEP* **1204** (2012) 036, [[arXiv:1202.1416](#)].
- [2] **CMS** Collaboration, *Search for a Standard Model-like Higgs boson decaying into WW to $l \nu q \bar{q}$ in pp collisions at $\sqrt{s} = 8$ TeV*, Tech. Rep. CMS-PAS-HIG-13-008, 2013.
- [3] **ATLAS** Collaboration, G. Aad et al., *Measurement of jet charge in dijet events from $\sqrt{s}=8$ TeV pp collisions with the ATLAS detector*, *Phys. Rev.* **D93** (2016), no. 5 052003, [[arXiv:1509.05190](#)].
- [4] **ATLAS** Collaboration, G. Aad et al., *Measurement of colour flow with the jet pull angle in $t\bar{t}$ events using the ATLAS detector at $\sqrt{s} = 8$ TeV*, *Phys. Lett.* **B750** (2015) 475–493, [[arXiv:1506.05629](#)].
- [5] **ATLAS** Collaboration, *Performance of jet substructure techniques in early $\sqrt{s} = 13$ TeV pp collisions with the ATLAS detector*, Tech. Rep. ATLAS-CONF-2015-035, 2015.
- [6] **ATLAS** Collaboration, G. Aad et al., *Identification of boosted, hadronically decaying W bosons and comparisons with ATLAS data taken at $\sqrt{s} = 8$ TeV*, *Eur. Phys. J.* **C76** (2016), no. 3 154, [[arXiv:1510.05821](#)].
- [7] **ATLAS** Collaboration, G. Aad et al., *Measurement of the differential cross-section of highly boosted top quarks as a function of their transverse momentum in $\sqrt{s} = 8$ TeV proton-proton collisions using the ATLAS detector*, *Phys. Rev.* **D93** (2016), no. 3 032009, [[arXiv:1510.03818](#)].
- [8] **ATLAS** Collaboration, *Studies of b -tagging performance and jet substructure in a high p_T $g \rightarrow b\bar{b}$ rich sample of large- R jets from pp collisions at $\sqrt{s} = 8$ TeV with the ATLAS detector*, Tech. Rep. ATLAS-CONF-2016-002, CERN, 2016.
- [9] **ATLAS** Collaboration, *Boosted Higgs ($\rightarrow b\bar{b}$) Boson Identification with the ATLAS Detector at $\sqrt{s} = 13$ TeV*, Tech. Rep. ATLAS-CONF-2016-039, CERN, Geneva, Aug, 2016.
- [10] **ATLAS** Collaboration, *Discrimination of Light Quark and Gluon Jets in pp collisions at $\sqrt{s} = 8$ TeV with the ATLAS Detector*, Tech. Rep. ATLAS-CONF-2016-034, CERN, Geneva, Jul, 2016.
- [11] **CMS** Collaboration, *Measurement of the $t\bar{t}$ production cross section at 13 TeV in the all-jets final state*, Tech. Rep. CMS-PAS-TOP-16-013, CERN, Geneva, 2016.
- [12] **CMS** Collaboration, *Search for $t\bar{t}H$ production in the $H \rightarrow b\bar{b}$ decay channel with $\sqrt{s} = 13$ TeV pp collisions at the CMS experiment*, Tech. Rep. CMS-PAS-HIG-16-004, CERN, Geneva, 2016.
- [13] **CMS** Collaboration, *Search for BSM $t\bar{t}$ Production in the Boosted All-Hadronic Final State*, Tech. Rep. CMS-PAS-EXO-11-006, 2011.
- [14] **ATLAS, CMS** Collaboration, S. Fleischmann, *Boosted top quark techniques and searches for $t\bar{t}$ resonances at the LHC*, *J.Phys.Conf.Ser.* **452** (2013), no. 1 012034.

- [15] **ATLAS, CMS** Collaboration, J. Pilot, *Boosted Top Quarks, Top Pair Resonances, and Top Partner Searches at the LHC*, *EPJ Web Conf.* **60** (2013) 09003.
- [16] **ATLAS** Collaboration, *Performance of boosted top quark identification in 2012 ATLAS data*, Tech. Rep. ATLAS-CONF-2013-084, ATLAS-COM-CONF-2013-074, 2013.
- [17] **CMS** Collaboration, S. Chatrchyan et al., *Search for Anomalous $t\bar{t}$ Production in the Highly-Boosted All-Hadronic Final State*, *JHEP* **1209** (2012) 029, [[arXiv:1204.2488](#)].
- [18] **CMS Collaboration** Collaboration, *Search for pair-produced vector-like quarks of charge $-1/3$ decaying to bH using boosted Higgs jet-tagging in pp collisions at $\sqrt{s} = 8$ TeV*, Tech. Rep. CMS-PAS-B2G-14-001, CERN, Geneva, 2014.
- [19] **CMS** Collaboration, *Search for top-Higgs resonances in all-hadronic final states using jet substructure methods*, Tech. Rep. CMS-PAS-B2G-14-002, CERN, Geneva, 2014.
- [20] **CMS** Collaboration, V. Khachatryan et al., *Search for vector-like T quarks decaying to top quarks and Higgs bosons in the all-hadronic channel using jet substructure*, *JHEP* **06** (2015) 080, [[arXiv:1503.01952](#)].
- [21] **CMS** Collaboration, V. Khachatryan et al., *Search for a massive resonance decaying into a Higgs boson and a W or Z boson in hadronic final states in proton-proton collisions at $\sqrt{s} = 8$ TeV*, *JHEP* **02** (2016) 145, [[arXiv:1506.01443](#)].
- [22] **ATLAS** Collaboration, G. Aad et al., *Search for high-mass diboson resonances with boson-tagged jets in proton-proton collisions at $\sqrt{s} = 8$ TeV with the ATLAS detector*, *JHEP* **12** (2015) 055, [[arXiv:1506.00962](#)].
- [23] **ATLAS** Collaboration, M. Aaboud et al., *Searches for heavy diboson resonances in pp collisions at $\sqrt{s} = 13$ TeV with the ATLAS detector*, [arXiv:1606.04833](#).
- [24] **ATLAS** Collaboration, M. Aaboud et al., *Search for heavy resonances decaying to a Z boson and a photon in pp collisions at $\sqrt{s} = 13$ TeV with the ATLAS detector*, [arXiv:1607.06363](#).
- [25] **ATLAS** Collaboration, M. Aaboud et al., *Search for dark matter produced in association with a hadronically decaying vector boson in pp collisions at $\sqrt{s} = 13$ TeV with the ATLAS detector*, [arXiv:1608.02372](#).
- [26] **ATLAS** Collaboration, *Search for resonances with boson-tagged jets in 15.5 fb $^{-1}$ of pp collisions at $\sqrt{s} = 13$ TeV collected with the ATLAS detector*, Tech. Rep. ATLAS-CONF-2016-055, CERN, Geneva, Aug, 2016.
- [27] **ATLAS** Collaboration, *Search for diboson resonances in the llq final state in pp collisions at $\sqrt{s} = 13$ TeV with the ATLAS detector*, Tech. Rep. ATLAS-CONF-2015-071, CERN, Geneva, Dec, 2015.
- [28] **ATLAS** Collaboration, *Search for diboson resonances in the $\nu\nu qq$ final state in pp collisions at $\sqrt{s} = 13$ TeV with the ATLAS detector*, Tech. Rep. ATLAS-CONF-2015-068, CERN, Geneva, Dec, 2015.
- [29] **CMS** Collaboration, *Search for dark matter in final states with an energetic jet, or a hadronically decaying W or Z boson using 12.9 fb $^{-1}$ of data at $\sqrt{s} = 13$ TeV*, Tech. Rep. CMS-PAS-EXO-16-037, CERN, Geneva, 2016.
- [30] **CMS** Collaboration, *Search for new physics in a boosted hadronic monotop final state using 12.9 fb $^{-1}$ of $\sqrt{s} = 13$ TeV data*, Tech. Rep. CMS-PAS-EXO-16-040, CERN, Geneva, 2016.

- [31] CMS Collaboration, V. Khachatryan et al., *Search for dark matter in proton-proton collisions at 8 TeV with missing transverse momentum and vector boson tagged jets*, Submitted to: *JHEP* (2016) [[arXiv:1607.05764](#)].
- [32] CMS Collaboration, *Searches for invisible Higgs boson decays with the CMS detector.*, Tech. Rep. CMS-PAS-HIG-16-016, CERN, Geneva, 2016.
- [33] CMS Collaboration, *Search for top quark-antiquark resonances in the all-hadronic final state at $\sqrt{s}=13$ TeV*, Tech. Rep. CMS-PAS-B2G-15-003, CERN, Geneva, 2016.
- [34] CMS Collaboration, *Search for dark matter in association with a boosted top quark in the all hadronic final state*, Tech. Rep. CMS-PAS-EXO-16-017, CERN, Geneva, 2016.
- [35] A. Abdesselam, E. B. Kuutmann, U. Bitenc, G. Brooijmans, J. Butterworth, et al., *Boosted objects: A Probe of beyond the Standard Model physics*, *Eur.Phys.J.* **C71** (2011) 1661, [[arXiv:1012.5412](#)].
- [36] A. Altheimer, S. Arora, L. Asquith, G. Brooijmans, J. Butterworth, et al., *Jet Substructure at the Tevatron and LHC: New results, new tools, new benchmarks*, *J.Phys.* **G39** (2012) 063001, [[arXiv:1201.0008](#)].
- [37] A. Altheimer, A. Arce, L. Asquith, J. Backus Mayes, E. Bergeaas Kuutmann, et al., *Boosted objects and jet substructure at the LHC. Report of BOOST2012, held at IFIC Valencia, 23rd-27th of July 2012*, *Eur.Phys.J.* **C74** (2014) 2792, [[arXiv:1311.2708](#)].
- [38] D. Adams et al., *Towards an Understanding of the Correlations in Jet Substructure*, *Eur. Phys. J.* **C75** (2015), no. 9 409, [[arXiv:1504.00679](#)].
- [39] I. Feige, M. D. Schwartz, I. W. Stewart, and J. Thaler, *Precision Jet Substructure from Boosted Event Shapes*, *Phys.Rev.Lett.* **109** (2012) 092001, [[arXiv:1204.3898](#)].
- [40] M. Field, G. Gur-Ari, D. A. Kosower, L. Mannelli, and G. Perez, *Three-Prong Distribution of Massive Narrow QCD Jets*, *Phys.Rev.* **D87** (2013), no. 9 094013, [[arXiv:1212.2106](#)].
- [41] M. Dasgupta, A. Fregoso, S. Marzani, and G. P. Salam, *Towards an understanding of jet substructure*, *JHEP* **1309** (2013) 029, [[arXiv:1307.0007](#)].
- [42] M. Dasgupta, A. Fregoso, S. Marzani, and A. Powling, *Jet substructure with analytical methods*, *Eur.Phys.J.* **C73** (2013), no. 11 2623, [[arXiv:1307.0013](#)].
- [43] A. J. Larkoski, J. Thaler, and W. J. Waalewijn, *Gaining (Mutual) Information about Quark/Gluon Discrimination*, *JHEP* **1411** (2014) 129, [[arXiv:1408.3122](#)].
- [44] M. Dasgupta, A. Powling, and A. Siodmok, *On jet substructure methods for signal jets*, *JHEP* **08** (2015) 079, [[arXiv:1503.01088](#)].
- [45] M. Seymour, *Jet shapes in hadron collisions: Higher orders, resummation and hadronization*, *Nucl.Phys.* **B513** (1998) 269–300, [[hep-ph/9707338](#)].
- [46] H.-n. Li, Z. Li, and C.-P. Yuan, *QCD resummation for jet substructures*, *Phys.Rev.Lett.* **107** (2011) 152001, [[arXiv:1107.4535](#)].
- [47] A. J. Larkoski, *QCD Analysis of the Scale-Invariance of Jets*, *Phys.Rev.* **D86** (2012) 054004, [[arXiv:1207.1437](#)].
- [48] M. Jankowiak and A. J. Larkoski, *Angular Scaling in Jets*, *JHEP* **1204** (2012) 039, [[arXiv:1201.2688](#)].
- [49] Y.-T. Chien and I. Vitev, *Jet Shape Resummation Using Soft-Collinear Effective Theory*, *JHEP* **1412** (2014) 061, [[arXiv:1405.4293](#)].

- [50] Y.-T. Chien, *Resummation of Jet Shapes and Extracting Properties of the Quark-Gluon Plasma*, *Int.J.Mod.Phys.Conf.Ser.* **37** (2015) 1560047, [[arXiv:1411.0741](#)].
- [51] J. Isaacson, H.-n. Li, Z. Li, and C. P. Yuan, *Factorization for substructures of boosted Higgs jets*, [arXiv:1505.06368](#).
- [52] D. Krohn, M. D. Schwartz, T. Lin, and W. J. Waalewijn, *Jet Charge at the LHC*, *Phys.Rev.Lett.* **110** (2013), no. 21 212001, [[arXiv:1209.2421](#)].
- [53] W. J. Waalewijn, *Calculating the Charge of a Jet*, *Phys.Rev.* **D86** (2012) 094030, [[arXiv:1209.3019](#)].
- [54] A. J. Larkoski, I. Moult, and D. Neill, *Toward Multi-Differential Cross Sections: Measuring Two Angularities on a Single Jet*, *JHEP* **1409** (2014) 046, [[arXiv:1401.4458](#)].
- [55] M. Procura, W. J. Waalewijn, and L. Zeune, *Resummation of Double-Differential Cross Sections and Fully-Unintegrated Parton Distribution Functions*, *JHEP* **1502** (2015) 117, [[arXiv:1410.6483](#)].
- [56] D. Bertolini, J. Thaler, and J. R. Walsh, *The First Calculation of Fractional Jets*, *JHEP* **1505** (2015) 008, [[arXiv:1501.01965](#)].
- [57] B. Bhattacharjee, S. Mukhopadhyay, M. M. Nojiri, Y. Sakaki, and B. R. Webber, *Associated jet and subjet rates in light-quark and gluon jet discrimination*, *JHEP* **1504** (2015) 131, [[arXiv:1501.04794](#)].
- [58] A. J. Larkoski, I. Moult, and D. Neill, *Analytic Boosted Boson Discrimination*, *JHEP* **05** (2016) 117, [[arXiv:1507.03018](#)].
- [59] M. Dasgupta, L. Schunk, and G. Soyez, *Jet shapes for boosted jet two-prong decays from first-principles*, *JHEP* **04** (2016) 166, [[arXiv:1512.00516](#)].
- [60] C. Frye, A. J. Larkoski, M. D. Schwartz, and K. Yan, *Precision physics with pile-up insensitive observables*, [arXiv:1603.06375](#).
- [61] C. Frye, A. J. Larkoski, M. D. Schwartz, and K. Yan, *Factorization for groomed jet substructure beyond the next-to-leading logarithm*, *JHEP* **07** (2016) 064, [[arXiv:1603.09338](#)].
- [62] Z.-B. Kang, F. Ringer, and I. Vitev, *Jet substructure using semi-inclusive jet functions within SCET*, [arXiv:1606.07063](#).
- [63] A. Hornig, Y. Makris, and T. Mehen, *Jet Shapes in Dijet Events at the LHC in SCET*, *JHEP* **04** (2016) 097, [[arXiv:1601.01319](#)].
- [64] J. R. Walsh and S. Zuberi, *Factorization Constraints on Jet Substructure*, [arXiv:1110.5333](#).
- [65] A. J. Larkoski, I. Moult, and D. Neill, *Power Counting to Better Jet Observables*, *JHEP* **1412** (2014) 009, [[arXiv:1409.6298](#)].
- [66] A. J. Larkoski, I. Moult, and D. Neill, *Building a Better Boosted Top Tagger*, *Phys.Rev.* **D91** (2015), no. 3 034035, [[arXiv:1411.0665](#)].
- [67] J. Cogan, M. Kagan, E. Strauss, and A. Schwartzman, *Jet-Images: Computer Vision Inspired Techniques for Jet Tagging*, *JHEP* **02** (2015) 118, [[arXiv:1407.5675](#)].
- [68] L. de Oliveira, M. Kagan, L. Mackey, B. Nachman, and A. Schwartzman, *Jet-images — deep learning edition*, *JHEP* **07** (2016) 069, [[arXiv:1511.05190](#)].

- [69] L. G. Almeida, M. Backović, M. Cliche, S. J. Lee, and M. Perelstein, *Playing Tag with ANN: Boosted Top Identification with Pattern Recognition*, *JHEP* **07** (2015) 086, [[arXiv:1501.05968](#)].
- [70] P. Baldi, K. Bauer, C. Eng, P. Sadowski, and D. Whiteson, *Jet Substructure Classification in High-Energy Physics with Deep Neural Networks*, *Phys. Rev.* **D93** (2016), no. 9 094034, [[arXiv:1603.09349](#)].
- [71] D. Guest, J. Collado, P. Baldi, S.-C. Hsu, G. Urban, and D. Whiteson, *Jet Flavor Classification in High-Energy Physics with Deep Neural Networks*, [arXiv:1607.08633](#).
- [72] J. S. Conway, R. Bhaskar, R. D. Erbacher, and J. Pilot, *Identification of High-Momentum Top Quarks, Higgs Bosons, and W and Z Bosons Using Boosted Event Shapes*, [arXiv:1606.06859](#).
- [73] J. Barnard, E. N. Dawe, M. J. Dolan, and N. Rajcic, *Parton Shower Uncertainties in Jet Substructure Analyses with Deep Neural Networks*, [arXiv:1609.00607](#).
- [74] A. J. Larkoski, G. P. Salam, and J. Thaler, *Energy Correlation Functions for Jet Substructure*, *JHEP* **1306** (2013) 108, [[arXiv:1305.0007](#)].
- [75] J. M. Butterworth, A. R. Davison, M. Rubin, and G. P. Salam, *Jet substructure as a new Higgs search channel at the LHC*, *Phys.Rev.Lett.* **100** (2008) 242001, [[arXiv:0802.2470](#)].
- [76] S. D. Ellis, C. K. Vermilion, and J. R. Walsh, *Techniques for improved heavy particle searches with jet substructure*, *Phys.Rev.* **D80** (2009) 051501, [[arXiv:0903.5081](#)].
- [77] S. D. Ellis, C. K. Vermilion, and J. R. Walsh, *Recombination Algorithms and Jet Substructure: Pruning as a Tool for Heavy Particle Searches*, *Phys.Rev.* **D81** (2010) 094023, [[arXiv:0912.0033](#)].
- [78] D. Krohn, J. Thaler, and L.-T. Wang, *Jet Trimming*, *JHEP* **1002** (2010) 084, [[arXiv:0912.1342](#)].
- [79] J. Dolen, P. Harris, S. Marzani, S. Rappoccio, and N. Tran, *Thinking outside the ROCs: Designing Decorrelated Taggers (DDT) for jet substructure*, *JHEP* **05** (2016) 156, [[arXiv:1603.00027](#)].
- [80] *Identification of boosted, hadronically-decaying W and Z bosons in $\sqrt{s} = 13$ TeV Monte Carlo Simulations for ATLAS*, Tech. Rep. ATL-PHYS-PUB-2015-033, CERN, Geneva, Aug, 2015.
- [81] **CMS** Collaboration, *Search for light vector resonances decaying to quarks at $\sqrt{s} = 13$ TeV*, Tech. Rep. CMS-PAS-EXO-16-030, CERN, Geneva, 2016.
- [82] J. Thaler and K. Van Tilburg, *Identifying Boosted Objects with N-subjettiness*, *JHEP* **1103** (2011) 015, [[arXiv:1011.2268](#)].
- [83] J. Thaler and K. Van Tilburg, *Maximizing Boosted Top Identification by Minimizing N-subjettiness*, *JHEP* **1202** (2012) 093, [[arXiv:1108.2701](#)].
- [84] M. Cacciari, G. P. Salam, and G. Soyez, *FastJet User Manual*, *Eur.Phys.J.* **C72** (2012) 1896, [[arXiv:1111.6097](#)].
- [85] “Fastjet contrib.” <http://fastjet.hepforge.org/contrib/>.
- [86] A. J. Larkoski, S. Marzani, G. Soyez, and J. Thaler, *Soft Drop*, *JHEP* **1405** (2014) 146, [[arXiv:1402.2657](#)].

- [87] S. Catani, G. Turnock, and B. Webber, *Jet broadening measures in e^+e^- annihilation*, *Phys.Lett.* **B295** (1992) 269–276.
- [88] Y. L. Dokshitzer, A. Lucenti, G. Marchesini, and G. Salam, *On the QCD analysis of jet broadening*, *JHEP* **9801** (1998) 011, [[hep-ph/9801324](#)].
- [89] A. Banfi, G. P. Salam, and G. Zanderighi, *Principles of general final-state resummation and automated implementation*, *JHEP* **0503** (2005) 073, [[hep-ph/0407286](#)].
- [90] A. J. Larkoski, D. Neill, and J. Thaler, *Jet Shapes with the Broadening Axis*, *JHEP* **1404** (2014) 017, [[arXiv:1401.2158](#)].
- [91] I. W. Stewart, F. J. Tackmann, and W. J. Waalewijn, *N -Jettiness: An Inclusive Event Shape to Veto Jets*, *Phys.Rev.Lett.* **105** (2010) 092002, [[arXiv:1004.2489](#)].
- [92] I. W. Stewart, F. J. Tackmann, J. Thaler, C. K. Vermilion, and T. F. Wilkason, *X Cone: N -jettiness as an Exclusive Cone Jet Algorithm*, *JHEP* **11** (2015) 072, [[arXiv:1508.01516](#)].
- [93] J. Thaler and T. F. Wilkason, *Resolving Boosted Jets with X Cone*, *JHEP* **12** (2015) 051, [[arXiv:1508.01518](#)].
- [94] A. J. Larkoski and I. Moult, *The Singular Behavior of Jet Substructure Observables*, *Phys. Rev.* **D93** (2016) 014017, [[arXiv:1510.08459](#)].
- [95] E. Farhi, *A QCD Test for Jets*, *Phys.Rev.Lett.* **39** (1977) 1587–1588.
- [96] M. Cacciari and G. P. Salam, *Pileup subtraction using jet areas*, *Phys. Lett.* **B659** (2008) 119–126, [[arXiv:0707.1378](#)].
- [97] R. Alon, E. Duchovni, G. Perez, A. P. Pranko, and P. K. Sinervo, *A Data-driven method of pile-up correction for the substructure of massive jets*, *Phys. Rev.* **D84** (2011) 114025, [[arXiv:1101.3002](#)].
- [98] G. Soyez, G. P. Salam, J. Kim, S. Dutta, and M. Cacciari, *Pileup subtraction for jet shapes*, *Phys.Rev.Lett.* **110** (2013), no. 16 162001, [[arXiv:1211.2811](#)].
- [99] J. Tseng and H. Evans, *Sequential recombination algorithm for jet clustering and background subtraction*, *Phys. Rev.* **D88** (2013) 014044, [[arXiv:1304.1025](#)].
- [100] D. Krohn, M. D. Schwartz, M. Low, and L.-T. Wang, *Jet Cleansing: Pileup Removal at High Luminosity*, *Phys. Rev.* **D90** (2014), no. 6 065020, [[arXiv:1309.4777](#)].
- [101] M. Cacciari, G. P. Salam, and G. Soyez, *SoftKiller, a particle-level pileup removal method*, *Eur. Phys. J.* **C75** (2015), no. 2 59, [[arXiv:1407.0408](#)].
- [102] D. Bertolini, P. Harris, M. Low, and N. Tran, *Pileup Per Particle Identification*, *JHEP* **10** (2014) 059, [[arXiv:1407.6013](#)].
- [103] M. Dasgupta and G. Salam, *Resummation of nonglobal QCD observables*, *Phys.Lett.* **B512** (2001) 323–330, [[hep-ph/0104277](#)].
- [104] M. Cacciari, G. P. Salam, and G. Soyez, *The Anti- $k(t)$ jet clustering algorithm*, *JHEP* **0804** (2008) 063, [[arXiv:0802.1189](#)].
- [105] Y. L. Dokshitzer, G. Leder, S. Moretti, and B. Webber, *Better jet clustering algorithms*, *JHEP* **9708** (1997) 001, [[hep-ph/9707323](#)].
- [106] M. Wobisch and T. Wengler, *Hadronization corrections to jet cross-sections in deep inelastic scattering*, [hep-ph/9907280](#).

- [107] M. Wobisch, *Measurement and QCD analysis of jet cross-sections in deep inelastic positron proton collisions at $\sqrt{s} = 300$ GeV*, 2000.
- [108] C. W. Bauer, S. Fleming, and M. E. Luke, *Summing Sudakov logarithms in $B \rightarrow X(s\gamma)$ in effective field theory*, *Phys.Rev.* **D63** (2000) 014006, [[hep-ph/0005275](#)].
- [109] C. W. Bauer, S. Fleming, D. Pirjol, and I. W. Stewart, *An Effective field theory for collinear and soft gluons: Heavy to light decays*, *Phys.Rev.* **D63** (2001) 114020, [[hep-ph/0011336](#)].
- [110] C. W. Bauer and I. W. Stewart, *Invariant operators in collinear effective theory*, *Phys.Lett.* **B516** (2001) 134–142, [[hep-ph/0107001](#)].
- [111] C. W. Bauer, D. Pirjol, and I. W. Stewart, *Soft collinear factorization in effective field theory*, *Phys.Rev.* **D65** (2002) 054022, [[hep-ph/0109045](#)].
- [112] A. V. Manohar and I. W. Stewart, *The Zero-Bin and Mode Factorization in Quantum Field Theory*, *Phys.Rev.* **D76** (2007) 074002, [[hep-ph/0605001](#)].
- [113] M. Dasgupta, F. Dreyer, G. P. Salam, and G. Soyez, *Small-radius jets to all orders in QCD*, *JHEP* **1504** (2015) 039, [[arXiv:1411.5182](#)].
- [114] Y.-T. Chien, A. Hornig, and C. Lee, *Soft-collinear mode for jet cross sections in soft collinear effective theory*, *Phys. Rev.* **D93** (2016), no. 1 014033, [[arXiv:1509.04287](#)].
- [115] D. W. Kolodrubetz, P. Pietrulewicz, I. W. Stewart, F. J. Tackmann, and W. J. Waalewijn, *Factorization for Jet Radius Logarithms in Jet Mass Spectra at the LHC*, [[arXiv:1605.08038](#)].
- [116] Z.-B. Kang, F. Ringer, and I. Vitev, *The semi-inclusive jet function in SCET and small radius resummation for inclusive jet production*, [[arXiv:1606.06732](#)].
- [117] C. W. Bauer, F. J. Tackmann, J. R. Walsh, and S. Zuberi, *Factorization and Resummation for Dijet Invariant Mass Spectra*, *Phys.Rev.* **D85** (2012) 074006, [[arXiv:1106.6047](#)].
- [118] A. J. Larkoski, I. Moult, and D. Neill, *Non-Global Logarithms, Factorization, and the Soft Substructure of Jets*, *JHEP* **09** (2015) 143, [[arXiv:1501.04596](#)].
- [119] P. Pietrulewicz, F. J. Tackmann, and W. J. Waalewijn, *Factorization and Resummation for Generic Hierarchies between Jets*, *JHEP* **08** (2016) 002, [[arXiv:1601.05088](#)].
- [120] A. J. Larkoski and J. Thaler, *Unsafe but Calculable: Ratios of Angularities in Perturbative QCD*, *JHEP* **1309** (2013) 137, [[arXiv:1307.1699](#)].
- [121] A. J. Larkoski, S. Marzani, and J. Thaler, *Sudakov Safety in Perturbative QCD*, *Phys.Rev.* **D91** (2015), no. 11 111501, [[arXiv:1502.01719](#)].
- [122] F. V. Tkachov, *Measuring multi - jet structure of hadronic energy flow or What is a jet?*, *Int. J. Mod. Phys.* **A12** (1997) 5411–5529, [[hep-ph/9601308](#)].
- [123] N. Sveshnikov and F. Tkachov, *Jets and quantum field theory*, *Phys.Lett.* **B382** (1996) 403–408, [[hep-ph/9512370](#)].
- [124] P. S. Chervor and N. A. Sveshnikov, *Jet observables and energy momentum tensor*, in *Quantum field theory and high-energy physics. Proceedings, Workshop, QFTHEP'97, Samara, Russia, September 4-10, 1997*, pp. 402–407, 1997. [[hep-ph/9710349](#)].
- [125] F. V. Tkachov, *A Theory of jet definition*, *Int. J. Mod. Phys.* **A17** (2002) 2783–2884, [[hep-ph/9901444](#)].

- [126] G. C. Fox and S. Wolfram, *Observables for the Analysis of Event Shapes in e^+e^- Annihilation and Other Processes*, *Phys. Rev. Lett.* **41** (1978) 1581.
- [127] G. C. Fox and S. Wolfram, *Event Shapes in e^+e^- Annihilation*, *Nucl. Phys.* **B149** (1979) 413. [Erratum: *Nucl. Phys.*B157,543(1979)].
- [128] G. Gur-Ari, M. Papucci, and G. Perez, *Classification of Energy Flow Observables in Narrow Jets*, [arXiv:1101.2905](#).
- [129] D. E. Kaplan, K. Rehermann, M. D. Schwartz, and B. Tweedie, *Top Tagging: A Method for Identifying Boosted Hadronically Decaying Top Quarks*, *Phys.Rev.Lett.* **101** (2008) 142001, [[arXiv:0806.0848](#)].
- [130] J. Thaler and L.-T. Wang, *Strategies to Identify Boosted Tops*, *JHEP* **0807** (2008) 092, [[arXiv:0806.0023](#)].
- [131] L. G. Almeida, S. J. Lee, G. Perez, G. F. Sterman, I. Sung, et al., *Substructure of high- p_T Jets at the LHC*, *Phys.Rev.* **D79** (2009) 074017, [[arXiv:0807.0234](#)].
- [132] L. G. Almeida, S. J. Lee, G. Perez, I. Sung, and J. Virzi, *Top Jets at the LHC*, *Phys.Rev.* **D79** (2009) 074012, [[arXiv:0810.0934](#)].
- [133] T. Plehn, G. P. Salam, and M. Spannowsky, *Fat Jets for a Light Higgs*, *Phys.Rev.Lett.* **104** (2010) 111801, [[arXiv:0910.5472](#)].
- [134] T. Plehn, M. Spannowsky, M. Takeuchi, and D. Zerwas, *Stop Reconstruction with Tagged Tops*, *JHEP* **1010** (2010) 078, [[arXiv:1006.2833](#)].
- [135] L. G. Almeida, S. J. Lee, G. Perez, G. Sterman, and I. Sung, *Template Overlap Method for Massive Jets*, *Phys.Rev.* **D82** (2010) 054034, [[arXiv:1006.2035](#)].
- [136] M. Jankowiak and A. J. Larkoski, *Jet Substructure Without Trees*, *JHEP* **1106** (2011) 057, [[arXiv:1104.1646](#)].
- [137] D. E. Soper and M. Spannowsky, *Finding top quarks with shower deconstruction*, *Phys.Rev.* **D87** (2013), no. 5 054012, [[arXiv:1211.3140](#)].
- [138] C. Anders, C. Bernaciak, G. Kasieczka, T. Plehn, and T. Schell, *Benchmarking an even better top tagger algorithm*, *Phys. Rev.* **D89** (2014), no. 7 074047, [[arXiv:1312.1504](#)].
- [139] M. Freytsis, T. Volansky, and J. R. Walsh, *Tagging Partially Reconstructed Objects with Jet Substructure*, [arXiv:1412.7540](#).
- [140] A. J. Larkoski, F. Maltoni, and M. Selvaggi, *Tracking down hyper-boosted top quarks*, *JHEP* **1506** (2015) 032, [[arXiv:1503.03347](#)].
- [141] G. Kasieczka, T. Plehn, T. Schell, T. Strebler, and G. P. Salam, *Resonance Searches with an Updated Top Tagger*, *JHEP* **06** (2015) 203, [[arXiv:1503.05921](#)].
- [142] T. Lapsien, R. Kogler, and J. Haller, *A new tagger for hadronically decaying heavy particles at the LHC*, [arXiv:1606.04961](#).
- [143] **ATLAS** Collaboration, *Identification and Tagging of Double b -hadron jets with the ATLAS Detector*, Tech. Rep. ATLAS-CONF-2012-100, CERN, Geneva, Jul, 2012.
- [144] **CMS** Collaboration, *Performance of b tagging at $\sqrt{s}=8$ TeV in multijet, $t\bar{t}$ and boosted topology events*, Tech. Rep. CMS-PAS-BTV-13-001, 2013.
- [145] **ATLAS** Collaboration, *b -tagging in dense environments*, Tech. Rep. ATL-PHYS-PUB-2014-014, CERN, Geneva, Aug, 2014.

- [146] **ATLAS** Collaboration, *Expected Performance of Boosted Higgs ($\rightarrow b\bar{b}$) Boson Identification with the ATLAS Detector at $\sqrt{s} = 13$ TeV*, Tech. Rep. ATL-PHYS-PUB-2015-035, CERN, Geneva, Aug, 2015.
- [147] **CMS** Collaboration, *Identification of b quark jets at the CMS Experiment in the LHC Run 2*, Tech. Rep. CMS-PAS-BTV-15-001, CERN, Geneva, 2016.
- [148] **CMS** Collaboration, *Identification of double- b quark jets in boosted event topologies*, Tech. Rep. CMS-PAS-BTV-15-002, CERN, Geneva, 2016.
- [149] **ATLAS** Collaboration, *Calibration of ATLAS b -tagging algorithms in dense jet environments*, Tech. Rep. ATLAS-CONF-2016-001, CERN, Geneva, Feb, 2016.
- [150] D. E. Soper and M. Spannowsky, *Finding physics signals with shower deconstruction*, *Phys. Rev.* **D84** (2011) 074002, [[arXiv:1102.3480](#)].
- [151] D. E. Soper and M. Spannowsky, *Finding physics signals with event deconstruction*, *Phys. Rev.* **D89** (2014), no. 9 094005, [[arXiv:1402.1189](#)].
- [152] **ATLAS** Collaboration, G. Aad et al., *Identification of high transverse momentum top quarks in pp collisions at $\sqrt{s} = 8$ TeV with the ATLAS detector*, *JHEP* **06** (2016) 093, [[arXiv:1603.03127](#)].
- [153] **CMS** Collaboration, *Top Tagging with New Approaches*, Tech. Rep. CMS-PAS-JME-15-002, CERN, Geneva, 2016.
- [154] G. Soyez, *A QCD description of jet shapes for boosted jets*, *BOOST Conference* (2016).
- [155] G. P. Salam, L. Schunk, and G. Soyez, *Towards a better use of N -subjettiness*, *forthcoming* (2016).
- [156] J. Alwall, R. Frederix, S. Frixione, V. Hirschi, F. Maltoni, et al., *The automated computation of tree-level and next-to-leading order differential cross sections, and their matching to parton shower simulations*, *JHEP* **1407** (2014) 079, [[arXiv:1405.0301](#)].
- [157] T. Sjostrand, S. Mrenna, and P. Z. Skands, *PYTHIA 6.4 Physics and Manual*, *JHEP* **0605** (2006) 026, [[hep-ph/0603175](#)].
- [158] T. Sjostrand, S. Mrenna, and P. Z. Skands, *A Brief Introduction to PYTHIA 8.1*, *Comput.Phys.Commun.* **178** (2008) 852–867, [[arXiv:0710.3820](#)].
- [159] A. J. Larkoski and J. Thaler, *Aspects of jets at 100 TeV*, *Phys.Rev.* **D90** (2014), no. 3 034010, [[arXiv:1406.7011](#)].
- [160] **ATLAS** Collaboration, *Boosted hadronic top identification at ATLAS for early 13 TeV data*, Tech. Rep. ATL-PHYS-PUB-2015-053, CERN, Geneva, Dec, 2015.
- [161] **ATLAS** Collaboration, *Searches for heavy ZZ and ZW resonances in the $llqq$ and $vvqq$ final states in pp collisions at $\sqrt{s} = 13$ TeV with the ATLAS detector*, Tech. Rep. ATLAS-CONF-2016-082, CERN, Geneva, Aug, 2016.
- [162] **ATLAS** Collaboration, *A Search for Resonances Decaying to a W or Z Boson and a Higgs Boson in the $q\bar{q}^{(\prime)}b\bar{b}$ Final State*, Tech. Rep. ATLAS-CONF-2016-083, CERN, Geneva, Aug, 2016.
- [163] **CMS** Collaboration, *Search for new resonances decaying to $WW/WZ \rightarrow \ell\nu qq$* , Tech. Rep. CMS-PAS-B2G-16-020, CERN, 2016.
- [164] **CMS** Collaboration, *Search for high-mass resonances in the $Z(q\bar{q})\gamma$ final state at $\sqrt{s} = 8$ TeV*, Tech. Rep. CMS-PAS-EXO-16-025, CERN, 2016.

- [165] **CMS** Collaboration, *Combination of diboson resonance searches at 8 and 13 TeV*, Tech. Rep. CMS-PAS-B2G-16-007, CERN, 2016.
- [166] D. Gonçalves, F. Krauss, and M. Spannowsky, *Augmenting the diboson excess for the LHC Run II*, *Phys. Rev.* **D92** (2015), no. 5 053010, [[arXiv:1508.04162](#)].
- [167] A. Martin and T. S. Roy, *Cautionary tale of mismeasured tails from q/g bias*, *Phys. Rev.* **D94** (2016), no. 1 014003, [[arXiv:1604.05728](#)].
- [168] A. J. Larkoski and I. Moutl, *Nonglobal correlations in collider physics*, *Phys. Rev.* **D93** (2016), no. 1 014012, [[arXiv:1510.05657](#)].
- [169] W. T. Giele, D. A. Kosower, and P. Z. Skands, *A simple shower and matching algorithm*, *Phys.Rev.* **D78** (2008) 014026, [[arXiv:0707.3652](#)].
- [170] W. Giele, D. Kosower, and P. Skands, *Higher-Order Corrections to Timelike Jets*, *Phys.Rev.* **D84** (2011) 054003, [[arXiv:1102.2126](#)].
- [171] A. Gehrmann-De Ridder, M. Ritzmann, and P. Z. Skands, *Timelike Dipole-Antenna Showers with Massive Fermions*, *Phys.Rev.* **D85** (2012) 014013, [[arXiv:1108.6172](#)].
- [172] M. Ritzmann, D. Kosower, and P. Skands, *Antenna Showers with Hadronic Initial States*, *Phys.Lett.* **B718** (2013) 1345–1350, [[arXiv:1210.6345](#)].
- [173] L. Hartgring, E. Laenen, and P. Skands, *Antenna Showers with One-Loop Matrix Elements*, *JHEP* **1310** (2013) 127, [[arXiv:1303.4974](#)].
- [174] A. J. Larkoski, J. J. Lopez-Villarejo, and P. Skands, *Helicity-Dependent Showers and Matching with VINCIA*, *Phys.Rev.* **D87** (2013), no. 5 054033, [[arXiv:1301.0933](#)].
- [175] N. Fischer, S. Prestel, M. Ritzmann, and P. Skands, *Vincia for Hadron Colliders*, [arXiv:1605.06142](#).
- [176] **ATLAS** Collaboration, *Search for resonances with boson-tagged jets in 3.2 fb¹ of p p collisions at s = 13 TeV collected with the ATLAS detector*, Tech. Rep. ATLAS-CONF-2015-073, CERN, Geneva, Dec, 2015.
- [177] **ATLAS** Collaboration, *Search for ZZ resonances in the ℓℓqq final state in pp collisions at √s = 13 TeV with the ATLAS detector*, Tech. Rep. ATLAS-CONF-2016-016, CERN, Geneva, Mar, 2016.
- [178] **CMS** Collaboration, *V Tagging Observables and Correlations*, Tech. Rep. CMS-PAS-JME-14-002, CERN, Geneva, 2014.
- [179] J. Gallicchio and M. D. Schwartz, *Pure Samples of Quark and Gluon Jets at the LHC*, *JHEP* **1110** (2011) 103, [[arXiv:1104.1175](#)].
- [180] J. Gallicchio and M. D. Schwartz, *Quark and Gluon Tagging at the LHC*, *Phys.Rev.Lett.* **107** (2011) 172001, [[arXiv:1106.3076](#)].
- [181] J. Gallicchio and M. D. Schwartz, *Quark and Gluon Jet Substructure*, *JHEP* **1304** (2013) 090, [[arXiv:1211.7038](#)].
- [182] J. R. Andersen et al., *Les Houches 2015: Physics at TeV Colliders Standard Model Working Group Report*, in *9th Les Houches Workshop on Physics at TeV Colliders (PhysTeV 2015) Les Houches, France, June 1-19, 2015*, 2016. [arXiv:1605.04692](#).
- [183] **CMS** Collaboration, *Pileup Jet Identification*, Tech. Rep. CMS-PAS-JME-13-005, 2013.

- [184] **CMS** Collaboration, *Performance of quark/gluon discrimination in 8 TeV pp data*, Tech. Rep. CMS-PAS-JME-13-002, 2013.
- [185] **ATLAS** Collaboration, G. Aad et al., *Light-quark and gluon jet discrimination in pp collisions at $\sqrt{s} = 7$ TeV with the ATLAS detector*, [arXiv:1405.6583](#).
- [186] C. F. Berger, T. Kucs, and G. F. Sterman, *Event shape / energy flow correlations*, *Phys.Rev.* **D68** (2003) 014012, [[hep-ph/0303051](#)].
- [187] S. J. Brodsky and J. F. Gunion, *Hadron Multiplicity in Color Gauge Theory Models*, *Phys. Rev. Lett.* **37** (1976) 402–405.
- [188] K. Konishi, A. Ukawa, and G. Veneziano, *A Simple Algorithm for QCD Jets*, *Phys. Lett.* **B78** (1978) 243–248.
- [189] A. H. Mueller, *Square Root of alpha (Q^{**2}) Corrections to Particle Multiplicity Ratios in Gluon and Quark Jets*, *Nucl. Phys.* **B241** (1984) 141–154.
- [190] E. D. Malaza and B. R. Webber, *QCD CORRECTIONS TO JET MULTIPLICITY MOMENTS*, *Phys. Lett.* **B149** (1984) 501–503.
- [191] J. B. Gaffney and A. H. Mueller, *Alpha (Q^{**2}) Corrections to Particle Multiplicity Ratios in Gluon and Quark Jets*, *Nucl. Phys.* **B250** (1985) 109–142.
- [192] E. D. Malaza and B. R. Webber, *Multiplicity Distributions in Quark and Gluon Jets*, *Nucl. Phys.* **B267** (1986) 702–713.
- [193] S. Catani, Y. L. Dokshitzer, F. Fiorani, and B. R. Webber, *Average number of jets in $e^+ e^-$ annihilation*, *Nucl. Phys.* **B377** (1992) 445–460.
- [194] S. Catani, B. R. Webber, Y. L. Dokshitzer, and F. Fiorani, *Average multiplicities in two and three jet $e^+ e^-$ annihilation events*, *Nucl. Phys.* **B383** (1992) 419–441.
- [195] I. M. Dremin and V. A. Nechitailo, *Moments of multiplicity distributions in higher order perturbative QCD*, *JETP Lett.* **58** (1993) 881–885.
- [196] I. M. Dremin and V. A. Nechitailo, *Average multiplicities in gluon and quark jets in higher order perturbative QCD*, *Mod. Phys. Lett.* **A9** (1994) 1471–1478, [[hep-ex/9406002](#)].
- [197] A. Capella, I. M. Dremin, J. W. Gary, V. A. Nechitailo, and J. Tran Thanh Van, *Evolution of average multiplicities of quark and gluon jets*, *Phys. Rev.* **D61** (2000) 074009, [[hep-ph/9910226](#)].
- [198] P. Bolzoni, B. A. Kniehl, and A. V. Kotikov, *Gluon and quark jet multiplicities at $N^3LO+NNLL$* , *Phys. Rev. Lett.* **109** (2012) 242002, [[arXiv:1209.5914](#)].
- [199] **ATLAS** Collaboration, G. Aad et al., *Measurement of the charged-particle multiplicity inside jets from $\sqrt{s} = 8$ TeV pp collisions with the ATLAS detector*, *Eur. Phys. J.* **C76** (2016), no. 6 322, [[arXiv:1602.00988](#)].
- [200] D. Ferreira de Lima, P. Petrov, D. Soper, and M. Spannowsky, *Quark-Gluon tagging with Shower Deconstruction: Unearthing dark matter and Higgs couplings*, [arXiv:1607.06031](#).
- [201] **DELPHI** Collaboration, J. Abdallah et al., *A Study of the energy evolution of event shape distributions and their means with the DELPHI detector at LEP*, *Eur. Phys. J.* **C29** (2003) 285–312, [[hep-ex/0307048](#)].
- [202] **ALEPH** Collaboration, A. Heister et al., *Studies of QCD at $e^+ e^-$ centre-of-mass energies between 91-GeV and 209-GeV*, *Eur. Phys. J.* **C35** (2004) 457–486.

- [203] **L3** Collaboration, P. Achard et al., *Studies of hadronic event structure in e^+e^- annihilation from 30-GeV to 209-GeV with the L3 detector*, *Phys.Rept.* **399** (2004) 71–174, [[hep-ex/0406049](#)].
- [204] **OPAL** Collaboration, G. Abbiendi et al., *Measurement of event shape distributions and moments in $e^+e^- \rightarrow j$ hadrons at 91-GeV - 209-GeV and a determination of $\alpha(s)$* , *Eur. Phys. J.* **C40** (2005) 287–316, [[hep-ex/0503051](#)].
- [205] G. P. Korchemsky and G. F. Sterman, *Power corrections to event shapes and factorization*, *Nucl.Phys.* **B555** (1999) 335–351, [[hep-ph/9902341](#)].
- [206] G. Korchemsky and S. Tafat, *On power corrections to the event shape distributions in QCD*, *JHEP* **0010** (2000) 010, [[hep-ph/0007005](#)].
- [207] S. Bosch, B. Lange, M. Neubert, and G. Paz, *Factorization and shape function effects in inclusive B meson decays*, *Nucl.Phys.* **B699** (2004) 335–386, [[hep-ph/0402094](#)].
- [208] A. H. Hoang and I. W. Stewart, *Designing gapped soft functions for jet production*, *Phys.Lett.* **B660** (2008) 483–493, [[arXiv:0709.3519](#)].
- [209] Z. Ligeti, I. W. Stewart, and F. J. Tackmann, *Treating the b quark distribution function with reliable uncertainties*, *Phys.Rev.* **D78** (2008) 114014, [[arXiv:0807.1926](#)].
- [210] R. Boughezal, C. Focke, X. Liu, and F. Petriello, *W-boson production in association with a jet at next-to-next-to-leading order in perturbative QCD*, *Phys. Rev. Lett.* **115** (2015), no. 6 062002, [[arXiv:1504.02131](#)].
- [211] J. Gaunt, M. Stahlhofen, F. J. Tackmann, and J. R. Walsh, *N-jettiness Subtractions for NNLO QCD Calculations*, *JHEP* **09** (2015) 058, [[arXiv:1505.04794](#)].
- [212] A. Hook, M. Jankowiak, and J. G. Wacker, *Jet Dipolarity: Top Tagging with Color Flow*, *JHEP* **04** (2012) 007, [[arXiv:1102.1012](#)].